T H E U N I V E R S I T Y O F T U L S A

THE GRADUATE SCHOOL

CONDITIONING 3D STOCHASTIC CHANNELS TO WELL-TEST PRESSURE DATA

by

Zhuoxin Bi

A dissertation submitted in partial fulfillment of

the requirements for the degree of Doctor of Philosophy

in the Discipline of Petroleum Engineering

The Graduate School

The University of Tulsa

1999

T H E U N I V E R S I T Y O F T U L S A

THE GRADUATE SCHOOL

CONDITIONING 3D STOCHASTIC CHANNELS TO WELL-TEST PRESSURE DATA

by

Zhuoxin Bi

A DISSERTATION

APPROVED FOR THE DISCIPLINE OF

PETROLEUM ENGINEERIN

By Dissertation Committee

_____, Co-Chairperson

_____, Co-Chairperson

_____

_____

ABSTRACT

Zhuoxin, Bi (Doctor of Philosophy in Petroleum Engineering)

Conditioning 3D Stochastic Channels to

Well-Test Pressure Data (150 pp. - Chapter VI)

Co-Directed by Dr. Albert C. Reynolds, Jr. and Dr. Dean S. Oliver

(327 words)

This dissertation addresses the problem of simulating stochastic 3-D channels that are conditional to well-test pressure data. The channels are characterized by four random variables that define the principal direction line (PDL), and by four one-dimensional random fields that define the deviation of the channel center from the PDL in the horizontal and vertical directions, and the channel width and aspect ratio (width divided by thickness). In most cases, the permeability and porosity inside and outside the channel are unknown variables to be determined simultaneously with the channel geometry. For the largest models treated in this report, there are 248 random variables to be conditioned to pressure data. Because there is insufficient information in the pressure data to uniquely constrain all of the channel variables, we use a Bayesian/Monte Carlo approach which combines prior geologic knowledge of plausible channel shapes with the observed data to generate plausible realizations of channels.

A Levenberg-Marquardt method is used in the conditioning procedure. Efficient

evaluation of the sensitivity of pressure data to channel variables is a critical aspect of our method. We first compute sensitivities of pressure to gridblock permeability and porosity using a variational method, then apply the chain rule to compute sensitivities to channel variables. The method is efficient, typically requiring only 4 to 6 iterations to generate a realization.

Based on the results of synthetic case studies, we found that good estimates of reservoir properties, such as the kh product of the reservoir around the well, the total channel volume or total pore volume, and the flow cross-sectional area of the reservoir around the well could be obtained using pressure data from a single well, provided pressure data during appropriate flow periods are available. For example, the total pore volume of the reservoir could be well resolved if pseudo-steady state pressure data are available. Moreover, conditioning to pressure data, the observed channel thickness and top depth does reduce the uncertainty in the geometric parameters near the well location.

ACKNOWLEDGMENTS

I wish to express my sincere appreciation to my advisors, Dr. Albert C. Reynolds, Jr., Professor of Petroleum Engineering and Mathematical Sciences of the University of Tulsa, and Dr. Dean S. Oliver, Professor of Petroleum Engineering of the University of Tulsa. Without their guidance, support, encouragement and occasional talks whenever needed, this study would not have been completed. My deep gratitude to them for patiently reading through and correcting many half-baked drafts of reports, summaries and dissertation over the last four years. For me, they represent the role models of successful Professors and scientific researchers and it has been an honor having them as my advisors.

I would like to express my sincere thanks to Dr. Richard A. Redner, Professor of Mathematical Department, the University of Tulsa, and Dr. Leslie G. Thompson, Associate Professor of Petroleum Engineering of the University of Tulsa. Professor Redner has made many suggestions that have been tremendously helpful to the DOE project “Geological Architecture Modeling by Markov Random Fields” which I worked on as part of my PhD program. Dr. Thompson has helped me get a good understanding of the well-test issues. I would like also to acknowledge them for serving as my dissertation committee members.

I would like to thank Dr. He, a former PhD student of TUPREP, working for Chevron Petroleum Technology Company. Dr. He developed the 3D single-phase flow

simulator and the program used for calculating sensitivity coefficients of pressure data to permeability and porosity fields of the reservoir. These programs have greatly contributed to the completion of this study.

I have been extremely fortunate in being blessed with good friends and colleagues, Xuri Huang, a gift brother and the best friend, Yula Tang, Fengjun Zhang, George H. Freeman, Yafes Abacioglu and all other Chinese students in the University of Tulsa. I appreciate Mrs. Judy Teal, the secretary of TUPREP, for helping me with many things and being as a big sister of mine.

I am deeply indebted to my wife Xiaoyan Wang and my daughter Yingda Bi, for their constant love, support and understanding. To me, nothing would be possible without their love in my heart.

This work is dedicated to my parents, Tongtai Bi and Fengqin Pi, and all my family members living in China. They are the source of my inspiration. Their encouragement and invaluable support have been the momentum of my life as well as for this study.

I am truly grateful for the financial support provided by the US Department of Energy (DOE), the Strategic Research Department of Mobil and the University f Tulsa Petroleum Reservoir Exploitation Project (TUPREP) during my PhD program.

TABLE OF CONTENTS

TABLE OF CONTENTS (Continued)

TABLE OF CONTENTS (Continued)

LIST OF TABLES

LIST OF FIGURES

LIST OF FIGURES (Continued)

LIST OF FIGURES (Continued)

LIST OF FIGURES (Continued)

LIST OF FIGURES (Continued)

LIST OF FIGURES (Continued)

LIST OF FIGURES (Continued)

LIST OF FIGURES (Continued)

LIST OF FIGURES (Continued)

CHAPTER I

INTRODUCTION

This study focuses on generating a stochastic three-dimensional (3D) channel conditioned to well-test pressure data. To do so, we first formulate a simple stochastic model for generating a single channel within a background facies. The background facies originally occupies a three-dimensional rectangular parallel-piped region (a "box") and a realization of a channel is embedded within this box. For reservoir simulation purposes, a three-dimensional rectangular grid is defined on this box. To simulate a channel, we first generate a principal direction line (PDL). The principal direction line is described by four random variables. The PDL starts at $(0, y_0, z_0)$, where y_0 and z_0 are modeled as Gaussian random variables. To complete the model of the PDL, we also specify the slope of the projection of the PDL on the *x*-*y* plane and the slope of its projection onto the *x*-*z* plane. These slopes are also modeled as Gaussian random variables. We assume that the *x* coordinate of the PDL is such that $0 \le x \le L_x$. Having specified a principal direction line, the channel is parameterized by four correlated Gaussian random fields: the sinuosity in the *x*-*y* plane, the sinuosity in the *x*-*z* plane, the width and aspect ratio. A simulation of each of these Gaussian random fields is generated to obtain values at discrete x_i's (*x*-coordinate of gridblock centers). If (x_i, y, z) denotes the point on the PDL at $x = x_i$, then the center of the channel at $x = x_i$ is obtained by using the two associated sinuosity values to perturb *y* and *z*. The thickness $H(x_i)$ at each x_i is obtained from the values of the width

$W(x_i)$ and aspect ratio $AR(x_i)$. Thus, at each x_i, the cross-section is rectangular and a "panel" of the channel is represented by a box having dimensions $H(x_i)$, $W(x_i)$ and Δx_i. By putting these panels together, we obtain the complete channel. This simple stochastic channel model is based on the work of Georgsen et al. [9, 10].

As we will see, this model offers two main advantages; (i) it is easy to embed the channel within the simulation grid; (ii) it is easy to generate the sensitivity of well-test pressure data to channel model parameters. These sensitivity coefficients are needed in the procedure we use to condition a channel to pressure data.

In conditioning the channel to pressure data, we wish to generate simultaneously realizations of the channel (geometric parameters) and the permeability and porosity fields. The permeability inside the channel is represented by single Gaussian random variable with prescribed mean and variance. Channel porosity and the permeability and porosity in the background facies are modeled in a similar way.

From this point on, model parameters refer to the collection of all stochastic parameters, the four random variables describing the principal direction line, the four Gaussian random fields describing the channel and the four stochastic variables describing the rock property fields. As values of the random fields describing channel geometry are generated only at x_i, $1 \leq i \leq N_x$, the number of model parameters is finite and can be described by a vector which is referred to as the vector of model parameters or simply as the model. This stochastic model is referred to as the prior model. From our specification of model parameters, the probability density function (pdf) for the prior model is well defined. The a posteriori pdf for the model conditioned to pressure data can be obtained from Bayes' theorem.

In order to characterize the uncertainty in model parameters (or in performance predictions), we wish to generate multiple realizations of the model by sampling the a posteriori pdf. Relevant discussions can be found in Tarantola [24], Oliver [18] and Reynolds et al. [23]. In this work, we sample the a posteriori pdf by a method which was briefly mentioned by Kitanidis [15], but was developed within the context of Markov chain Monte Carlo simulation by Oliver et al. [18]; see Reynolds et al. [23] for additional theoretical discussion. Here, we refer to the procedure as the randomized maximum likelihood procedure.

Our emphasis is on generating realizations, not on simply generating the maximum likelihood estimate, i.e., we are more interested in stochastic simulation than estimation. However, it is important to note that others have considered the problem of conditioning a channel to pressure data. In particular, Landa and Horne [17] and Landa [16] considered the problem of conditioning a channel to pressure data. They considered only a simple two-dimensional (*x*-*y*) problem in which the channel boundaries are described by trigonometric functions and are parallel; i.e., the channel width is constant. Since the Landa-Horne model has only a few parameters, the sensitivity coefficients needed to condition a channel to pressure data can be generated by the direct method (gradient simulator), see Anterion et al. [1] and Yeh [27], without too high computational cost. Wu et al. [26] and Wu [25] compared in general terms the computational efficiency of the gradient simulation method and the adjoint method, see Chen et al. [6] and Chavent [5], for generating sensitivity coefficients. For single-phase flow problems, the adjoint method is equivalent to a method proposed by Carter et al. [2, 3]; see Carter et al.'s discussion. In our procedure for generating the sensitivity of pressure data to model

parameters, we use He et al.'s method [12] to compute the sensitivity of pressure data to gridblock permeabilities and porosities. Sensitivity of pressure to model parameters can be computed from these sensitivity values by using the chain rule. As mentioned earlier, a realization of the model is generated by the randomized maximum likelihood method. This requires the minimization of an appropriate objective function. This minimization is accomplished by a Levenberg-Marquardt type algorithm. Typically, the algorithm requires on the order of 10 iterations or less for convergence.

Rahon et al. [22] developed a general procedure for conditioning a geological object to pressure data. They developed an adjoint method to calculate the sensitivity of pressure data to an object shape or boundaries. Their formulation is based on the continuous model, i.e., uses the single-phase flow partial difference equation. When the object is inserted into a simulation grid, the boundary is modeled using a triangulation of the boundary surface. The vertices of these triangles are the parameters modified by conditioning to pressure data. Rahon et al. do not use an a prior probability model to regularize the procedure and thus uses a non-conventional optimization procedure to minimize the objective function. They did not attempt to evaluate the uncertainty in the estimate of model parameters.

The remainder of this dissertation is divided into chapters. Chapter II describes the stochastic model for the channel. Chapter III discusses the prior and a posterior pdf for model parameters, the randomized maximum likelihood procedure and the Levenberg-Marquardt method used to generate realizations. Chapter IV discusses in detail the procedure developed for generating sensitivity coefficients and provides examples. Chapter V presents some synthetic examples where the conditioning data include the

well-test pressure data as well as the channel thickness and top depth observed at the well location. Chapter VI presents the conclusions of this study.

CHAPTER II

GENERATION OF A 3D SINGLE CHANNEL

The model for a single 3D channel follows the basic idea of Georgsen et al. [9, 10]. In this model, the channel is characterized by a parameter set which consists of the principal direction line, horizontal and vertical sinuosity of the centerline of the channel relative to the principal direction line, and the width and aspect ratio (width/thickness) of the channel.

We divide the reservoir under study into gridblocks for flow simulation. We will use the reservoir simulation grid in a (x, y, z) coordinate system throughout the entire process, i.e., the scale for the reservoir properties is the same in channel modeling and flow simulation. We assume that there are N_x, N_y and N_z gridblocks in the x, y and z directions respectively, so that the dimension of the grid is $N_b=N_x \acute{} \ N_y \acute{} \ N_z$. We will use i as the index of the gridblocks in the x-direction, and j and k, respectively, as the gridblock indices in the y and z directions unless stated explicitly otherwise. We assume that there are two homogeneous facies in the reservoir, floodplain facies (outside the channel) and channel fill facies (channel interior).

2.1 Principal Direction Line

The principal direction line is a spatial straight line. It controls the average alignment or main tendency of the channel. We denote the principal direction line of the channel as $_p$, which is described by

$$\ell_p = \{(x_p, y_p, z_p) = (x_0, y_0, z_0) + t(1, s_{xy}, s_{xz})\}, \qquad (2.1)$$

where

x_0 is the x-coordinate of the starting point of ℓ_p and will be set equal to zero,

y_0 and z_0 are the y and z coordinates of the starting point, i.e., the y and z coordinates at the point where the line intersects the $x = x_0$ plane,

t is the argument along ℓ_p which will be set equal to x.

s_{xy} and s_{xz} represent the slopes of ℓ_p projected onto the x-y plane and x-z plane respectively.

Note this is nothing but a parametric representation of a line containing (x_0, y_0, z_0) and having direction numbers (1, s_{xy}, s_{xz}). Note also that y_0, z_0, s_{xy} and s_{xz} are single random variables. We assume that y_0, z_0, s_{xy} and s_{xz} are independent normal random variables and that estimates of the means and variances of these variables are available from geological data or interpretation. Let $\bar{y}_0$, $\bar{z}_0$, $\bar{s}_{xy}$, $\bar{s}_{xz}$ and $s^2_{y_0}$, $s^2_{z_0}$, $s^2_{s_{xy}}$, $s^2_{s_{xz}}$ denote the means and variances of the corresponding normal variables, so that the following probability distribution functions (pdf's) apply:

$$f(y_0) = \frac{1}{\sqrt{2\pi}\, s_{y_0}} \exp\left\{ -\frac{(y_0 - \bar{y}_0)^2}{2 s^2_{y_0}} \right\}, \qquad (2.2.1)$$

$$f(z_0) = \frac{1}{\sqrt{2\pi}\, s_{z_0}} \exp\left\{ -\frac{(z_0 - \bar{z}_0)^2}{2 s^2_{z_0}} \right\}, \qquad (2.2.2)$$

$$f(s_{xy}) = \frac{1}{\sqrt{2\pi}\, s_{s_{xy}}} \exp\left\{ -\frac{(s_{xy} - \bar{s}_{xy})^2}{2 s^2_{s_{xy}}} \right\}, \qquad (2.2.3)$$

$$f(s_{xz}) = \frac{1}{\sqrt{2p}\, s_{s_{xz}}} \exp\left\{ -\frac{(s_{xz} - \bar{s}_{xz})^2}{2 s^{\,2}_{s_{xz}}} \right\}. \qquad (2.2.4)$$

As the random variables are Gaussian, the variables can be sampled very easily.

Figs. 2.1 (a) and (b) illustrate the projections of the principal direction line in the *x*-*y* and *x*-*z* plane, respectively. A realization of the principal direction line in 3D space for $\bar{y}_0 = 30,\ \bar{z}_0 = 60,\ \bar{s}_{xy} = 0.2,\ \bar{s}_{xz} = 0.0,\ s^{\,2}_{y_0} = 1,\ s^{\,2}_{z_0} = 1,\ s^{\,2}_{s_{xy}} = 0.0001$ and $s^{\,2}_{s_{xz}} = 0.001$ is shown in red in Fig. 2.2.

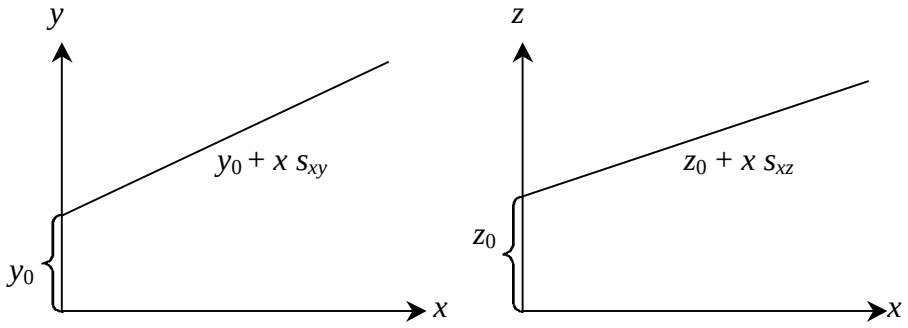

(a) Projection in *x*-*y* plane. (b) Projection in *x*-*z* plane.

Fig. 2.1 – Projections of the principal direction line.

2.2 Center of the Channel

The center $_c$ of the channel is defined by two one-dimensional Gaussian random fields called the horizontal sinuosity and vertical sinuosity, denoted by S_h and S_v respectively. Horizontal sinuosity here is defined as the deviation of the center from the principal direction line in the *y*-direction and similarly the vertical sinuosity is the deviation of the channel center from the principal direction line in the *z*-direction. These definitions are slightly different from the definition of sinuosity in geology. These two fields vary with the *x*-coordinate, i.e., $S_h = S_h(x_i)$ and $S_v = S_v(x_i)$. Each of these Gaussian

random fields, S_h or S_v, has zero mean and a covariance function that describes the correlation length and variability. Gaussian covariance functions will be used for both of these fields because they generate smooth channel paths. One might choose other covariance functions, such as spherical and exponential or some combination of these functions [19].

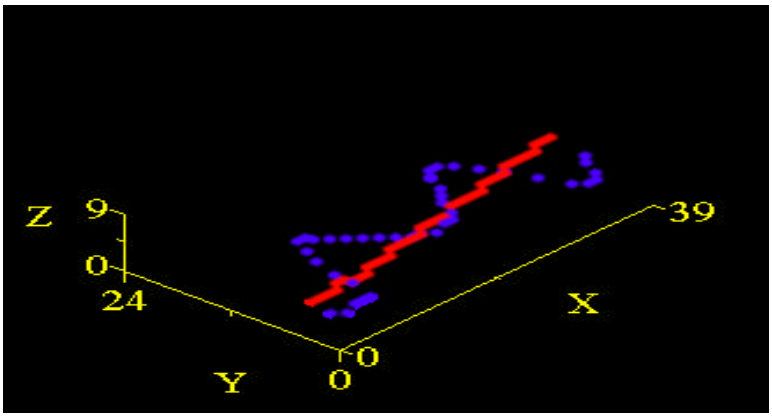

Fig. 2.2 – Principal direction line (red) and center-line (blue) of the channel.

We simulate these fields by the moving average method or filter method [13,14,19]. Assuming a Gaussian covariance function, the horizontal sinuosity S_h and vertical sinuosity S_v are defined as follows.

$$S_h(x) : E\{S_h(x)\} = 0.0,$$
$$Cov\{S_h(x), S_h(x')\} = s^2_{S_h} \exp\left\{-\left(\frac{x - x'}{a_{S_h}}\right)^2\right\}. \tag{2.3}$$

$$S_v(x) : E\{S_v(x)\} = 0.0,$$

and

$$Cov\{S_v(x), S_v(x')\} = s^2_{S_v} \exp\left\{-\left(\frac{x - x'}{a_{S_v}}\right)^2\right\}. \tag{2.4}$$

where E and Cov represent expectation and covariance operators, respectively, and $s^2_{S_h}$ and $s^2_{S_v}$, respectively, are the variances of S_h and S_v. The parameters a_{S_h} and a_{S_v}, respectively, are related to the correlation lengths of the two fields (the ranges of the covariance functions), which are about $\sqrt{3}\, a_{S_h}$ and $\sqrt{3}\, a_{S_v}$, respectively.

Since $S_h(x)$ and $S_v(x)$ are defined relative to the principal line, we can calculate the coordinates of the channel center $_c$ based on both the coordinates of $_p$ and the definition of S_h and S_v.

$$\ell_c = \{(x_p, y_p + S_h(x_p), z_p + S_v(x_p))\}. \tag{2.5}$$

Note that S_h and S_v are both functions of the x-coordinate, i.e., S_h=$S_h(x)$ and S_v= $S_v(x)$, because we have specified the x-direction as the alignment direction of the channel. Therefore, the dimensions of $S_h(x)$ and $S_v(x)$ on the simulation grid are actually the number of gridblocks in the x-direction.

An example of the centerline of a channel is shown in Fig. 2.2 as the blue line on a uniform grid with the gridblock size in all directions equal to 10 ft. The corresponding parameters are $s^2_{S_h} = 900.0\ \text{ft}^2$, $s^2_{S_v} = 4.0\ \text{ft}^2$, $a_{S_h} = a_{S_h} = 46.2$ ft.

2.3 Width *W*(*x*) and Aspect Ratio *AR*(*x*) of the Channel

Other properties of the channel include the width W and aspect ratio AR. The aspect ratio, by definition, is the ratio of the width to the thickness of the channel. Since we have chosen the x direction to represent the main direction of the channel, we will assume W and AR are functions of x only. We let $x_{i-1/2}$ and $x_{i+1/2}$ denote the boundaries of all gridblocks centered at (x_i, y_j, z_k) for all j and k such that $1 \le j \le N_y$, $1 \le k \le N_z$. For $x_{i-1/2} \le$

$x \le x_{i+1/2}$, we set $W(x)=W(x_i)$ and $AR(x)=AR(x_i)$. The width does not vary in the vertical direction and the thickness does not vary in the *y*-direction. Therefore, for any value of *x*, the cross-section of the channel in the *y*-*z* plane is rectangular and symmetric to the centerline of the channel. The width and aspect ratio are also modeled as 1D correlated Gaussian random fields with specified expected values and covariance functions. Instead of using the aspect ratio to define model parameters, Georgsen et al. [9,10] used channel thickness directly. Replacing the aspect ratio by thickness would make some calculations more straightforward in our case. Geologically, however, using the aspect ratio appears more appropriate because channel width and thickness for meandering channels on broad floodplains are stable and quantitatively related. In this study, width, $W(x)$, and aspect ratio, $AR(x)$, are multivariate Gaussian random vectors with

$$E\{W(x)\} = m_w, \tag{2.6.1}$$

$$Cov\{W(x), W(x')\} = s_W^2 \exp\left\{-\left(\frac{x-x'}{a_W}\right)^2\right\}; \tag{2.6.2}$$

$$E\{AR(x)\} = m_{AR}, \tag{2.7.1}$$

$$Cov\{AR(x), AR(x')\} = s_{AR}^2 \exp\left\{-\left(\frac{x-x'}{a_{AR}}\right)^2\right\}, \tag{2.7.2}$$

where m_W and m_{AR}, respectively, are the expected values of *W(x)* and *AR(x)*, *x* and x' are two points along the channel center in the *x* direction, s_W^2 and s_{AR}^2, respectively, denote the variances of *W(x)* and *AR(x)*, and a_W and a_{AR}, respectively, are related to the ranges of the covariance functions for *W(x)* and *AR(x)*. Fig. 2.3 gives a schematic cross-section of the gridded reservoir for a fixed *x* coordinate as well as the relationships of the channel

parameters described above. Notice that the boundaries of the channel do not necessarily coincide with gridblock boundaries, since all channel parameters will be determined by the real coordinates rather than the grid indices. We will refer to the gridblocks intersected by the channel boundaries as boundary gridblocks. As will be seen in later chapters, the permeability and porosity for such gridblocks will be defined by a volumetric average.

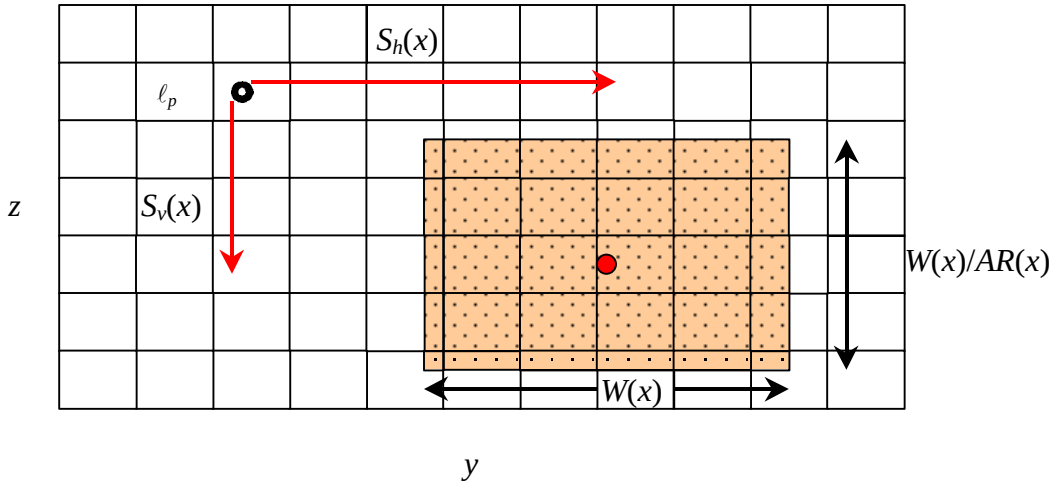

Fig. 2.3 – A *y*-*z* cross-section of the gridded reservoir at any *x* that shows the relationship between the model parameters of a single channel. (⊙ is the intersection of the principal direction line and *x* plane; ● represents the intersection of the centerline and *x* plane)

2.4 Moving Average Method for Simulating 1D Gaussian Random Fields

As discussed above, $S_h(x)$, $S_v(x)$, $W(x)$ and $AR(x)$ are assumed to be 1D Gaussian random fields with known covariance functions. To generate unconditional realizations of the 3D channel on the simulation grid, we must simulate these four random fields. To do so, the moving average method is applied since it is easy to implement and computationally inexpensive.

The idea of this method is that if the imposed covariance function of a second order stationary random field can be written as a convolution product of a function f and its transpose f^T, i.e.,

$$C(x) = f * f^T = \int_{-\infty}^{+\infty} f(u) f(x+u) du , \tag{2.8}$$

where the transpose of f is defined by $f^T(u) = f(-u)$, then a correlated random field $Y(x)$ with covariance function $C(x)$ and zero expectation can be generated by the convolution of the known function f with a one-dimensional stationary random field $Z(x)$ with a Dirac covariance measure, i.e.,

$$Y(x) = \int_{-\infty}^{+\infty} f(x-u) Z(u) du . \tag{2.9}$$

Notice that the convolution in Eq. 2.8 looks different from the general expression for the convolution of two functions. For example, the convolution for two functions, f and g, is normally written as

$$(f * g)(x) = \int_{-\infty}^{\infty} f(u) g(x-u) du = \int_{-\infty}^{\infty} g(u) f(x-u) du = (g * f)(x) . \tag{2.10}$$

Setting $g = f^T$ and applying $f^T(u) = f(-u)$, we have,

$$C(x) = f * f^T = \int_{-\infty}^{\infty} f(u) f^T(x-u) du = \int_{-\infty}^{\infty} f(u) f(u-x) du . \tag{2.11}$$

Making the change of variable $v = u-x$ in Eq. 2.11gives

$$C(x) = f * f^T = \int_{-\infty}^{\infty} f(v+x) f(v) dv = \int_{-\infty}^{\infty} f(u) f(u+x) du , \tag{2.12}$$

which is the form used in Eq. 2.8.

Next, we show that $Y(x)$ given by Eq. 2.9 has the same expectation and variance as the field we wish to simulate. Then, we derive the discrete approximation of Eq. 2.9 that we will use for simulation.

Suppose that we wish to simulate a stationary random field $Y(x)$ with zero mean and covariance function $C(x)$ given by Eq. 2.8. Note that if $E[Y(x)] = m \neq 0$, one can simply define a stationary function $U = Y\text{-}m$ and simulate U. To get a realization of Y, one simply needs to add m to the realization of U.

Taking the expectation of Eq. 2.9 gives

$$E[Y(x)] = \int_{-\infty}^{\infty} f(x-u)E[Z(u)du] = 0. \tag{2.13}$$

The covariance of $Y(x)$ is given by

$$\begin{aligned} C(h) &= C[Y(x), Y(x+h)] = E[Y(x)Y(x+h)] \\ &= E\left[\int_{-\infty}^{\infty} f(x-u)Z(u)du \int_{-\infty}^{\infty} f(x+h-v)Z(v)dv\right] \\ &= \int_{-\infty}^{\infty}\int_{-\infty}^{\infty} f(x-u)f(x+h-v)E[Z(u)Z(v)dudv]. \end{aligned} \tag{2.14}$$

Assume that $Z(u)\mathrm{d}u$ is a Dirac covariance measure with $E[Z(u)\mathrm{d}u] = 0$ and such that $\mathrm{E}[Z(u)\mathrm{d}u\ Z(u)\mathrm{d}\ u]$ equals $s^2\mathrm{d}u$ if $u = u$ and equals zero if $u \neq u$. Using these relations and assuming that $Z(u)\mathrm{d}u$ is chosen so that $s^2 = 1$, Eq. 2.14 can be written as

$$C(h) = C[Y(x), Y(x+h)] = \int_{-\infty}^{\infty} f(x-u)\,f(x+h-u)du. \tag{2.15}$$

Making the change of variable $v = x\text{-}u$, Eq. 2.15 becomes

$$C(h) = C[Y(x), Y(x+h)] = -\int_{\infty}^{-\infty} f(v)\,f(v+h)dv = \int_{-\infty}^{\infty} f(v)\,f(v+h)dv, \tag{2.16}$$

which is identical to Eq. 2.8. Thus, we have shown that the random field $Y(x)$ has zero expectation and its covariance is given by Eq. 2.8.

We would like to construct realizations of $Y(x)$ at an array of discrete points, x_i, i = 1, 2,…, N_x. Moreover, we want to approximate the integral of Eq. 2.9 by a discrete sum. Applying the trapezoidal rule in Eq. 2.9 with $x = x_i$ gives

$$\begin{aligned} Y(x_i) &= \int_{-\infty}^{\infty} f(x_i - u)Z(u)du = \sum_{\ell=-\infty}^{\infty} \int_{u_\ell}^{u_{\ell+1}} f(x_i - u)Z(u)du \\ &= \sum_{\ell=-\infty}^{\infty} \left[\frac{f(x_i - u_\ell)Z(u_\ell) + f(x_i - u_{\ell+1})Z(u_{\ell+1})}{2} \right] (u_{\ell+1} - u_\ell). \end{aligned} \tag{2.17}$$

Since the same values of f Z appear in two consecutive terms in the infinite sum, letting $Z_\ell = Z(u_\ell)$ and $\Delta u = u_{\ell+1} - u_\ell$ for all ℓ, we can rewrite Eq. 2.17 as

$$Y(x_i) = \sum_{\ell=-\infty}^{\infty} f(x_i - u_\ell)Z_\ell \Delta u\,. \tag{2.18}$$

Making the change $k = \ell - i$ in the index of summation of Eq. 2.18 gives

$$Y(x_i) = \sum_{k=-\infty}^{\infty} f(x_i - u_{k+i})Z_{k+i} \Delta u\,. \tag{2.19}$$

Now assuming $x_i = i\Delta x$, $u_j = j\Delta u$ and $\Delta x = \Delta u$ for all integers i and j, Eq. 2.19 becomes

$$\begin{aligned} Y(x_i) &= \sum_{k=-\infty}^{\infty} f(i\Delta x - (k+i)\Delta x)Z_{k+i}\Delta x \\ &= \sum_{k=-\infty}^{\infty} f(-k\Delta x)Z_{k+i}\Delta x. \end{aligned} \tag{2.20}$$

If we make the change of variable $k = \ell + i$ in Eq. 2.18, we can show that

$$Y(x_i) = \sum_{k=-\infty}^{\infty} f(k\Delta x)Z_{i-k}\Delta x\,. \tag{2.21}$$

Note that Eq. 2.9 implies $Y(x) = f * Z$, i.e., y_i is the convolution of function f and the random field Z. In fact, we can also prove that $Y(x) = f^T * Z = Z * f^T$ is a Gaussian random

field with mean 0 and covariance equal to $f^T * f$. The discrete approximation for $Y(x)$ in this case could be obtained by the same procedure and given by

$$Y(x_i) = \sum_{k=-\infty}^{\infty} f(k\Delta x) Z_{i+k} \Delta x . \tag{2.22}$$

Therefore, we can use any one of the preceding three equations to generate the discrete random field, $Y(x_i)$. However, Eq. 2.22 will be used for the results presented in this work.

Now we choose Z_i, i=1,2,…, to be independent identically distributed random variables with zero mean and variance $s^2_{\Delta x}$. Clearly, the expectation of $Y(x_i)$ is zero. The covariance of the random field $Y_i = Y(x_i)$ given by Eq. 2.22 is

$$\begin{aligned} C(j) &= E\left[Y(x_i)Y(x_{i+j})\right] \\ &= E\left[\sum_{k=-\infty}^{\infty} f(k\Delta x) Z_{i+k} \Delta x \sum_{l=-\infty}^{\infty} f(l\Delta x) Z_{i+j+l} \Delta x\right] \\ &= \sum_{k=-\infty}^{\infty} \sum_{l=-\infty}^{\infty} f(k\Delta x) f(l\Delta x) E(Z_{i+k} Z_{i+j+l}) (\Delta x)^2 . \end{aligned} \tag{2.23}$$

Making the change of summation index $n = l+j$ gives

$$\begin{aligned} C(j) &= E\left[Y(x_i)Y(x_{i+j})\right] \\ &= \sum_{k=-\infty}^{\infty} \sum_{n=-\infty}^{\infty} f[k\Delta x] f[(n-j)\Delta x] E(Z_{i+k} Z_{i+n}) (\Delta x)^2 . \end{aligned} \tag{2.24}$$

Since $E[Z_{i+k} Z_{i+n}] = 0$, if $n \neq k$ and $E[Z_{i+k} Z_{i+n}] = s^2_{\Delta x}$, if $n = k$, Eq. 2.24 reduces to

$$\begin{aligned} C(j) &= E\left[Y(x_i)Y(x_{i+j})\right] \\ &= \sum_{k=-\infty}^{\infty} f[k\Delta x] f[(k-j)\Delta x] s^2_{\Delta x} (\Delta x)^2 . \end{aligned} \tag{2.25}$$

The variance denoted by $Var[Y_i]$ is obtained by setting j=0 and is given by

$$Var[Y_i] = C(0) = \sum_{k=-\infty}^{\infty} f(k\Delta x) f(k\Delta x) s^2_{\Delta x} (\Delta x)^2 . \tag{2.26}$$

As Δx will be determined by the grid discretization, it seems clear that we should choose $s^2_{\Delta x}$ so that the variance given by Eq. 2.26 represents the discrete approximation of the variance of the continuous random field $Y(x)$.

Denote the variance of $Y(x)$ by $Var[Y(x)]$, from Eq. 2.8, we have,

$$Var[Y(x)] = C(0) = \int_{-\infty}^{\infty} f(u) f(u) du . \tag{2.27}$$

Using the trapezoidal rule approximation as in Eq. 2.17 to approximate Eq. 2.27 and setting $\Delta u = \Delta x$ give

$$\begin{aligned} Var[Y(x_i)] &= \sum_{k=-\infty}^{\infty} f(u_k) f(u_k) \Delta u = \sum_{k=-\infty}^{\infty} f(k\Delta u) f(k\Delta u) \Delta u \\ &= \sum_{k=-\infty}^{\infty} f(k\Delta x) f(k\Delta x) \Delta x. \end{aligned} \tag{2.28}$$

Comparing Eqs. 2.28 and 2.26, we see that

$$Var[Y_i] = (s^2_{\Delta x} \Delta x) Var[Y(x_i)], \tag{2.29}$$

where $s^2_{\Delta x}$ is the variance of all the Z_i variables. Thus, we should choose the variance of the Z_i as equal to $1/\Delta x$, i.e., $s^2_{\Delta x} = 1/\Delta x$ in order to ensure that $Var[y(x_i)]=Var[y_i]$.

From this point on, we assume that the discrete random field Z_i is a vector of independent realizations of a normal random variable with mean 0 and variance $1/\Delta x$. We denote these discrete values of $Z(x)$ as z_i. The values of a random field $Y(x)$ of interest, e.g., $S_h(x)$, $S_v(x)$, $W(x)$ or $AR(x)$, can be calculated by a discrete form of Eq. 2.9, i.e., Eq. 2.22, which is repeated here as

$$y_i = \sum_{k=-\infty}^{+\infty} z_{i+k} f(k\Delta x) \Delta x , \tag{2.30}$$

where Δx is the grid block size in the x-direction. The value of z_i corresponding to k=0, is assigned to the same point as the value y_i. This method is useful only when the weights, $f(k\Delta x)$, (also known as filter coefficients since the summation in Eq. 2.30 can be considered as a numerical filter), reduce rapidly to zero as $|k|$ increases so that the sum can be taken over a relatively small interval, say k~[-20,20]. For a Gaussian covariance function in one dimension,

$$C(r) = s^2 \exp\left\{-\frac{r^2}{a^2}\right\}, \tag{2.31}$$

where $r = |x\text{-}x|$ represents the distance between x and x, $f(r)$ is calculated as

$$f(r) = s\left(\frac{4}{a^2 p}\right)^{0.25} \exp\left(-\frac{2r^2}{a^2}\right). \tag{2.32}$$

For the problem considered here, s is the standard deviation of the correlated random variables of interest; $Y(x)$, r represents the distance between two points of the simulation grid in the x-direction and a is proportional to the correlation length of the random field, i.e., represents the a terms in Eqs. 2.3 and 2.4. In order to gain some knowledge about how many terms must be summed in Eq. 2.30 to approximate y_i accurately, the exponential part of Eq. 2.32 is plotted in Fig. 2.4 for different values of $\Delta x/a$. In Fig. 2.4, we have plotted $\exp\left[-2(k\Delta x/a)^2\right]$ versus k. Note that we may approximate Eq. 2.30 by

$$y_i = \sum_{k=-k_{\max}}^{k_{\max}} z_{i+k}\, f(k\Delta x)\Delta x, \tag{2.33}$$

where $k_{\max}$=1.5($a/\Delta x$).

Fig. 2.5 presents a realization of the discrete random field $AR(i)$ generated by using Eq. 2.33 and the corresponding normal field Z_i for i=1,2,…,40.

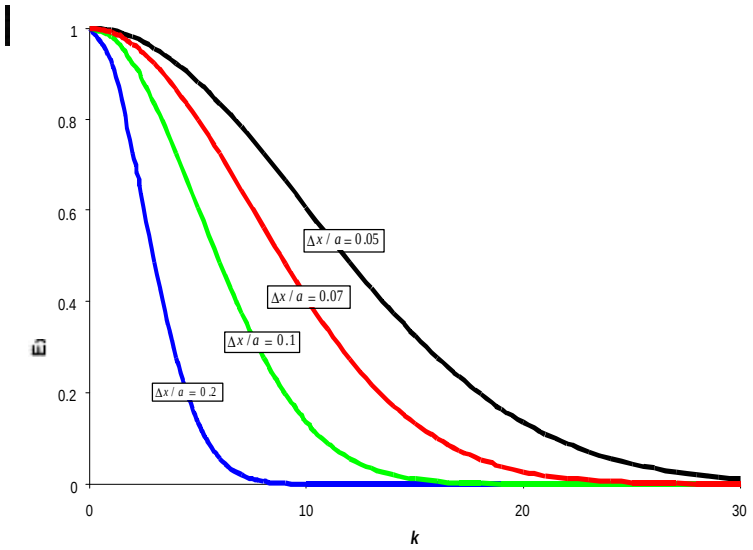

Fig. 2.4 – Exponential functions for different $\Delta x/a$ values.

In Fig. 2.5, Δx =10 ft was used. Therefore, $E(Z_i)$ = 0.0, and $Var[Z_i]$ = $1/\Delta x$ = 0.1. The expectation and variance of the *AR* are 1.5 and 0.025. The sample mean and variance of the y_i generated from Eq. 2.33 are 1.456 and 0.0241, respectively, which are very close to the true values.

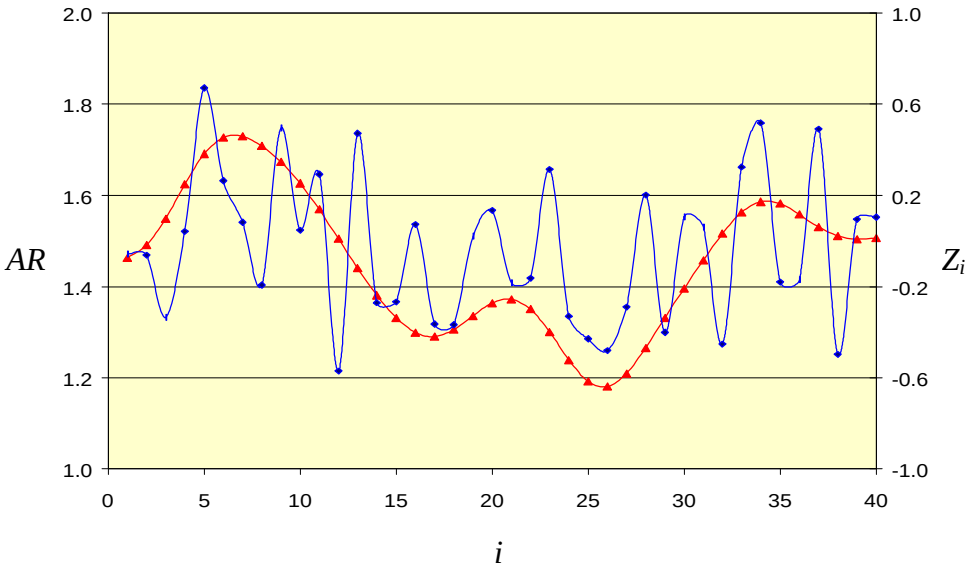

Fig. 2.5 – A realization of $AR(x)$ (triangles) and $Z(x)$ (diamonds).

The values of the function $f(k\Delta x)$ that correspond to Fig. 2.5 are shown in Fig. 2.6 for k = -20~20. As we can see, $f(k\Delta x)$ decays rapidly as $|k|$ increases. When $|k|>9$, $f(k\Delta x)$ is essentially zero. Note also that the function $f(k\Delta x)$ is symmetric in this case.

For other commonly used covariance functions, e.g., spherical and exponential functions, the expressions for $f(r)$'s are given in Refs. [13], [14] and [19].

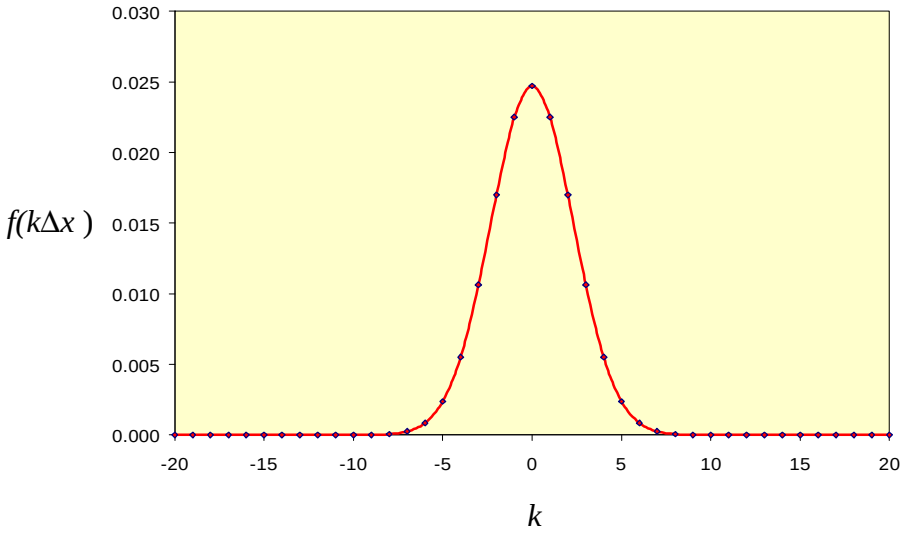

Fig. 2.6 – The function $f(k\Delta x)$ corresponding to Fig. 2.5.

Fig. 2.7 shows a realization of a 3D single channel on a simulation grid. The dimension of the grid is 40×25×10 and each gridblock is 10ft × 10ft ×10ft. In generating this realization, the following values of the model parameters were used.

Principal direction line: $\bar{y}_0 = 100.0\text{ft},\ \bar{z}_0 = 50.0\text{ft},\ \bar{s}_{xy} = 0.05,\ \bar{s}_{xz} = 0.00,$

$$s^2_{y0} = 1.0,\ s^2_{z0} = 1.0,\ s^2_{s_{xy}} = 0.001,\ s^2_{s_{xz}} = 0.001.$$

Horizontal and vertical sinuosity of the centerline: $s^2_{S_h} = 676.0,\ s^2_{S_v} = 9.0,$

$$a_{S_h} = a_{S_v} = 80.0\text{ft}.$$

Width: $m_W = 80.0\text{ft},\ s^2_W = 9.0,\ a_W = 80.0\text{ft},$

Aspect ratio: $m_{AR} = 2.0,\ s^2_{AR} = 0.025,\ a_W = 80.0\text{ft}.$

In Fig. 2.7, the boundaries of the channel are displayed with different colors. As discussed later, the colors are associated with the values of gridblock permeabilities.

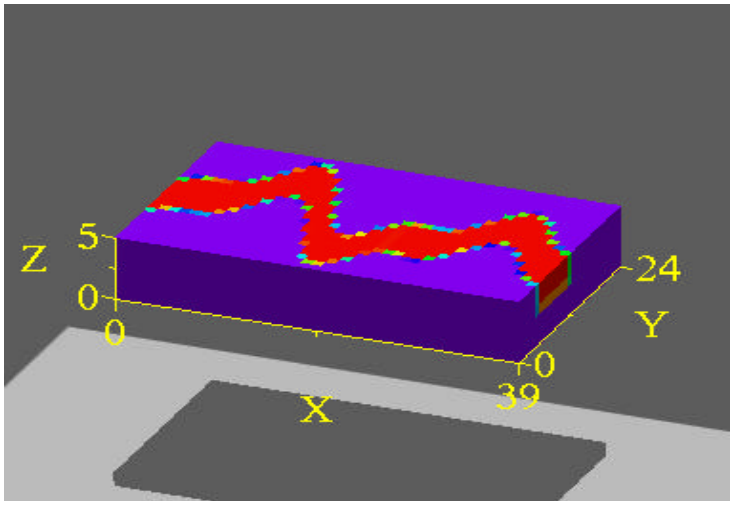

Fig. 2.7 – A realization of a single 3D channel on the simulation grid 40×25×10. Only six vertical gridblocks (z = 0-5) are shown. The scales on the axes are gridblock numbers starting from 0.

CHAPTER III

SIMULATION BY RANDOMIZED MAXIMUM LIKELIHOOD METHOD

In the previous chapter, we discussed the four random variables which define the principal direction line, and the four one-dimensional correlated Gaussian random fields that define the geometric parameters for a channel. In this chapter, we first define the prior probability density function (pdf) for the channel model. Secondly, we consider the case where the set of model parameters includes the permeability and porosity inside and outside the channel. Thirdly, we apply Bayes theorem to obtain the a posteriori pdf conditioned to data. The data can include both pressure data and the channel thickness and top depth observed at the location of a well. Finally, we discuss the sampling of the a posteriori pdf using the randomized maximum likelihood method. Each realization generated by this procedure requires the minimization of an objective function. For the application presented here, a modified Levenberg-Marquardt algorithm was used to perform the minimization.

3.1 The Prior pdf

For the stochastic channel model introduced in the first chapter, the vector of model parameters is $m = m_G$ where

$$m_G = [y_0, z_0, s_{xy}, s_{xz}, S_{h1}, \ldots, S_{h,N_x}, S_{v1}, \ldots, S_{v,N_x}, W_1, \ldots, W_{N_x}, AR_1, \ldots, AR_{N_x}]^T, \quad (3.1)$$

where we have used the subscript G to denote geometric parameters and N_x is the number of simulation gridblocks in the x-direction. Recall the first four entries in m_G represent the four random variables which describe the principal direction line, whereas, S_h, S_v, W and AR are modeled as one-dimensional stationary, correlated random fields which represent, respectively, horizontal sinuosity, vertical sinuosity, width and aspect ratio. Note that m_G is a $4N_x + 4$ dimensional column vector. The expectations (means) and covariances of these random variables and fields were specified in the preceding chapter. We let $m_{G,prior}$ denote the vector of prior means.

We define the 4×4 diagonal matrix C_ℓ by

$$C_\ell = \begin{bmatrix} \sigma^2_{y_0} & & & \\ & \sigma^2_{z_0} & & \\ & & \sigma^2_{s_{xy}} & \\ & & & \sigma^2_{s_{xz}} \end{bmatrix}, \tag{3.2}$$

i.e., C_ℓ is the covariance matrix for the principal direction line.

Let C_{S_h}, C_{S_v}, C_W and C_{AR}, respectively, define the $N_x \times N_x$ covariance matrix for S_h, S_v, W and AR. Then, the prior covariance matrix for the geometric parameters is a block diagonal matrix given by

$$C_G = \begin{bmatrix} C_\ell & & & & \\ & C_{S_h} & & & \\ & & C_{S_v} & & \\ & & & C_W & \\ & & & & C_{AR} \end{bmatrix}. \tag{3.3}$$

In general, we will let C_M denote the overall prior covariance matrix for the model parameters. If the only model parameters are the ones describing the channel geometry, then $C_M = C_G$, $m = m_G$, $m_{prior} = m_{G,prior}$ and the prior pdf is

$$f_M(m) = c\exp\left\{-\frac{1}{2}(m-m_{prior})^T C_M^{-1}(m-m_{prior})\right\}$$
$$= c\exp\left\{-\frac{1}{2}(m_G-m_{G,prior})^T C_G^{-1}(m_G-m_{G,prior})\right\}, \quad (3.4)$$

where c is the normalizing constant.

However, we may also wish to consider the rock properties interior and exterior to a channel as random variables. In this case, we add four random variables, k_c (channel permeability, i.e., the permeability in the channel interior), k_{nc} (permeability of non-channel facies, or simply permeability outside the channel), j_c (channel porosity) and j_{nc} (porosity of non-channel facies).

Letting

$$m_r = [k_c, k_{nc}, j_c, j_{nc}]^T, \quad (3.5)$$

our vector of model parameters is

$$m = \begin{bmatrix} m_G \\ m_r \end{bmatrix}. \quad (3.6)$$

In this work, we model each of the four variables in m_r as Gaussian with prescribed means and variances. For simplicity, we assume these variables are uncorrelated, so the associated covariance matrix, C_R, is diagonal, i.e.,

$$C_R = \begin{bmatrix} s_{k_c}^2 & & & \\ & s_{k_{nc}}^2 & & \\ & & s_{j_c}^2 & \\ & & & s_{j_{nc}}^2 \end{bmatrix}. \quad (3.7)$$

Let $m_{r,prior}$ denote the vector of prior means for these four variables. Our combined vector of the prior mean is

$$m_{prior} = \begin{bmatrix} m_{G,prior} \\ m_{r,prior} \end{bmatrix}, \tag{3.8}$$

and the prior covariance matrix is

$$C_M = \begin{bmatrix} C_G & O \\ O & C_R \end{bmatrix}, \tag{3.9}$$

where throughout submatrices denoted by *O* denote null matrices.

The prior probability density function still has the form

$$f_M(m) = c \exp\left\{-\frac{1}{2}(m - m_{prior})^T C_M^{-1}(m - m_{prior})\right\}. \tag{3.10}$$

where *c* is the normalizing constant.

3.2 A Posteriori Probability Density Function

Here, d_{obs}, denotes the vector of observed data that will be used as conditioning data. This includes pressure data, plus the observed channel thickness and depth of the top of channel at the well, assuming the channel is penetrated by the well. In all cases considered in this work, we assume that the channel is penetrated by a single well. We let d_{obs}^{p} denote the vector of observed pressure data that will be used to condition an unconditional realization of a channel and $d^{p} = g_p(m)$ denote the relation between predicted data and model parameters. Here d^{p} denotes predicted data corresponding to d_{obs}^{p}; i.e., if *m* is the true model and measurements in d_{obs}^{p} are exact, then $d^{p} = d_{obs}^{p}$.

The diagonal matrix $C_{D,p}$ denotes the pressure data covariance matrix. We assume that pressure measurement errors can be modeled as independent, identically distributed Gaussian random variables with mean zero and variance $s_{d,p}^{2}$.

We let H_{obs} denote the observed thickness of the channel at the well location and $z_{obs,t}$ represent the observed value of z at the top of the channel at a well location. We can of course have several wells in the system in which case H_{obs} represents a vector of observed channel thicknesses and $z_{obs,t}$ represents a vector of observed depths of channel tops.

We assume the measurement errors associated with the vector H_{obs} are independent, identically distributed Gaussian random variables with mean zero and variance $s_{d,t}^2$. We let $C_{D,t}$ denote the associated diagonal covariance matrix with all diagonal entries equal to $s_{d,t}^2$. The measurement errors of $z_{obs,t}$ are modeled in a similar way with $C_{D,z}$ representing the diagonal data covariance matrix. The overall data covariance matrix is then the diagonal matrix

$$C_D = \begin{bmatrix} C_{D,p} & 0 & 0 \\ 0 & C_{D,t} & 0 \\ 0 & 0 & C_{D,z} \end{bmatrix}. \tag{3.11}$$

The vector d_{obs} represents the vector which contains all observed data. In the most general case,

$$d_{obs} = \begin{bmatrix} d_{obs}^{p} \\ H_{obs} \\ z_{obs,t} \end{bmatrix}. \tag{3.12}$$

We let d be the corresponding vector of predicted data and let $d = g(m)$ represent the relation between the model m and predicted data, i.e.,

$$d = \begin{bmatrix} d^{p} \\ d^{H} \\ d^{z} \end{bmatrix}. \tag{3.13}$$

If the observed data at a single channel are channel thickness H_{obs} and top depth $z_{obs,t}$ of the channel, the following relations apply:

$$d^H = g_H(m) = \frac{W(x_w)}{AR(x_w)}, \tag{3.14}$$

$$d^z = g_z(m) = z_0 + x_w s_{xz} + \frac{W(x_w)}{2AR(x_w)}, \tag{3.15}$$

where x_w represents the x coordinate of the well. In the multiple well case, d^H and d^z represent the vector corresponding to H_{obs} and $z_{obs,t}$, respectively.

From Bayes theorem, the a posteriori pdf (conditional to observed data), is given by

$$\begin{aligned} p(m) &= c\exp\left\{-\frac{1}{2}(m-m_{prior})^T C_M^{-1}(m-m_{prior}) - \frac{1}{2}(d-d_{obs})^T C_D^{-1}(d-d_{obs})\right\} \\ &= c\exp\{-O(m)\}, \end{aligned} \tag{3.16}$$

where

$$O(m) = \frac{1}{2}(m-m_{prior})^T C_M^{-1}(m-m_{prior}) + \frac{1}{2}(d-d_{obs})^T C_D^{-1}(d-d_{obs}). \tag{3.17}$$

The model m which minimizes $O(m)$, is the maximum a posteriori estimate. However, as in previous work done at the University of Tulsa [8], [21] and [23], we wish to generate a suite of realizations of the model by sampling (m). We use a method discussed in Kitanidis [15], Oliver et al. [18] and Reynolds et al. [21]. We refer to this procedure as the randomized maximum likelihood method. In this procedure, an individual realization is obtained as follows: first, sample the prior pdf for m to calculate an unconditional realization m_{uc}; second, generate an unconditional realization d_{uc} of the data; then minimize

$$O(m) = \frac{1}{2}(m-m_{uc})^T C_M^{-1}(m-m_{uc}) + \frac{1}{2}(d-d_{uc})^T C_D^{-1}(d-d_{uc}), \tag{3.18}$$

to obtain the conditional realization m_c.

The procedure is repeated to generate the specified number of conditional realizations. Unless d is linearly related to the model, this generates only an approximate sampling of the a posteriori pdf.

3.3 Gauss-Newton Algorithm

The objective function, Eq. 3.17, can be minimized by the Gauss-Newton algorithm. The gradient of the objective function $O(m)$ in Eq. 3.17 is given by

$$\nabla O(m) = C_M^{-1}(m - m_{prior}) + \left\{\nabla[d_{obs} - g(m)]^T\right\} C_D^{-1}[d_{obs} - g(m)], \tag{3.19}$$

where $$\nabla[d_{obs} - g(m)]^T = -\nabla[g(m)]^T = -\begin{pmatrix} \frac{\partial g_1(m)}{\partial m_1} & \frac{\partial g_2(m)}{\partial m_1} & \cdots & \frac{\partial g_{N_d}(m)}{\partial m_1} \\ \frac{\partial g_1(m)}{\partial m_2} & \frac{\partial g_2(m)}{\partial m_2} & \cdots & \vdots \\ \vdots & \vdots & \cdots & \vdots \\ \frac{\partial g_1(m)}{\partial m_M} & \frac{\partial g_2(m)}{\partial m_M} & \cdots & \frac{\partial g_{N_d}(m)}{\partial m_M} \end{pmatrix}, \tag{3.20}$$

where g_i is the i[th] component of the N_d-dimensional vector-valued function $g(m)$. Here, N_d is the total number of conditioning data.

If we define the matrix in Eq. 3.20 as G^T, then we have,

$$\nabla[d_{obs} - g(m)]^T = -G^T, \tag{3.21}$$

and $$G = \begin{pmatrix} \frac{\partial g_1(m)}{\partial m_1} & \frac{\partial g_1(m)}{\partial m_2} & \cdots & \frac{\partial g_1(m)}{\partial m_M} \\ \frac{\partial g_2(m)}{\partial m_1} & \frac{\partial g_2(m)}{\partial m_2} & \cdots & \vdots \\ \vdots & \vdots & \cdots & \vdots \\ \frac{\partial g_{N_d}(m)}{\partial m_1} & \frac{\partial g_{N_d}(m)}{\partial m_2} & \cdots & \frac{\partial g_{N_d}(m)}{\partial m_M} \end{pmatrix}. \tag{3.22}$$

The matrix G is referred to as the sensitivity matrix. The efficient computation of this matrix is crucial. We can rewrite Eq. 3.19 in terms of G as

$$\nabla O(m) = C_M^{-1}(m - m_{prior}) + G^T C_D^{-1}[g(m) - d_{obs}]. \tag{3.23}$$

The Hessian matrix of $O(m)$ is given by

$$H(m) = \nabla\left[(\nabla O(m))^T\right] = C_M^{-1} + G^T C_D^{-1} G + \left(\nabla G^T\right) C_D^{-1}\left(g(m) - d_{obs}\right). \tag{3.24}$$

However, in the Gauss-Newton algorithm, this matrix is approximated by

$$H(m) \cong C_M^{-1} + G^T C_D^{-1} G. \tag{3.25}$$

Since C_M and C_D are positive definite, this approximate Hessian matrix is also positive definite.

The Gauss-Newton algorithm solves

$$H(m^k) dm^k = -\nabla O(m^k), \tag{3.26}$$

for dm^k and sets

$$m^{k+1} = m^k + m_k dm^k, \tag{3.27}$$

where k stands for the iteration index and m_k is the step size that is determined by a line search or restricted-step algorithm. In our work, we actually use a modified Levenberg-Marquardt algorithm to minimize the objective function. This eliminates the necessity to perform a line search. This algorithm has proved to be a very effective way to solve nonlinear problems. Another advantage of the algorithm is that it often enhances the stability of the approximated Hessian matrix.

3.4 Levenberg-Marquardt Algorithm

The Levenberg-Marquardt algorithm can be thought of as a modification of the Gauss-Newton algorithm. Assume that in the Gauss-Newton algorithm, we use m_{prior} as

an initial guess of the model parameters which gives a large pressure data mismatch. In this case, we often obtain a rough model m^1 at the first iteration. Once a model "estimate" becomes too rough, it is difficult to correct it at later iterations. Moreover, in such situations, the Gauss-Newton method often converges to a local minimum which gives an unacceptable match of the data. We wish to avoid this problem. Borrowing the idea of the Levenberg-Marquardt algorithm, we can either "increase" the data variances so as to reduce the effect of huge data mismatch or modify the Gauss-Newton procedure. We use a modified Levenberg-Marquardt algorithm which is written as

$$\begin{aligned}\left\{(1+\alpha)C_M^{-1}+G^T C_D^{-1}G\right\}dm^{k+1} = &-C_M^{-1}(m^k - m_{prior})\\ &-G^T C_D^{-1}\left(g(m)-d_{obs}\right),\end{aligned} \tag{3.28}$$

where α is a positive number. Note by making α sufficient large, we can make $\|dm^{k+1}\|$ small and thus control the change in model parameters over an iteration. This procedure tends to result in smoother change in model parameters and appears to reduce the chance of becoming trapped in a local minimum which gives a unacceptable data mismatch.

To obtain an expression for dm^{k+1}, we divide Eq. 3.28 by $(1+\alpha)$ which gives

$$\begin{aligned}\left\{C_M^{-1}+\frac{1}{1+\alpha}G^T C_D^{-1}G\right\}dm^{k+1} = \frac{1}{1+\alpha}\{ &-C_M^{-1}(m^k - m_{prior}) -\\ &G^T C_D^{-1}\left(g(m)-d_{obs}\right)\ \}.\end{aligned} \tag{3.29}$$

Letting $C_{DM} = (1+\alpha)C_D$, it follows that

$$C_{DM}^{-1} = \frac{1}{1+\alpha}C_D^{-1}. \tag{3.30}$$

Substituting Eq. 3.30 into Eq. 3.29, we have,

$$\begin{aligned}\left\{C_M^{-1}+G^T C_{DM}^{-1}G\right\}dm^{k+1} = -\frac{1}{1+\alpha}\{ &\ C_M^{-1}(m^k - m_{prior}) +\\ &G^T C_{DM}^{-1}(1+\alpha)\left(g(m)-d_{obs}\right)\ \}.\end{aligned} \tag{3.31}$$

From a matrix inverse lemma [24]

$$\left[C_M^{-1} + G^T C_{DM}^{-1} G\right]^{-1} = C_M - C_M G^T \left[C_{DM} + G C_M G^T\right]^{-1} G C_M, \tag{3.32}$$

so that

$$\begin{aligned} &\left[C_M^{-1} + G^T C_{DM}^{-1} G\right]^{-1} C_M^{-1}(m^k - m_{prior}) \\ &\quad = \left\{C_M - C_M G^T \left[C_{DM} + G C_M G^T\right]^{-1} G C_M\right\} C_M^{-1}(m^k - m_{prior}) \\ &\quad = (m^k - m_{prior}) - C_M G^T \left[C_{DM} + G C_M G^T\right]^{-1} G(m^k - m_{prior}). \end{aligned} \tag{3.33}$$

From basic matrix algebra, the following matrix identity can be established,

$$\left[C_M^{-1} + G^T C_D^{-1} G\right]^{-1} G^T C_D^{-1} = C_M G^T \left[C_D + G C_M G^T\right]^{-1}. \tag{3.34}$$

Therefore,

$$\begin{aligned} &\left[C_M^{-1} + G^T C_{DM}^{-1} G\right]^{-1} G^T C_{DM}^{-1} (1+a)(g(m) - d_{obs}) \\ &\qquad = (1+a) C_M G^T \left[C_{DM} + G C_M G^T\right]^{-1} (g(m) - d_{obs}). \end{aligned} \tag{3.35}$$

Substituting Eq. 3.33 and 3.35 into 3.31 gives

$$\begin{aligned} dm^{k+1} = &-\frac{m^k - m_{prior}}{(1+a)} + \\ &\frac{1}{1+a} C_M G^T \left[C_{DM} + G C_M G^T\right]^{-1} \left\{G(m^k - m_{prior}) - (1+a)(g(m) - d_{obs})\right\}. \end{aligned} \tag{3.36}$$

Replacing C_{DM} by $(1+a)C_D$, it follows,

$$\begin{aligned} dm^{k+1} = &-\frac{m^k - m_{prior}}{(1+a)} + \\ &C_M G^T \left[(1+a) C_D + G C_M G^T\right]^{-1} \left\{\frac{G(m^k - m_{prior})}{1+a} - (g(m) - d_{obs})\right\}. \end{aligned} \tag{3.37}$$

The detailed Levenberg-Marquardt algorithm for channel inversion is given below.

1. k = 0: set a_0 to be a big number, say 10000; form m_{prior}, m^0, and the covariance matrices, C_D and C_M. In all the case studies of this work, we wish to generate

realizations from the a posteriori pdf by the randomized maximum likelihood method. Therefore, we replace m_{prior} and d_{obs} in Eq. 3.37 by an unconditional realization of them, respectively, i.e., m_{uc}, d_{uc}.

2. $k = k+1$: calculate pressure response $g_p(m^k)$ by using a reservoir simulator; evaluate objective function $O_k = O(m^k)$ according to Eq. 3.17 and calculate sensitivity matrix G_k.
3. Evaluate dm^{k+1} from Eq. 3.37. Then propose the model by $m^{k+1} = m^k + dm^{k+1}$ and calculate $O_{k+1} = O(m^{k+1})$.
4. Check to see if $O(m^{k+1}) < O(m^k)$. If so, accept m^{k+1}, and decrease a_k by a factor of 10, i.e., $a_{k+1} = a_k/10$, then check the convergence criteria. If one of them is satisfied, then stop iterating; otherwise, go to step 2 for another iteration.
5. If it is not satisfied, increase a_k by a factor of 10, i.e., $a_k = a_k \times 10$, then go to step 3.

A few remarks regarding this algorithm follow.

1) We use three convergence criteria to stop the iteration. The first one is the data error variance. If the estimated pressure data error variance is less than the specified data variance $s^2_{d,p}$, i.e., if

$$\frac{1}{N_p}\sum_{i=1}^{N_p}[g_p(m^k) - d^p_{obs,i}]^2 \le s^2_{d,p}, \tag{3.38}$$

then we assume that the algorithm has converged. Another convergence criterion is that if the change in the objective function over an iteration is negligible, i.e.,

$$\frac{|O_{k+1} - O_k|}{O_k + 10^{-14}} < e, \tag{3.39}$$

where e is a very small number, say 10^{-5}.

If the number of iterations exceeds the specified maximum number of iterations without satisfying either convergence criteria, the algorithm is also forced to stop even though it has not converged. Typically, we specify the maximum number of iterations allowed as 10.

2) The calculated pressure response $g_p(m^k)$ is obtained by a 3D single-phase flow simulator which is discussed in He [11]. The porosity and permeability fields for flow simulation are provided by the stochastic channel generator based on the model parameters. We use a volume average to calculate the porosity and permeability of a gridblock intersected by one or more channel boundaries.

3) Modification of the a value is done within each iteration (if necessary) and the updated value will be used for the next iteration. Most of the researchers have recommended using a smaller starting value of a, say 0.001. We use a larger starting value of a such that the model change is smoother from the beginning of the algorithm.

CHAPTER IV

COMPUTATION OF SENSITIVITY COEFFICIENTS

As described in the last two chapters, we wish to generate realizations of the channel model parameters, which honor the well test pressure data, channel thickness and top depth observed at well locations. We do this by minimizing an appropriate objective function by a modified Levenberg-Marquardt algorithm, which essentially interpolates between the steepest descent and Gauss-Newton algorithms, based on some practical considerations. The implementation of this algorithm requires only computation of the objective function $O(m)$ and its gradient and Hessian, for both of which the sensitivity matrix G is required. As the sensitivity of hard data to model parameters can be easily calculated directly, we consider the case where $d = g(m)$ represented only pressure data. Physically speaking, each entry of G, i.e., $(\partial g_i(m)/\partial m_j)$, measures the change of pressure $p_i = g_i(m)$ due to a small perturbation of model parameter m_j. For example, $\frac{\partial p_3}{\partial m_2}$ represents how the calculated pressure corresponding to the 3rd measured pressure $p_{obs,3}$ changes with the 2nd model parameter m_2. Recall that m_2 represents the z coordinate of the starting point of the principal direction line, i.e., z_0, according to the ordering of model parameters. Efficient calculation of the G matrix is the key element of the entire inversion process.

It is well known that the pressure response of a reservoir is a function of reservoir properties, fluid properties and production time. The mathematical model for this process is governed by a set of differential equations and usually solved by numerical simulation.

The most important reservoir properties are the porosity and permeability fields. Since we use a numerical reservoir simulator for flow simulation, we need the porosity and permeability values in each gridblock of the reservoir grid. Much relevant work [11], [12], [18] and [21], has focused on how to find the maximum a posteriori estimate or realizations of the porosity and permeability distribution. In the channel inversion problem however, the model parameters also include the random variables that describe the geometry of the 3D channel. The porosity and permeability fields are intermediate variables that convey the information in channel model parameters to the pressure response. It is natural to apply the chain rule to compute derivatives of pressure with respect to channel parameters. In this chapter, we discuss how to calculate porosity and permeability distributions based on a set of channel parameters and present the procedure for calculating sensitivity coefficients.

4.1 Computation of Porosity and Permeability Fields

As described in Chapter II, a 3D channel is modeled by four normal random variables and four Gaussian random fields. For convenience, we have taken the x-direction as the main direction of the channel. Therefore, the four Gaussian random fields are all random functions of the x-coordinate. The cross-section of the channel at any value of x, is rectangular. But cross-sectional area may vary with x. Fig. 4.1 shows an y-z cross-section of the channel on a reservoir grid at a fixed value of x. It should be noted that the boundaries of the channel do not necessarily coincide with the grid lines of the

reservoir grid. If the boundaries are between the grid lines, part of the corresponding gridblocks are within the channel and part of them are outside the channel. We need a way to handle these gridblocks in order to distribute porosity and permeability fields on the entire grid. To simplify notation, let us denote the boundaries of the channel by $T_m(x)$ (top boundary), $B_m(x)$ (bottom boundary), $L_m(x)$ (left boundary) and $R_m(x)$ (right boundary) as shown in Fig. 4.1.

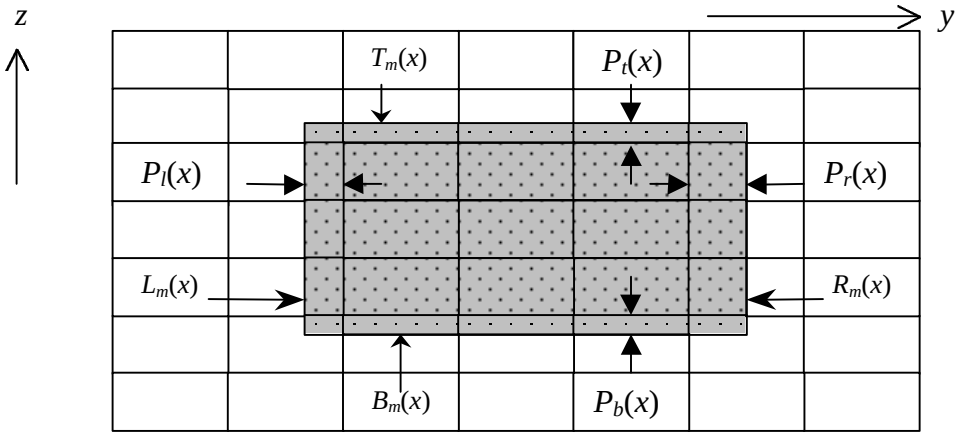

Fig. 4.1 – A cross-section of a gridded reservoir shows a cross-section of the channel and its boundaries.

These boundaries can be expressed as functions of the model parameters as follows.

$$T_m(x) = z_0 + x\, s_{xz} + S_v(x) + \left(0.5W(x)/AR(x)\right), \tag{4.1}$$

$$B_m(x) = z_0 + x\, s_{xz} + S_v(x) - \left(0.5W(x)/AR(x)\right), \tag{4.2}$$

$$L_m(x) = y_0 + x\, s_{xy} + S_h(x) - 0.5W(x), \tag{4.3}$$

$$R_m(x) = y_0 + x\, s_{xy} + S_h(x) + 0.5W(x). \tag{4.4}$$

Along each boundary and for a given x, the proportions of the gridblocks inside the channel are similar and can be determined very easily given the values of the boundary variables and the size of the grid blocks in each direction. Denote $P_t(x)$ and $P_b(x)$ as the

length of the channel interior in the top and bottom boundary gridblocks, respectively. Similarly denote $P_l(x)$ and $P_r(x)$ as the length of the channel interior within the left and right boundary gridblocks, as illustrated in Fig. 4.1.

$P_t(x)$, $P_b(x)$, $P_l(x)$ and $P_r(x)$ are very easy to compute. For example, $P_t(x)$ can be calculated by

$$P_t(x) = T_m(x)/\Delta z - \text{int}[T_m(x)/\Delta z], \tag{4.5}$$

where int represents the operation of taking the integer part.

Assume that we can use the volume-weighted average to calculate the porosity and permeability for all the gridblocks of the channel boundaries. For example, if the total volume of a boundary gridblock is V and the volumes of the parts of the gridblock inside and outside the channel are V_{i} and V_{o} respectively, then the porosity j and permeability k of this gridblock are calculated by,

$$j = \frac{V_i}{V} j_{\mathrm{c}} + \frac{V_o}{V} j_{\mathrm{nc}}, \tag{4.6}$$

$$\mathrm{k} = \frac{V_i}{V} \mathrm{k}_{\mathrm{c}} + \frac{V_o}{V} \mathrm{k}_{\mathrm{nc}}, \tag{4.7}$$

where j_{c}, $\mathrm{k_c}$, j_{nc} and $\mathrm{k_{nc}}$ are the porosity and permeability inside and outside the channel, respectively. Determination of V_i and V_o for a boundary gridblock is straightforward if $P_t(x)$, $P_b(x)$, $P_l(x)$ and $P_r(x)$ are known. Fig. 4.2 shows a 3D gridblock on the bottom boundary of the channel. If this block is not on the corners, V_i and V_o for this block can be calculated as follows:

$$V_i = \Delta x \times \Delta y \times P_b(x), \tag{4.8}$$

$$V_o = \Delta x \times \Delta y \times (\Delta z - P_b(x)). \tag{4.9}$$

For the gridblock on the lower left corner, we will have,

$$V_i = \Delta x \times P_l(x) \times P_b(x), \tag{4.10}$$

$$V_o = \Delta x \times [\Delta y \Delta z - P_l(x) P_b(x)]. \tag{4.11}$$

We can calculate V_i and V_o for all the boundary gridblocks in the same way as above.

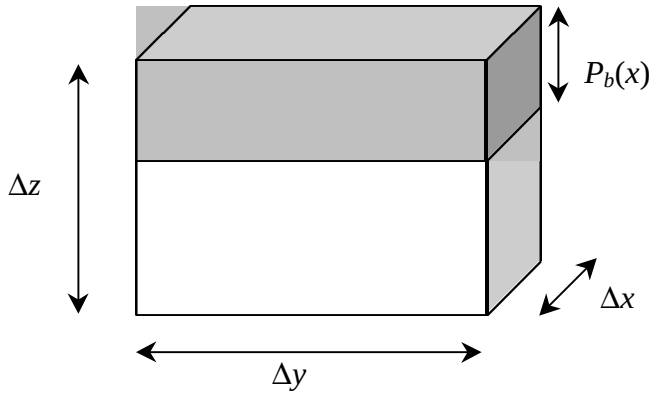

Fig. 4.2 – A 3D gridblock on the bottom boundary of the channel, Δx, Δy and Δz are the gridblock size for this particular block in the x, y and z directions.

For the porosity and permeability inside and out of the channel, we either use specified constant values or specify prior Gaussian distributions for porosity and permeability.

Although this is an ad hoc treatment, it turns out that it is very effective. One might question the validity of this treatment, especially for permeability, which does not exhibit any volume additive property in nature. One could, of course, use another procedure such as geometric average to compute permeability for boundary gridblocks. Since it is not the major purpose of this study, we will assume that the volume-weighted average is appropriate.

In Fig. 2.7 of Chapter II, we note that the channel boundaries appear as different colors, which actually reflects the permeability values determined by the above volume-weighted averages along the boundaries. In that case, we used a constant value of 100md

for channel permeability and a constant permeability value of 1md for the facies out of the channel.

4.2 Computation of Sensitivities

For channel inversion, the main sensitivity coefficients of interest are the derivatives of the well-test pressure data with respect to the channel parameters, i.e., $\frac{\partial p}{\partial y_0}, \frac{\partial p}{\partial z_0}, \frac{\partial p}{\partial s_{xy}}, \frac{\partial p}{\partial s_{xz}}, \left\{ \frac{\partial p}{\partial S_{hi}}, \frac{\partial p}{\partial S_{vi}}, \frac{\partial p}{\partial W_i}, \frac{\partial p}{\partial AR_i}, i = 1,2,...,N_x \right\}$ and the derivative with respect to the rock properties. If we also condition the observed channel thickness and top depth at well locations, then sensitivities include the derivative of the predicted channel thickness and top depth at wells with respect to other model parameters (width and aspect ratio, etc.). Since we have no way to establish a direct relationship between pressure response obtained in well testing and the channel parameters, we have to take advantage of the porosity field $\Phi(m)$ and the permeability field $K(m)$ induced from the channel parameters as a two-stage bridge. On the first stage, we will connect our "input" model parameters to the "output" pressure response, i.e., $p(m) = p[K(m), \Phi(m)]$ where m is the model parameter vector. In the second stage, we use the chain rule to construct the desired sensitivities.

Here, we assume that the data consist of only pressure data. If p_i is the i^{th} observed pressure data and m_j is the j^{th} model parameter, then the entry in the i^{th} row and j^{th} column of the sensitivity matrix G is given by

$$G_{ij} = \frac{\partial p_i}{\partial m_j} = \sum_{b=1}^{N_b} \left(\frac{\partial p_i}{\partial \mathrm{k}_b} \frac{\partial \mathrm{k}_b}{\partial m_j} + \frac{\partial p_i}{\partial j_b} \frac{\partial j_b}{\partial m_j} \right), \tag{4.12}$$

where N_b is the number of simulation gridblocks, and k_b and j_b, respectively, denote the permeability and porosity in the b^{th} gridblock.

Letting K denote the vector of gridblock permeabilities, K=K(m), and Φ the vector of gridblock porosities, $\Phi=\Phi(m)$, then Eq. 4.12 can be written as

$$G_{ij} = [\nabla_{\mathrm{K}} p_i]^T \frac{\partial \mathrm{K}}{\partial m_j} + [\nabla_{\Phi} p_i]^T \frac{\partial \Phi}{\partial m_j}. \tag{4.13}$$

We let $\partial p/\partial \mathrm{K}$ denote the $N_p \times N_b$ matrix with i^{th} row given by $[\nabla_{\mathrm{K}} p_i]^T$, $\partial p/\partial \Phi$ denote the $N_p \times N_b$ matrix with i^{th} row given by $[\nabla_{\Phi} p_i]^T$. Let $\partial \mathrm{K}/\partial m$ denote the $N_b \times M$ matrix with j^{th} column given by $\partial \mathrm{K}/\partial m_j$ and let $\partial \Phi/\partial m$ denote the $N_b \times M$ matrix with j^{th} column given by $\partial \Phi/\partial m_j$, then with this notation, it follows from Eq. 4.13 that the sensitivity coefficient matrix associated with pressure data is given by

$$G = \frac{\partial p}{\partial m} = \frac{\partial p}{\partial \mathrm{K}} \frac{\partial \mathrm{K}}{\partial m} + \frac{\partial p}{\partial \Phi} \frac{\partial \Phi}{\partial m}. \tag{4.14}$$

It seems that these matrices may require a large amount of computer memory if the number of simulation gridblocks is large. For example, if we use a 40×25×10 grid, N_b=10000, and $M=4N_x+4=164$, so $(\partial \mathrm{K}/\partial m)$ and $(\partial \Phi/\partial m)$ are both 10000×164 matrices. We will see in the next section, however, most of the entries of these matrices are zero so that we do not need to store them.

4.2.1 Computation of Sensitivities of Pressure to Porosity and Permeability

In this study, the sensitivities of observed pressure with respect to porosity and permeability, i.e., $\partial p/\partial \mathrm{K}$ and $\partial p/\partial \Phi$, are calculated with the three-dimensional extension of the Carter et al. method described by He [11]. Since the procedure utilizes a unit source pressure response as well as its spatial and time derivatives, careful selection of

the time step for simulation and sensitivity calculation is needed to avoid negative sensitivity values induced by numerical truncation error. This may occur because the unit source pressure drop might be too small to make meaningful calculations of the spatial and time derivatives. Detailed description about this method and its numerical implementation are given in [11].

4.2.2 General Formula for $\partial K/\partial m$ and $\partial \Phi/\partial m$

The matrices, $\partial K/\partial m$ and $\partial \Phi/\partial m$, by definition, contain the sensitivities of gridblock permeability and porosity to the model parameters in m. The definition of the prior model for channel geometry provides us an explicit relationship between $K(m)$, $\Phi(m)$ and the model parameter vector m, through the definitions of the boundaries. An interesting phenomenon is that if m_j is one of the parameters describing the channel, then $\partial k_b/\partial m_j = 0$ unless the gridblock associated with k_b contains a channel boundary. This observation provides a straightforward way to calculate the desired sensitivities. In fact, if we define the channel boundaries $T_m(x)$, $B_m(x)$, $L_m(x)$ and $R_m(x)$ in terms of the model parameters, which was done in the last chapter, then we need only to know how the porosity and permeability near the channel boundaries change as these boundaries vary in space, i.e., $\partial K/\partial T_m$, $\partial K/\partial B_m$, $\partial K/\partial L_m$, $\partial K/\partial R_m$, $\partial \Phi/\partial T_m$, $\partial \Phi/\partial B_m$, $\partial \Phi/\partial L_m$ and $\partial \Phi/\partial R_m$, because analytical evaluation of the derivatives of $T_m(x)$, $B_m(x)$, $L_m(x)$ and $R_m(x)$ with respect to model parameters is straightforward. Here, T_m, B_m, L_m and R_m, respectively, represent the vectors of top, bottom, left and right boundary of the channel with the dimension equal to the number of gridblocks in the x-direction, e.g., $T_m = \{T_{mi}, i=1,2,\ldots, N_x\}$.

In order to keep the equations neat, we will still use matrix notation. Further application of the chain rule gives,

$$\frac{\partial \mathrm{K}}{\partial m} = \frac{\partial \mathrm{K}}{\partial T_m}\frac{\partial T_m}{\partial m} + \frac{\partial \mathrm{K}}{\partial B_m}\frac{\partial B_m}{\partial m} + \frac{\partial \mathrm{K}}{\partial L_m}\frac{\partial L_m}{\partial m} + \frac{\partial \mathrm{K}}{\partial R_m}\frac{\partial R_m}{\partial m}, \tag{4.15}$$

and

$$\frac{\partial \Phi}{\partial m} = \frac{\partial \Phi}{\partial T_m}\frac{\partial T_m}{\partial m} + \frac{\partial \Phi}{\partial B_m}\frac{\partial B_m}{\partial m} + \frac{\partial \Phi}{\partial L_m}\frac{\partial L_m}{\partial m} + \frac{\partial \Phi}{\partial R_m}\frac{\partial R_m}{\partial m}. \tag{4.16}$$

Substituting Eqs. 4.15 and 4.16 into 4.14 will finally give the sensitivity matrix G that is required for channel inversion.

As a summary, Tables 4.1 and 4.2 list the dimensions of all the vectors and matrices defined so far.

4.2.3 Calculation of Boundary Sensitivities to Model Parameters

Since we have already defined the relationships between the boundaries of the channel, i.e., $T_m(x)$, $B_m(x)$, $L_m(x)$ and $R_m(x)$, and the model parameters in Eqs. 4.1 through 4.4, it is very simple to calculate the derivatives of $T_m(x)$, $B_m(x)$, $L_m(x)$ and $R_m(x)$ with respect to the model parameters.

Let us record again the expressions for $T_m(x)$, $B_m(x)$, $L_m(x)$ and $R_m(x)$ given by Eqs 4.1 through 4.4.

$$T_m(x) = z_0 + x\, s_{xz} + S_v(x) + \left(0.5W(x)/AR(x)\right), \tag{4.17}$$

$$B_m(x) = z_0 + x\, s_{xz} + S_v(x) - \left(0.5W(x)/AR(x)\right), \tag{4.18}$$

$$L_m(x) = y_0 + x\, s_{xy} + S_h(x) - 0.5W(x), \tag{4.19}$$

$$R_m(x) = y_0 + x\, s_{xy} + S_h(x) + 0.5W(x). \tag{4.20}$$

Recall that T_{mi} represents the top boundary of the channel at gridblock i in the x-direction and W_j is the channel width of the gridblock j in the x-direction. x_i is the value of the x-coordinate of gridblock i in the x-direction.

The derivatives of these boundaries can be readily obtained as follows:

Table 4.1 Dimensions of the vectors

Vector	Dimension
Model parameters, *m and* m_{prior}	M, M
Observed Pressure, $p=p_{obs}$	N_p
Observed Thickness, H_{obs}	N_T
Centerline Sinuosities, S_h and S_v	N_x, N_x
Channel Width, W	N_x
Channel Aspect ratio, AR	N_x
Channel Boundaries, T_m, B_m	N_x, N_x
Channel Boundaries, L_m, R_m	N_x, N_x
Porosity field, Φ	N_b
Permeability field, K	N_b

Table 4.2 Dimensions of the Matrices

Matrix	Dimension
Data Covariance Matrix, C_D	$N_d \acute{} N_d$
Model Covariance Matrix, C_M	$M \acute{} M$
Sensitivity Matrix, G	$N_d \acute{} M$
$\partial p/\partial K$, $\partial p/\partial \Phi$	$N_d \acute{} N_b$
$\partial K/\partial m$, $\partial \Phi/\partial m$	$N_b \acute{} M$
$\partial K/\partial T_m$,$\partial K/\partial B_m$, $\partial K/\partial L_m$,$\partial K/\partial R_m$	$N_b \acute{} N_x$
$\partial \Phi/\partial T_m$,$\partial \Phi/\partial B_m$, $\partial \Phi/\partial L_m$,$\partial \Phi/\partial R_m$	$N_b \acute{} N_x$
$\partial T_m/\partial m$,$\partial B_m/\partial m$,$\partial L_m/\partial m$,$\partial R_m/\partial m$	$N_x \acute{} M$

$$\frac{\partial T_{mi}}{\partial y_0} = 0, \frac{\partial T_{mi}}{\partial z_0} = 1, \frac{\partial T_{mi}}{\partial s_{xy}} = 0, \frac{\partial T_{mi}}{\partial s_{xz}} = x_i \quad for\ i = 1,2,...,N_x; \tag{4.21}$$

For i, j=1, 2, …, N_x,

$$\frac{\partial T_{mi}}{\partial S_{hj}} = 0; \tag{4.22}$$

$$\frac{\partial T_{mi}}{\partial S_{vj}} = \begin{cases} 1 & if\ \ j = i \\ 0 & otherwise \end{cases}; \tag{4.23}$$

$$\frac{\partial T_{mi}}{\partial W_j} = \begin{cases} 0.5/AR_i & if\ \ j = i \\ 0 & otherwise \end{cases}; \tag{4.24}$$

$$\frac{\partial T_{mi}}{\partial AR_j} = \begin{cases} -0.5W_i/AR_i^2 & if\ \ j = i \\ 0 & otherwise \end{cases}; \tag{4.25}$$

where i and j are both indices of the gridblocks in the x-direction.

Similarly, we have, for the derivatives of B_{mi},

$$\frac{\partial B_{mi}}{\partial y_0} = 0, \frac{\partial B_{mi}}{\partial z_0} = 1, \frac{\partial B_{mi}}{\partial s_{xy}} = 0, \frac{\partial B_{mi}}{\partial s_{xz}} = x_i \quad for\ i = 1,2,...,N_x; \tag{4.26}$$

For i, j=1, 2, …, N_x,

$$\frac{\partial B_{mi}}{\partial S_{hj}} = 0; \tag{4.27}$$

$$\frac{\partial B_{mi}}{\partial S_{vj}} = \begin{cases} 1 & if\ \ j = i \\ 0 & otherwise \end{cases}; \tag{4.28}$$

$$\frac{\partial B_{mi}}{\partial W_j} = \begin{cases} -0.5/AR_i & if\ \ j = i \\ 0 & otherwise \end{cases}; \tag{4.29}$$

$$\frac{\partial B_{mi}}{\partial AR_j} = \begin{cases} 0.5W_i/AR_i^2 & if\ \ j = i \\ 0 & otherwise. \end{cases} \tag{4.30}$$

Also for L_{mi} and R_{mi}, i=1, 2, …, N_x,

$$\frac{\partial L_{mi}}{\partial y_0}=1,\ \frac{\partial L_{mi}}{\partial z_0}=0,\ \frac{\partial L_{mi}}{\partial s_{xy}}=x_i,\ \frac{\partial L_{mi}}{\partial s_{xz}}=0 \quad for\ i=1,2,...,N_x; \tag{4.31}$$

For i, j=1, 2, …, N_x,

$$\frac{\partial L_{mi}}{\partial S_{hj}}=\begin{cases}1 & if\ \ j=i\\ 0 & otherwise\end{cases}; \tag{4.32}$$

$$\frac{\partial L_{mi}}{\partial S_{vj}}=0; \tag{4.33}$$

$$\frac{\partial L_{mi}}{\partial W_j}=\begin{cases}-0.5 & if\ \ j=i\\ 0 & otherwise\end{cases}; \tag{4.34}$$

$$\frac{\partial L_{mi}}{\partial AR_j}=0. \tag{4.35}$$

$$\frac{\partial R_{mi}}{\partial y_0}=1,\ \frac{\partial R_{mi}}{\partial z_0}=0,\ \frac{\partial R_{mi}}{\partial s_{xy}}=x_i,\ \frac{\partial R_{mi}}{\partial s_{xz}}=0 \quad for\ i=1,2,...,N_x; \tag{4.36}$$

For i, j=1, 2, …, N_x,

$$\frac{\partial R_{mi}}{\partial S_{hj}}=\begin{cases}1 & if\ \ j=i\\ 0 & otherwise\end{cases}; \tag{4.37}$$

$$\frac{\partial R_{mi}}{\partial S_{vj}}=0; \tag{4.38}$$

$$\frac{\partial R_{mi}}{\partial W_j}=\begin{cases}0.5 & if\ \ j=i\\ 0 & otherwise\end{cases}; \tag{4.39}$$

$$\frac{\partial R_{mi}}{\partial AR_j}=0. \tag{4.40}$$

4.2.4 Derivatives of Permeability and Porosity with Respect to Channel Boundaries

These derivatives can be evaluated by a very simple procedure. In order to illustrate this, we consider the calculation of $\partial K/\partial T_m$ only. $\partial K/\partial B_m$, $\partial K/\partial L_m$ and $\partial K/\partial R_m$ can be obtained by a similar procedure to the one shown below. Fig 4.3 shows a cross-section of a channel at the i^{th} gridblock in the x-direction. The top and bottom boundaries for "cross-section i" are T_{mi} and B_{mi} which are located in the k_2^{th} and k_1^{th} gridblocks in the z-direction, respectively, as shown in Fig. 4.3. Assume that the boundaries L_{mi} and R_{mi} are located in j_1^{th} and j_2^{th} gridblocks in the y-direction and that there is an infinitesimal change in T_{mi}, say $\Delta T>0$, as shown in in Fig. 4.3.

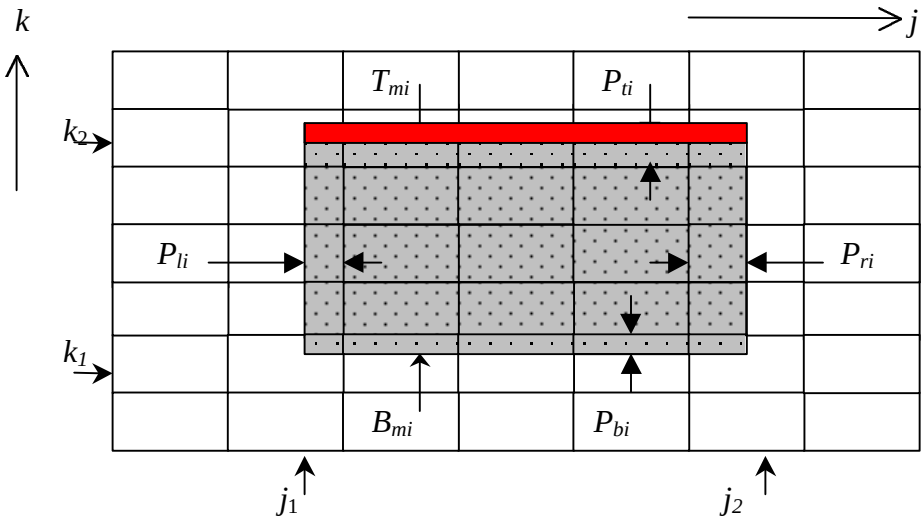

Fig. 4.3 – Illustration of a reservoir cross-section for $\partial K/\partial T_m$ evaluation.

For simplicity, we assume the permeability inside the channel is k_c (constant) and the permeability out of the channel is also a constant and equal to k_{nc}. Throughout, we use the following convention of the gridblock ordering. Let i, j, and k denote the indices for the x, y and z directions, respectively. We start with the first gridblock in the z-direction, i.e., k = 1(bottom layer). Then the y-direction index, j, increases from 1 to N_y.

For each index j, the x-direction index increases from 1 to N_x. The same ordering is repeated for k = 2,3,…,N_z. Therefore, the single index b of any gridblock (i, j, k) in the simulation grid can be computed as $b = (k\text{-}1)N_xN_y+(j\text{-}1)N_x+i$.

As shown in Table 4.2, $\partial K/\partial T_m$ is a $N_b \times N_x$ matrix. Denote any entry of $\partial K/\partial T_m$ by $\partial k_b/\partial T_{mi\ell}$ for b=1, 2,…, N_b and $i\ell$ =1,2,…,N_x. Clearly, $\partial k_b/\partial T_{mi\ell}$ is zero unless $i = i\ell$ and $b = (k_2\text{-}1)N_xN_y+(j\text{-}1)N_x+i$. For $b = (k_2\text{-}1)N_xN_y+(j\text{-}1)N_x+i$, $i\ell = i$ and $j_1 £ j £ j_2$, we have three different cases as explained below.

- Case 1: if j is greater than j_1 and less than j_2, the permeability change ΔK of the gridblocks due to the change of top boundary T_{mi}, denoted by ΔT, can be calculated based on the volume-weighted average as described before, i.e.,

$$\begin{aligned}\Delta K &= \left\{\frac{\Delta x\Delta y(P_{ti}+\Delta T)}{\Delta x\Delta y\Delta z}k_c + \frac{\Delta x\Delta y(\Delta z - P_{ti} - \Delta T)}{\Delta x\Delta y\Delta z}k_{nc}\right\} \\ &\quad - \left\{\frac{\Delta x\Delta y P_{ti}}{\Delta x\Delta y\Delta z}k_c + \frac{\Delta x\Delta y(\Delta z - P_{ti})}{\Delta x\Delta y\Delta z}k_{nc}\right\} \\ &= \frac{(k_c - k_{nc})\Delta T}{\Delta z}.\end{aligned} \tag{4.41}$$

  Therefore, the derivative $\partial k_b/\partial T_{mi\ell}$, by definition, is given by

$$\frac{\partial k_b}{\partial T_{mi'}} = \lim_{\Delta T\to 0}\left(\frac{\Delta K}{\Delta T}\right) = \lim_{\Delta T\to 0}\left(\frac{(k_c - k_{nc})\Delta T}{\Delta z\Delta T}\right) = \frac{(k_c - k_{nc})}{\Delta z}. \tag{4.42}$$

- Case 2: $j = j_1$,

$$\begin{aligned}\Delta K &= \left\{\frac{\Delta x P_{li}(P_{ti}+\Delta T)}{\Delta x\Delta y\Delta z}k_c + \left[1 - \frac{\Delta x P_{li}(P_{ti}+\Delta T)}{\Delta x\Delta y\Delta z}\right]k_{nc}\right\} \\ &\quad - \left\{\frac{\Delta x P_{li}P_{ti}}{\Delta x\Delta y\Delta z}k_c + \left[1 - \frac{\Delta x P_{li}P_{ti}}{\Delta x\Delta y\Delta z}\right]k_{nc}\right\} \\ &= \frac{P_{li}(k_c - k_{nc})\Delta T}{\Delta y\Delta z}.\end{aligned} \tag{4.43}$$

So,
$$\frac{\partial \mathrm{k}_b}{\partial T_{mi'}} = \lim_{\Delta T \to 0}\left(\frac{\Delta \mathrm{K}}{\Delta T}\right) = \lim_{\Delta T \to 0}\left(\frac{P_{li}(\mathrm{k_c} - \mathrm{k_{nc}})\Delta T}{\Delta y \Delta z \Delta T}\right) = \frac{P_{li}(\mathrm{k_c} - \mathrm{k_{nc}})}{\Delta y \Delta z}. \tag{4.44}$$

- Case 3: $j = j_2$, replacing P_{li} with P_{ri} in Eq. 4.44 gives,

$$\frac{\partial \mathrm{k}_b}{\partial T_{mi'}} = \frac{P_{ri}(\mathrm{k_c} - \mathrm{k_{nc}})}{\Delta y \Delta z}. \tag{4.45}$$

Evaluation of $\partial \mathrm{K}/\partial B_m$ can be done following the same procedure except that the $\Delta \mathrm{B}<0.0$ is used because we have taken the positive z-direction from bottom to the top of the reservoir grid, as shown in Fig. 4.4. Consequently, all the expressions of $\partial \mathrm{k_b}/\partial B_{mi\ell}$ for the same three cases as above should have opposite signs compared to Eqs. 4.42, 4.44 and 4.45. We omit those derivations. Instead, we write the expressions for $\partial \mathrm{k_b}/\partial B_{mi\ell}$ by substituting $(\mathrm{k_{nc}}\text{-}\mathrm{k_c})$ for $(\mathrm{k_c}\text{-}\mathrm{k_{nc}})$ in the above equations.

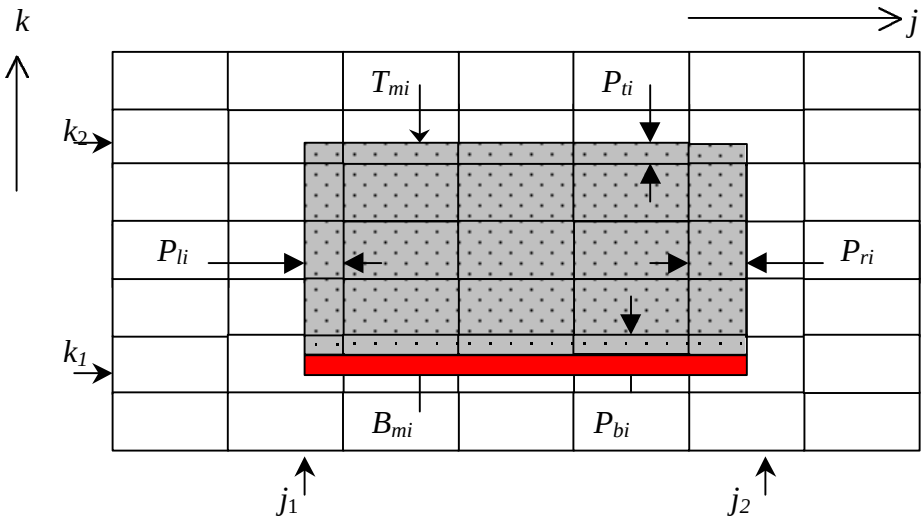

Fig. 4.4 - Illustration of a reservoir cross-section for $\partial \mathrm{K}/\partial B_m$ evaluation.

For $b = (k_1\text{-}1)N_xN_y+(j\text{-}1)N_x+i$ and $i\text{¢} = i$,

$$\frac{\partial \mathrm{k}_b}{\partial B_{mi'}} = \begin{cases} 0.0 & \text{if } j < j_1 \text{ or } j > j_2; \\ \dfrac{(\mathrm{k_{nc}} - \mathrm{k_c})}{\Delta z} & \text{if } j_1 < j < j_2; \\ \dfrac{P_{li}(\mathrm{k_{nc}} - \mathrm{k_c})}{\Delta y \Delta z} & \text{if } j = j_1; \\ \dfrac{P_{ri}(\mathrm{k_{nc}} - \mathrm{k_c})}{\Delta y \Delta z} & \text{if } j = j_2. \end{cases} \tag{4.46}$$

Similarly, if $b \neq (k\text{-}1)N_xN_y + (j_2\text{-}1)N_x + i$ or $i\text{¢} \neq i$, then $\partial \mathrm{k_b}/\partial R_{mi\text{¢}} = 0$, $\partial \mathrm{k_b}/\partial L_{mi\text{¢}} = 0$; otherwise, if $b = (k\text{-}1)N_xN_y+(j_1\text{-}1)N_x+i$ and $i\text{¢} = i$, then,

$$\frac{\partial \mathrm{k}_b}{\partial L_{mi'}} = \begin{cases} 0.0 & \text{if } k < k_1 \text{ or } k > k_2; \\ \dfrac{(\mathrm{k_{nc}} - \mathrm{k_c})}{\Delta y} & \text{if } k_1 < k < k_2; \\ \dfrac{P_{bi}(\mathrm{k_{nc}} - \mathrm{k_c})}{\Delta y \Delta z} & \text{if } k = k_1; \\ \dfrac{P_{ti}(\mathrm{k_{nc}} - \mathrm{k_c})}{\Delta y \Delta z} & \text{if } k = k_2. \end{cases} \tag{4.47}$$

Also, if $b = (k\text{-}1)N_xN_y+(j_2\text{-}1)N_x+i$ and $i\text{¢} = i$, then,

$$\frac{\partial \mathrm{k}_b}{\partial R_{mi'}} = \begin{cases} 0.0 & \text{if } k < k_1 \text{ or } k > k_2; \\ \dfrac{(\mathrm{k_c} - \mathrm{k_{nc}})}{\Delta y} & \text{if } k_1 < k < k_2; \\ \dfrac{P_{bi}(\mathrm{k_c} - \mathrm{k_{nc}})}{\Delta y \Delta z} & \text{if } k = k_1; \\ \dfrac{P_{ti}(\mathrm{k_c} - \mathrm{k_{nc}})}{\Delta y \Delta z} & \text{if } k = k_2. \end{cases} \tag{4.48}$$

A few remarks on the above formula are given below.

1) The gridblock size in each direction, i.e., Δx, Δy and Δz, are considered to be uniform in the above derivations. If non-uniform gridblock sizes for each direction are used, then Δy and Δz should be based on gridblock b in the above formula.

2) Rather than use constant permeability both inside and out of the channel, we could specify some permeability distribution such as normal permeability distribution. In this case, the formulas for $\partial k_b/\partial T_{mi¢}$, $\partial k_b/\partial B_{mi¢}$, $\partial k_b/\partial R_{mi¢}$ and $\partial k_b/\partial L_{mi¢}$ are still similar. But the permeabilities k_c and k_{nc} in all the above equations should be the permeabilities for the gridblocks that correspond to the indices *b* and *i¢*.

3) Since we apply the volume-weighted average for both permeability and porosity calculations for the boundary gridblocks, the expressions for the derivatives of porosity with respect to the boundaries, i.e., $\partial\Phi/\partial T_m$, $\partial\Phi/\partial B_m$, $\partial\Phi/\partial L_m$ and $\partial\Phi/\partial L_m$, can be obtained following exactly the same procedure and are identical to the expressions for $\partial K/\partial T_m$, $\partial K/\partial B_m$, $\partial K/\partial L_m$ and $\partial K/\partial L_m$ with permeability replaced by porosity. Specifically, we can just replace K, k_c and k_{nc} with Φ, j_c and j_{nc} in Eqs. 4.42, 4.44 and 4.45 through 4.48 for the computation of $\partial\Phi/\partial T_m$, $\partial\Phi/\partial B_m$, $\partial\Phi/\partial L_m$ and $\partial\Phi/\partial L_m$, where j_c and j_{nc} are the porosity values inside and outside the channel. Again, we could specify some probability distribution for porosity.

4) If permeability and porosity both inside and outside of the channel are taken as model parameters (unknowns), the sensitivity of gridblock permeability and porosity to model parameters is also required. This will be discussed in Chapter V where an example is given.

4.2.5 Derivatives of Channel Thickness with Respect to Model Parameters

Generally, the channel thickness and the top depth of the channel are also available from core data or well logs. In addition to conditioning to the well-test pressure data, we would condition the model to these observations. An effective way to condition to the observed thickness at the well and to the top boundary of the channel is to include these

observations with the pressures and incorporate them into the objective function as shown below.

$$\begin{aligned}&\left(H_{obs}-g_H(m)\right)^T C_{D,t}^{-1}\left(H_{obs}-g_H(m)\right)\\&+\left(z_{obs,t}-z_t(m)\right)^T C_{D,z}^{-1}\left(z_{obs,t}-z_t(m)\right),\end{aligned} \tag{4.49}$$

where H_{obs} and $z_{obs,t}$ represent the observed thickness and top depth of the channel. $g_H(m)$ and $z_t(m)$ are the calculated channel thickness and top and $C_{D,t}$ and $C_{D,z}$ are the corresponding data covariances. It is necessary to calculate the sensitivity of $g_H(m)$, i.e., the calculated channel thickness, to the model parameters. Instead of specifying channel thickness as model parameters directly, we have specified aspect ratio $AR(x)$, which is the ratio of channel width to channel thickness. If we assume that the well is vertical, then $g_H(m)$ can be calculated by

$$g_H(m)=\frac{W(x)}{AR(x)}, \tag{4.50}$$

where, $AR(x)=0$ is prohibited. Calculation of $\partial g_H(m)/\partial m$ is as follows:

$$\frac{\partial g_H(m)}{\partial m_1}=\frac{\partial g_H(m)}{\partial y_0}=0, \tag{4.51}$$

$$\frac{\partial g_H(m)}{\partial m_2}=\frac{\partial g_H(m)}{\partial z_0}=0, \tag{4.52}$$

$$\frac{\partial g_H(m)}{\partial m_3}=\frac{\partial g_H(m)}{\partial s_{xy}}=0, \tag{4.53}$$

$$\frac{\partial g_H(m)}{\partial m_4}=\frac{\partial g_H(m)}{\partial s_{xz}}=0, \tag{4.54}$$

and for $i=1,2,\ldots,N_x$,

$$\frac{\partial g_H(m)}{\partial m_{i+4}}=\frac{\partial g_H(m)}{\partial S_{hi}}=0, \tag{4.55}$$

$$\frac{\partial g_H(m)}{\partial m_{i+4+N_x}} = \frac{\partial g_H(m)}{\partial S_{vi}} = 0\,, \tag{4.56}$$

$$\frac{\partial g_H(m)}{\partial m_{i+4+2N_x}} = \frac{\partial g_H(m)}{\partial W_i} = \begin{cases} \dfrac{1}{AR_i} & if\ \ i = iwell \\ 0 & otherwise. \end{cases} \tag{4.57}$$

$$\frac{\partial g_H(m)}{\partial m_{i+4+3N_x}} = \frac{\partial g_H(m)}{\partial AR_i} = \begin{cases} -\dfrac{W_i}{AR_i^2} & if\ \ i = iwell \\ 0 & otherwise \end{cases} \tag{4.58}$$

where *iwell* is the *x*-coordinate of the well.

When we evaluate these derivatives, we need to know whether the well penetrates the channel or not, especially if we have multiple wells, because the above computation only makes sense when the channel is fully penetrated by the well.

The derivatives of $z_t(m)$ with respect to the model parameters have been obtained in the last section (since $z_t(m)=T_m(x)$). Certainly, we need only to evaluate $\partial z_t(m)/\partial m$ at the well locations for this purpose.

Some examples of the sensitivity coefficients will be given in the next section. It should be mentioned that although the evaluation of these sensitivities is extremely simple and effective, intuitively, the dimensions of the matrices are very large if there are a larger number of gridblocks. However, it is not necessary to store all components, because most of the components are zero. For example, assume a 40×25×10 grid, then $\partial K/\partial T_m$ and $\partial \Phi/\partial T_m$ are $N_b \times N_x$ = 10,000×40 matrices. However, if the average width of the channel is 15 gridblocks, we have only about 40×15 nonzero values in $\partial K/\partial T_m$ and $\partial \Phi/\partial T_m$. We need only store these nonzero values and keep track of their locations.

4.3 Examples of Sensitivity Coefficients

In this section, we present examples for all the sensitivities or derivatives developed in last section. All the examples are based on a 40×25×10 grid. The channel parameters used are those discussed previously. For the computation of sensitivities of pressure to permeability and porosity fields using the method presented by He et al. [12], we need to simulate the pressure responses for both the actual flowrate and unit flowrate cases. Therefore, the fluid properties and production parameters are also required. A finite difference numerical simulator for single-phase flow simulation [11] is used in this study. Constant flowrate production in one well is considered, and the skin factor is zero. Table 4.3 lists the data used for the cases considered here. In all examples, we first generate a true channel from our stochastic model. For cases where we use pressure data to condition the model, we use synthetic pressure data obtained from our reservoir simulator.

Table 4.3 – Parameters for flow simulation and computation of $\partial p/\partial \mathrm{K}$ and $\partial p/\partial \Phi$

Fluid viscosity	3.0 cp
Total compressibility	10^{-4} 1/psi
Initial pressure of the reservoir	3230.0 psi
Initial time step size	0.01 day
Maximum allowable time step	0.30 day
Production rate	500.0 bbl/day
Production duration	3.0 days
Well radius	0.3 feet
Well location	*iwell*=20, *jwell*=6

Fig. 4.5 shows the permeability distribution of the 5th layer cut from the true reservoir. The black pixel indicates the well location (20,6) in this layer. In this case, we assume that the well fully penetrates all the reservoir gridblocks in the vertical direction and k_c =100md and k_{nc} =1md are used. We can see very clearly the shape of the channel.

Note in Fig. 4.5 that the width of the channel varies with the *x*-coordinate. Notice also that the permeability values along the channel boundaries are changing (appear as different colors) because we use volume-weighted averages between k_c and k_{nc}, which depend on the proportion of the channel within the corresponding gridblocks as discussed previously.

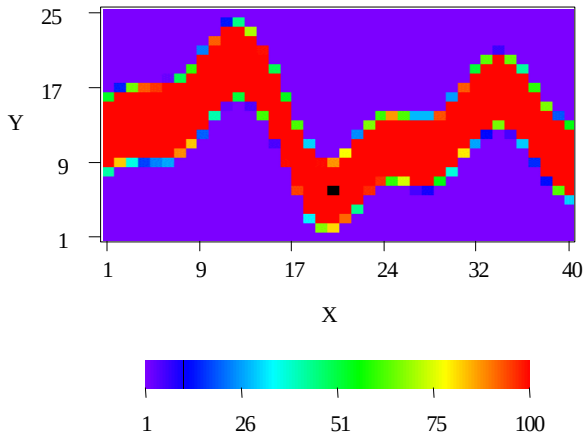

Fig. 4.5 – Permeability distribution of the 5th layer cut from the reservoir grid.

Based on the channel parameters and the calculated permeability and porosity fields, the pressure response for constant production (500 bbl/day) and unit production are simulated. The well is assumed to fully penetrate the reservoir blocks in the vertical direction (layers 1 to 10). The discrete times, t = 0.0, 0.01, 0.03, 0.07, 0.15, 0.31, 0.61, 0.91, 1.21, 1.51, 1.81, 2.11, 2.41, 3.0 (in days), are automatically determined by the initial time step length, the maximum allowable step length and a time step multiplier [11]. Fig. 4.6 shows the simulated pressure field at t=0.91 days.

4.3.1 Example of $\partial p/\partial K$ and $\partial p/\partial \Phi$

The sensitivities of pressure at t_7 = 0.91days with respect to permeability and porosity fields, i.e., $\partial p_7/\partial k_b$ and $\partial p_7/\partial j_b$, b=1,2,……, N_b, are shown in Figs. 4.7 and 4.8.

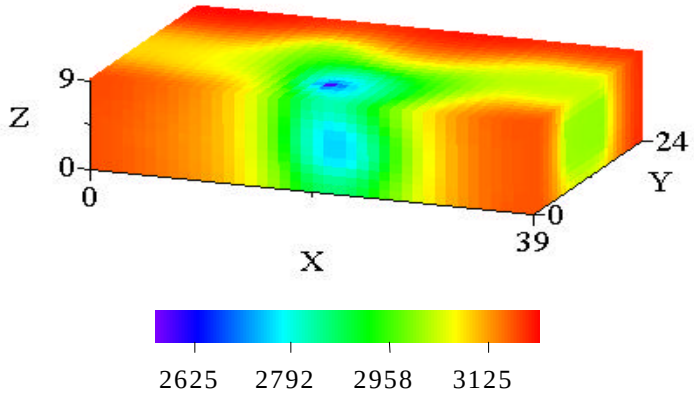

Fig. 4.6 – Pressure distribution at t=0.91 days.

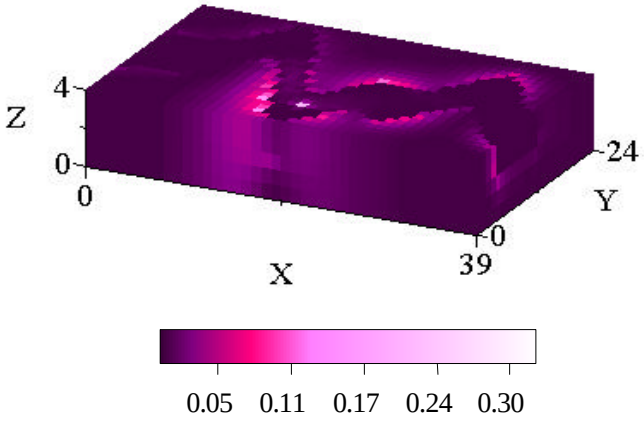

Fig. 4.7 – Sensitivity of pressure to permeability at t=0.91days.

At t_7 = 0.91days, the pressure drop has propagated throughout the entire channel with the biggest pressure drop at the well being about 669psi. We can see from Fig. 4.6 that the pressure within the channel is smaller than that out of the channel due to the higher permeability within the channel.

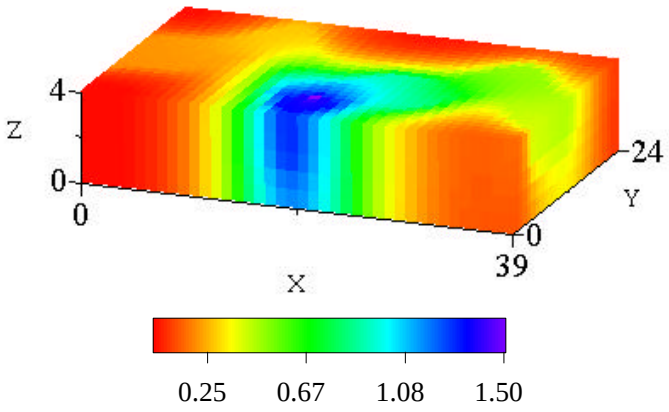

Fig. 4.8 – Sensitivity of pressure to porosity at t=0.91days

Note that Figs. 4.7 and 4.8 illustrate only the sensitivities from layer 0 to layer 4 with the resolution (gridblock dimension) in the vertical direction two times bigger than in other two directions. This is to show clearly the sensitivity changes. We can see from these two figures that the sensitivity values of pressure to porosity are greater (from 0.02 to 1.51) than the sensitivities of pressure to permeability (from 0.0 to 0.51). However, the channel boundaries are much more clearly seen in the sensitivity of pressure to permeability, i.e., in Fig. 4.7. Instead, the channel boundaries are very obscure in the plot of the sensitivity of pressure to the porosity field. We think this may be because the difference in permeability inside and out of the channel (99md) is much bigger than the difference in porosity (0.2). We can also notice that the sensitivity values from x=0 to about x=15 gridblocks within the channel are smaller than those in other portions of the

channel. This is because the well is located such that it takes more time for the flow from left part of the channel (x=0~15) to the well due to the bigger curvature of the channel in the corresponding region. This is also verified by the pressure distribution in Fig. 4.6, which demonstrates higher pressures in the corresponding part of the channel.

Fig. 4.9 shows pressure sensitivity to permeability in layer 5 at three different times, e.g., t_3=0.07, t_7=0.91 and t_{11}=2.11days, respectively. Apparently, the sensitivity of pressure increases with the production time during this period. For example, at the gridblock indexed (16,6) of this layer, the sensitivity values at the three times are 0.09022, 0.21412 and 0.22983 respectively. This is an indication of transient pressure response. After the pressure response has reached pseudo-steady state, the sensitivity coefficient will become constant.

The sensitivity of pressure with respect to porosity, as shown in Fig. 4.10, changes with time too, but the behavior is somewhat different. At very early times, e.g., t_3=0.07 day, the pressure is sensitive only to the porosities in a small area around the well, as seen in Fig. 4.10 (a). As time increases, the pressure is sensitive to the porosities in a bigger area. At some locations close to the well, e.g., the gridblock (19,7) of layer 5, the sensitivities at t_3=0.07, t_7=0.91 and t_{11}=2.11days are, respectively, 1.565, 1.239 and 1.289 which show a decrease and then a increase in sensitivity values. At locations far from the well, the sensitivity increases monotonically from zero. For example, at gridblock (23,6) of layer 5, the sensitivity coefficients at the three times above are 1.047, 1.127 and 1.223, respectively, as shown in Fig. 4.10 (a) through (c).

By comparison, the pressure is more sensitive to the porosity inside the channel, i.e., the bigger porosity value.

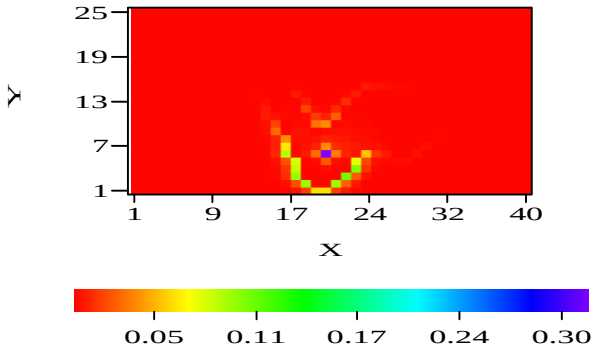

(a) t_3 = 0.07 day.

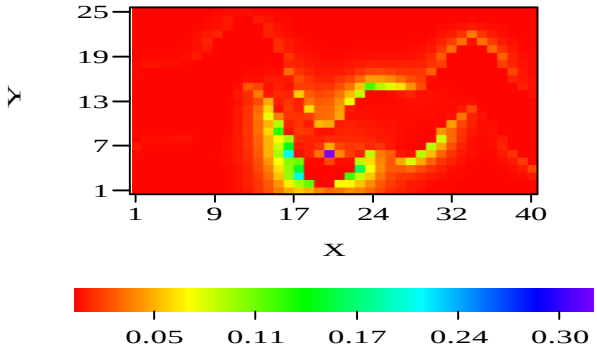

(b) t_7 = 0.91days.

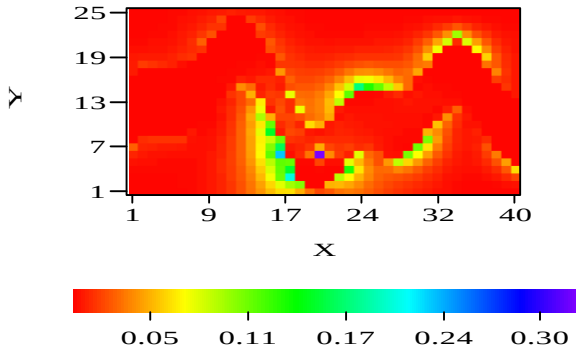

(c) t_{11} = 2.11days.

Fig. 4.9 – Sensitivity of pressure to permeability at different times, (a) t_3 = 0.07 days; (b) t_7 = 0.91days; (c) t_{11} = 2.11days.

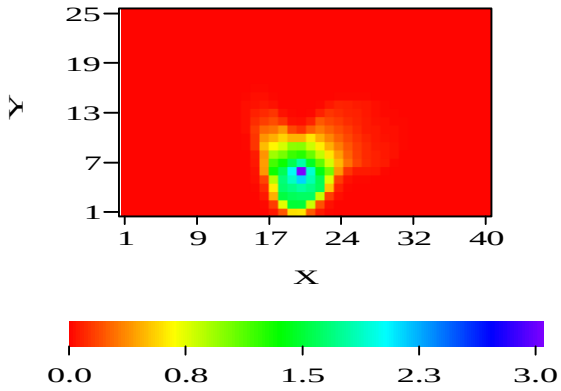

(a) t_3 = 0.07days.

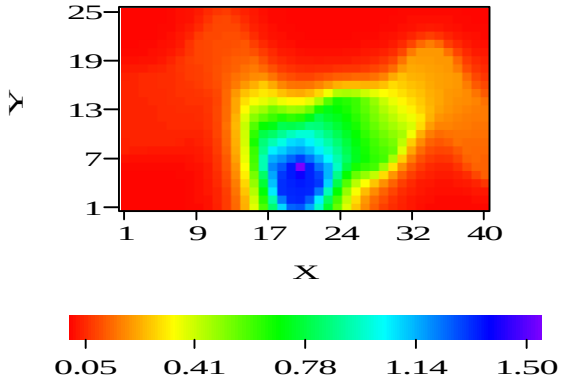

(b) t_7 = 0.91days

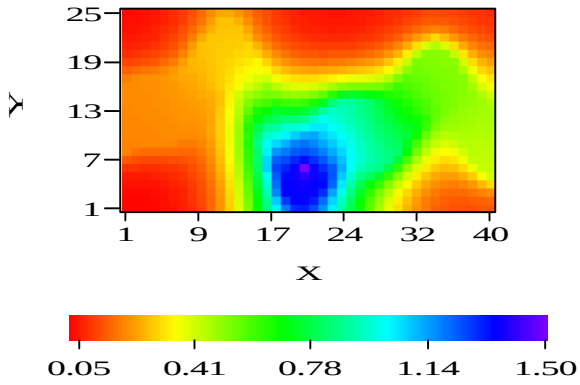

(c) t_{11} = 2.11days.

Fig. 4.10 – Sensitivity of pressure to porosity at different times,
(a) t_3 = 0.07days; (b) t_7 = 0.91days; (c) t_{11} = 2.11days.

4.3.2 $\partial K/\partial T_m$, $\partial K/\partial B_m$, $\partial K/\partial L_m$ and $\partial K/\partial R_m$

$\partial K/\partial T_m$, $\partial K/\partial B_m$, $\partial K/\partial L_m$ and $\partial K/\partial R_m$ are all $N_b \times N_x$ matrices. They represent the change in permeability due to a small perturbation in the channel boundaries, $T_m(x)$, $B_m(x)$, $L_m(x)$ and $R_m(x)$. For example, $\partial k_b/\partial T_{mi}$ for b=1,2,…,N_b and i=1,2,…,N_x, represents the change of permeability at gridblock b due to the change of the top boundary at x_i, where $b = (k\text{-}1)N_xN_y + (j\text{-}1)N_x + i$ according to the ordering of the gridblock system and (i, j, k) are the indices of a block in the x, y and z directions. Recall that we assume a constant permeability inside the channel and another constant permeability outside the channel. Thus, if the gridblock does not contain the top boundary at any particular i, then $\partial k_b/\partial T_{mi}$ is zero. For a particular i, the gridblocks intersected by the top boundary, correspond to those with a z-direction index given by $k = \text{int}(T_{mi}/\Delta z)+1$, and a y-direction index j from $j=\text{int}(L_{mi}/\Delta y)+1$ to $j=\text{int}(R_{mi}/\Delta y)+1$. These are the only blocks where $\partial K/\partial T_m$ is non-zero. Fig. 4.11 shows $\partial k_b/\partial T_{m1}$, i.e., the derivative of gridblock permeability to the channel width at the first gridblock in the x-direction, where $b = (k\text{-}1)N_xN_y + (j\text{-}1)N_x + 1$, $\text{int}(T_{m1}/\Delta z)+1= 8$, $\text{int}(L_{m1}/\Delta y)+1 = 8$ and $\text{int}(R_{m1}/\Delta y)+1 = 15$, i.e., the top boundary of the channel intersects the 8^{th} gridblock in the z-direction and the left and right boundaries of the channel are between 8^{th} and 15^{th} gridblocks in the y-direction, respectively. For any other values of b, $\partial k_b/\partial T_{m1}$ is zero.

Since $\partial K/\partial B_m$, $\partial K/\partial L_m$ and $\partial K/\partial R_m$ have the same characteristics as $\partial K/\partial T_m$, they will not be discussed here. Moreover, $\partial \Phi/\partial T_m$ has the same zero, non-zero structure as $\partial K/\partial T_m$; $\partial \Phi/\partial B_m$, $\partial \Phi/\partial L_m$ and $\partial \Phi/\partial R_m$, respectively, have the same structure as $\partial K/\partial B_m$, $\partial K/\partial L_m$ and $\partial K/\partial R_m$.

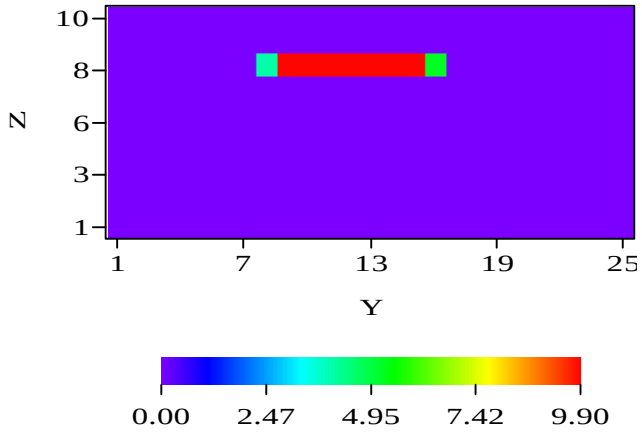

Fig. 4.11 – An example of $\partial k_b / \partial T_{mi}$ for i=1 and $b = (k\text{-}1)N_xN_y+(j\text{-}1)N_x+1$, where j=1~N_y and k=1~N_z.

4.3.3 Examples of $\partial K/\partial m$, $\partial \Phi/\partial m$

These derivatives are measures of how the permeability and porosity fields change with the model parameters. As noted previously, we have a total of $M=4N_x+8$ parameters where the last four parameters represent channel and non-channel permeabilities and porosities. The matrices $\partial K/\partial m$ and $\partial \Phi/\partial m$ are both $N_b \acute{} M$ matrices. They are obtained by using the chain rule, i.e. Eqs. 4.15 and 4.16, where $\partial T_m/\partial m$, $\partial B_m/\partial m$, $\partial L_m/\partial m$ and $\partial R_m/\partial m$ are evaluated from Eqs. 4.21 through 4.40. According to the ordering of parameters in vector m, $m_1 = y_0$, $m_2 = z_0$, $m_3 = s_{xy}$, $m_4 = s_{xz}$, $m_{i+4} = S_{hi}$, $m_{i+Nx+4} = S_{vi}$, $m_{i+2Nx+4} = W_i$, and $m_{i+3Nx+4} = AR_i$ for i=1,2,…,N_x. If the rock properties are also taken as unknowns, then $m_{4Nx+5} = k_c$, $m_{4Nx+6} = k_{nc}$, $m_{4Nx+7} = j_c$, $m_{4Nx+8} = j_{nc}$. Therefore, $\partial K/\partial m_1 = \partial K/\partial y_0$ and $\partial \Phi/\partial m_1 = \partial \Phi/\partial y_0$ represent the derivatives of permeability and porosity in all the gridblocks with respect to the first model parameter, i.e., the y-coordinate of the starting point of the principal direction line. Similarly, $\partial K/\partial m_{1+2Nx+4} = \partial K/\partial W_1$ and $\partial \Phi/\partial m_{1+2Nx+4} = \partial \Phi/\partial W_1$ are the derivatives of permeability and porosity fields with respect to the first

channel width in the x-direction. Fig. 4.12 demonstrates layer 5 cut from $\partial k_b/\partial m_1 = \partial k_b/\partial y_0$ (b=1,2,…,N_b). It shows that $\partial K/\partial y_0$ is zero except at the gridblocks intersected by the left and right channel boundaries, $L_m(x)$ and $R_m(x)$. This makes sense because a small change in y_0 can only cause permeability changes in $L_m(x)$ and $R_m(x)$. Notice that $\partial K/\partial y_0 > 0$ on $R_m(x)$ (top boundary in Fig. 4.12) and $\partial K/\partial y_0 < 0$ on $L_m(x)$ (bottom boundary).

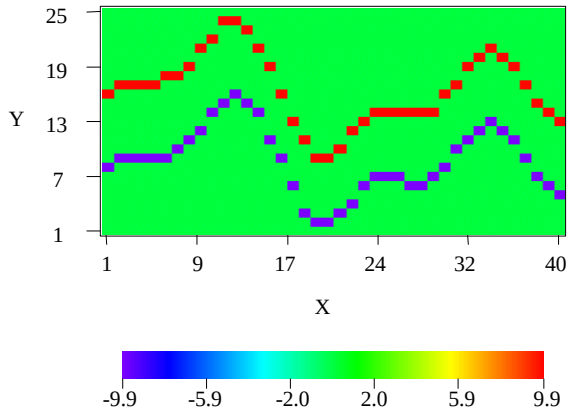

Fig. 4.12 – A layer cut from $\partial K/\partial m_1$ shows nonzero values of $\partial K/\partial m_1$ only in gridblocks intersected by $L_m(x)$ and $R_m(x)$ at this layer.

Similar examples for $\partial K/\partial z_0$, $\partial K/\partial s_{xy}$, $\partial K/\partial s_{xz}$, $\partial K/\partial S_{h1}$, $\partial K/\partial S_{v1}$, $\partial K/\partial W_1$ and $\partial K/\partial AR_1$ are shown in Figs 4.13 through 4.19. All these plots illustrate results for one layer or cross-section cut from the entire matrix.

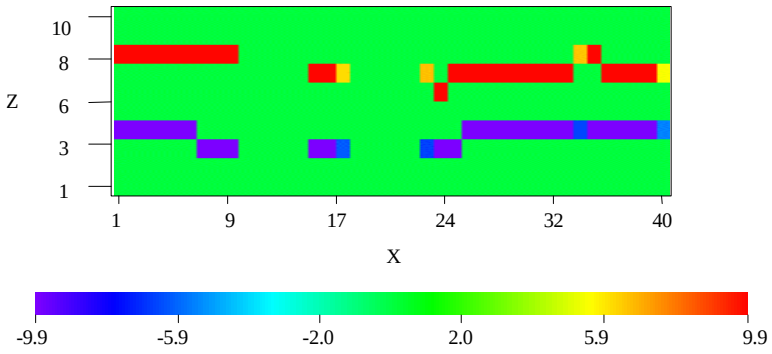

Fig. 4.13 – A x-z cross-section (13) cut from $\partial K/\partial z_0$, the nonzero values are in the gridblocks intersected by $T_m(x)$ and $B_m(x)$. At some x's, $T_m(x)$ and $B_m(x)$ do not intersect this cross-section.

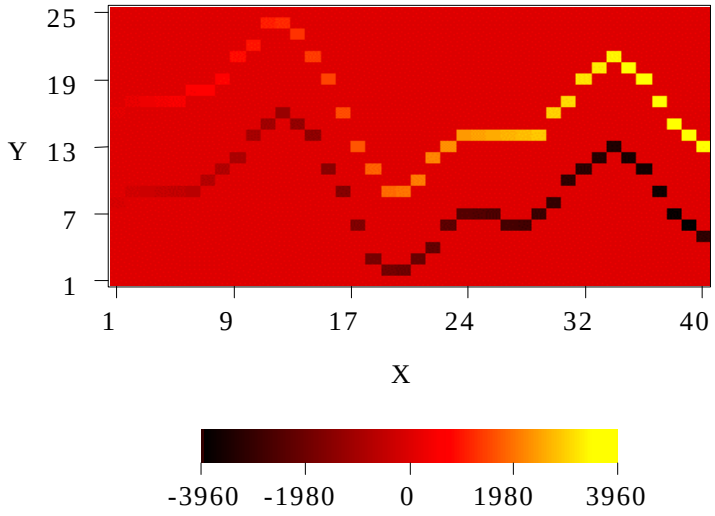

Fig. 4.14 – A layer (5) cut from $\partial K/\partial s_{xy}$, the nonzero values appear in the gridblocks intersected by $L_m(x)$ and $R_m(x)$, the values of $\partial K/\partial s_{xy}$ are very large as it is related to the x-coordinate of $L_m(x)$ and $R_m(x)$.

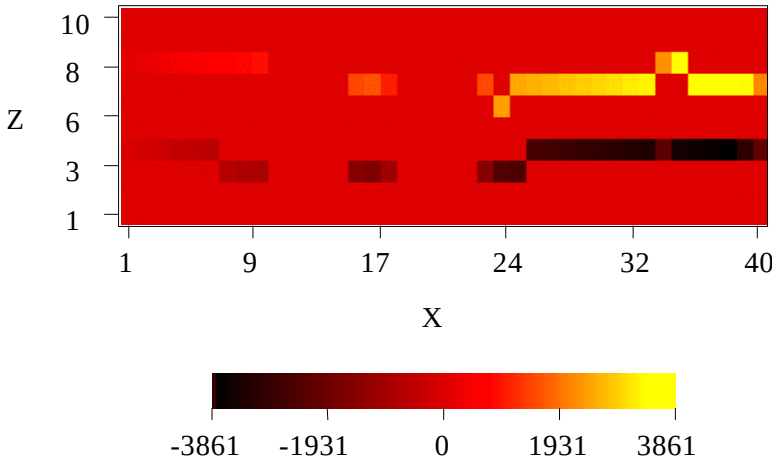

Fig. 4.15 – A x-z cross-section cut from $\partial K/\partial s_{xz}$, the nonzero values are in the gridblocks intersected by $T_m(x)$ and $B_m(x)$, but the values of $\partial K/\partial s_{xz}$ on the top boundary gridblocks are opposite to the values on the bottom boundary gridblocks.

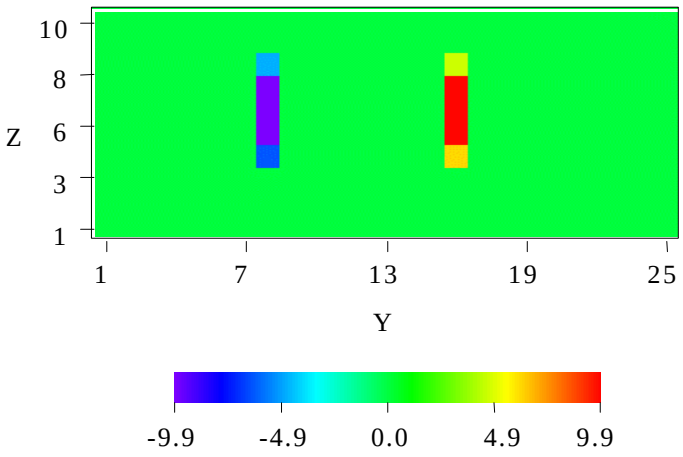

Fig. 4.16 – A *y*-*z* cross-section cut from $\partial K/\partial S_{h1}$, the gridblocks intersected by L_{m1} and R_{m1} have non-zero values of $\partial K/\partial S_{h1}$.

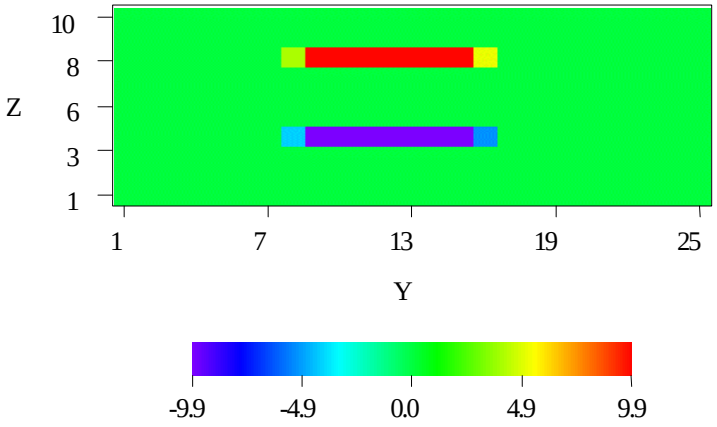

Fig. 4.17 – A *y*-*z* cross-section cut from $\partial K/\partial S_{v1}$, the nonzero values are in the gridblocks intersected by T_{m1} and B_{m1}.

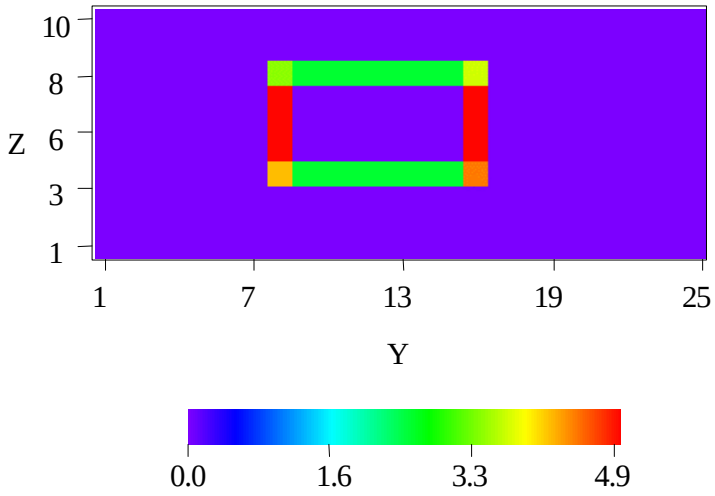

Fig. 4.18 – A *y*-*z* cross-section cut from $\partial K/\partial W_1$, the nonzero values are in the gridblocks intersected by T_{m1}, B_{m1}, L_{m1} and R_{m1}, meaning that changing W_1 will change the permeability on all the boundary blocks since the width and thickness of the channel are related.

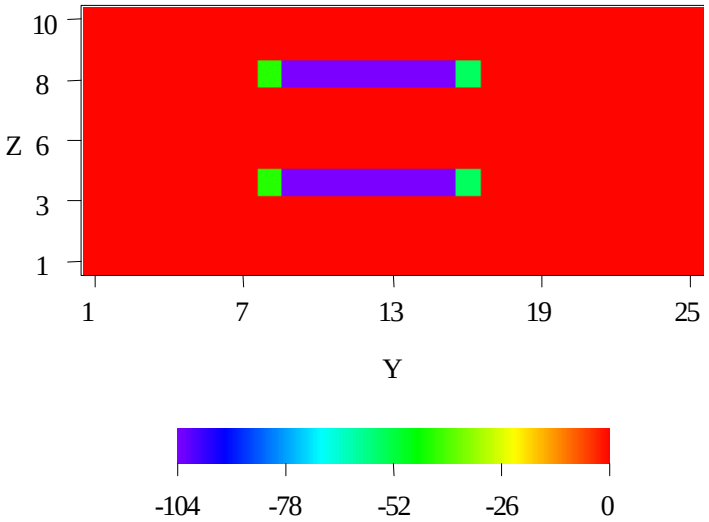

Fig. 4.19 – A *y*-*z* cross-section cut from $\partial K/\partial AR_1$, the nonzero values are in the gridblocks intersected by T_{m1}, B_{m1}, meaning that increasing AR_1 will decrease the gridblock permeabilities intersected by T_{m1}, B_{m1}.

The derivatives of porosity with respect to model parameters, i.e. $\partial\Phi/\partial m$, are analogous to $\partial K/\partial m$ shown above except the actual values are of course different.

4.3.4 The Sensitivity of Pressure to Model Parameters, $\partial p/\partial m$

The sensitivity matrix, $G = \partial p/\partial m$, is required for channel inversion. Suppose we have N_p observed pressure data, then $\partial p/\partial m$ is a $N_p \times M$ matrix. In the example considered below, there are 11 conditioning pressure data and N_x=40. Since k_c, k_{nc}, j_c and j_{nc} are specified constants, so $M=4N_x+4=164$ and the dimension of $\partial p/\partial m$ is 11×164.

Fig. 4.20 shows the sensitivity of pressure to the first two channel parameters, i.e., y_0 and z_0. Note that the abscissa of Fig. 4.20 is the test time t.

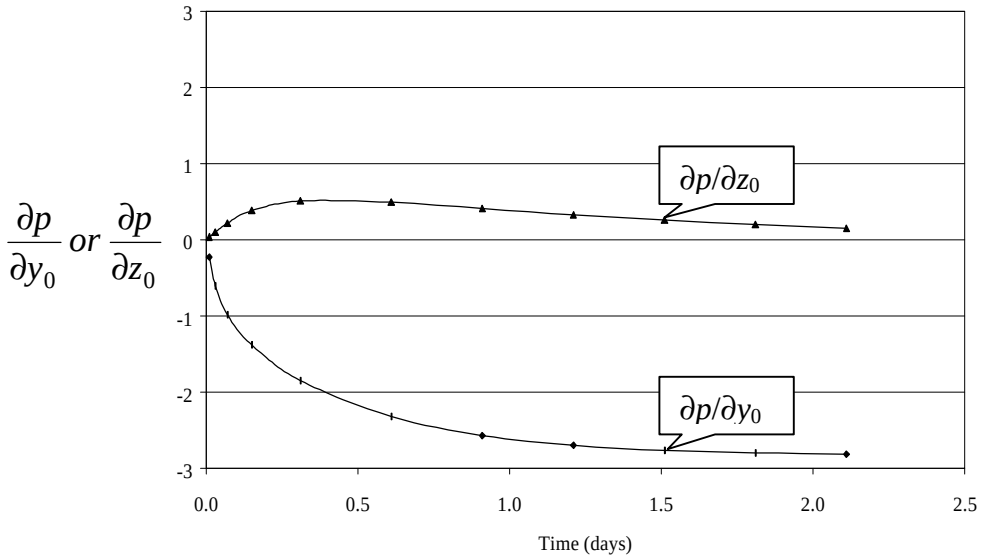

Fig. 4.20 – Sensitivity of pressure to y_0 and z_0 at different times.

It is clear in this case that $\partial p/\partial y_0$ and $\partial p/\partial z_0$ are changing with time but $\partial p/\partial y_0$ is always negative and $\partial p/\partial z_0$ is positive. This means that the pressure decreases as y_0 increases but increases as z_0 increases. In order to understand this physically, we first consider the relationship between parameter y_0 and the bottom-hole pressure. We saw in Fig. 4.12 that

increasing y_0 will cause an increase of permeability in gridblocks intersected by $L_m(x)$ and a decrease of permeability in the gridblocks intersected by $R_m(x)$. In the current case, the well is closer to the boundary $R_m(x)$. Hence the reduction of permeability in gridblocks intersected by $R_m(x)$ will affect the flowing pressure more. Permeability decrease will lead to a higher pressure drop or lower flowing pressure. So increasing y_0 causes lower flowing pressure eventually, i.e., $\partial p/\partial y_0<0$. It is possible that $\partial p/\partial y_0$ could be positive depending on the relative position of the well in the channel and the test time. Similarly, $\partial p/\partial s_{xy}$ should also be negative in this case as shown in Fig. 4.21.

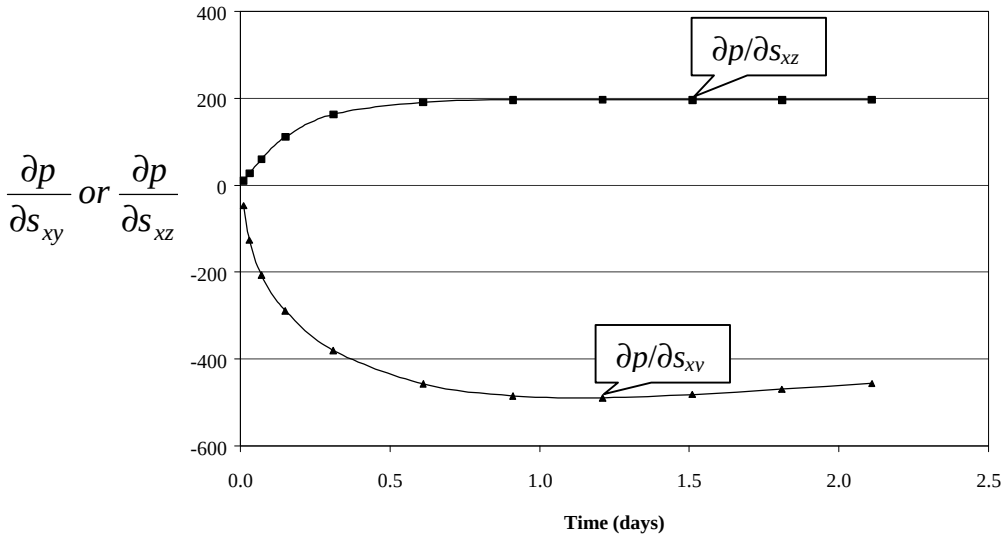

Fig. 4.21 – Sensitivity of pressure to s_{xy} and s_{xz} at different times.

As far as $\partial p/\partial z_0$ is concerned, we see from Fig. 4.13 that $\partial K/\partial z_0$ is positive on the boundary gridblock intersected by $T_m(x)$ and negative on the boundary gridblock intersected by $B_m(x)$. This means that increasing z_0 will lead to an increase in permeability for gridblocks intersected by $T_m(x)$ but a reduction of permeability in gridblocks intersected by $B_m(x)$. Based on Eqs. 4.5 through 4.11, the increase in permeability of the gridblocks intersected by $T_m(x)$ for a uniform grid system will mainly depend on the total

proportion of the channel within the boundary gridblocks, i.e., the sum of $P_t(x)$. Similarly the reduction of permeability in gridblocks intersected by $B_m(x)$ will mainly depend on the sum of $P_b(x)$. In the above case, $\sum_{i=1}^{N_x} P_{ti} = 208.13\,ft$, and $\sum_{i=1}^{N_x} P_{bi} = 202.55\,ft$. So, increasing z_0 would result in a bigger increment of the gridblock permeabilities intersected by $T_m(x)$. In other words, the overall permeability of the system would increase a little bit, which means that a lower pressure drop or higher flowing pressure would be required to keep a constant flow rate. Thus, $\partial p/\partial z_0$ is positive, as shown in Fig. 4.20. By the same reasoning, we find that we should expect $\partial p/\partial s_{xz}$ to be positive, as shown in Fig. 4.21.

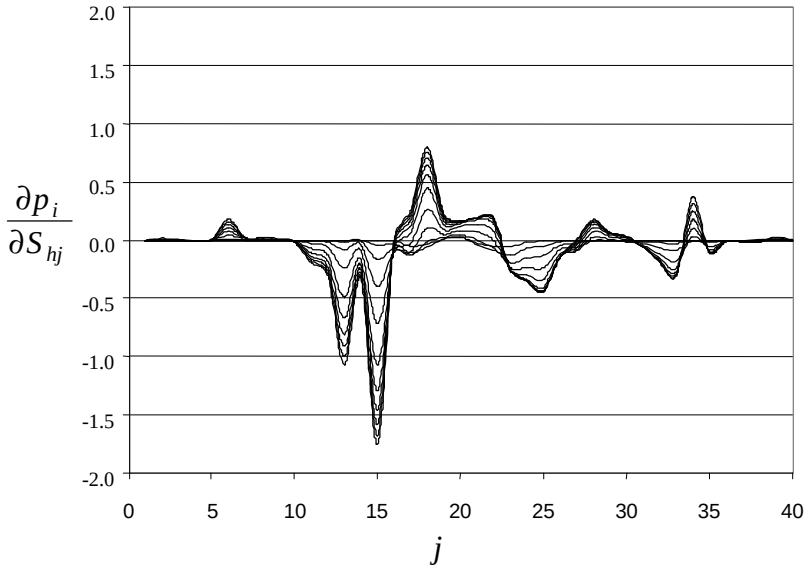

Fig. 4.22 – Sensitivity of pressure to horizontal sinuosity of the channel, there are 11 curves corresponding to 11 different times, where the bigger values in different curves correspond to later times.

Figs. 4.22 and 4.23, respectively, present plots of $\partial p/\partial S_h$ and $\partial p/\partial S_v$. On each figure, each curve corresponds to one time value. Note that $\partial p/\partial S_h$ and $\partial p/\partial S_v$ change with time and with locations. Physically, the results indicate that at a fixed time, the pressure decreases as S_{hi} increases for some i, but increases for other i values. Fig. 4.23 shows

similar results. The physical explanation for this phenomenon is not obvious. Thus, we consider $\partial p/\partial S_h$ as an example and do a qualitative analysis.

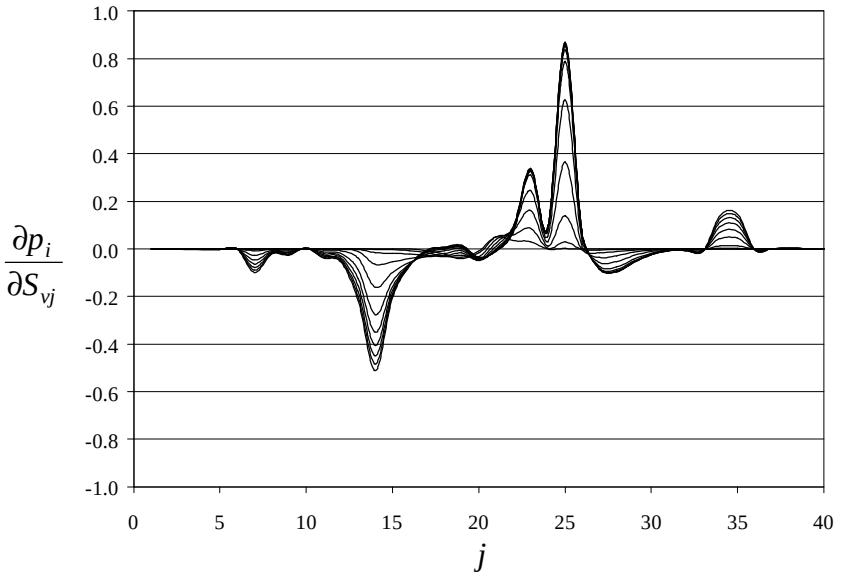

Fig. 4.23- Sensitivity of pressure to vertical sinuosity of the channel.

For simplicity, we will consider the sensitivity of j^{th} observed pressure, i.e., p_j, to i^{th} horizontal sinuosity S_{hi}. According to Eqs. 4.12 through 4.16, we have

$$\frac{\partial p_j}{\partial S_{hi}} = \sum_{b=1}^{N_b}\left(\frac{\partial p_j}{\partial \mathrm{k}_b}\frac{\partial \mathrm{k}_b}{\partial S_{hi}} + \frac{\partial p_j}{\partial j_b}\frac{\partial j_b}{\partial S_{hi}}\right) = \left(\frac{\partial p_j}{\partial S_{hi}}\right)_1 + \left(\frac{\partial p_j}{\partial S_{hi}}\right)_2 . \tag{4.59}$$

Although the two terms in Eq. 4.59 might be very different in altitude, they have the same sign. Therefore, we only consider the first term for simplicity.

$$\left(\frac{\partial p_j}{\partial S_{hi}}\right)_1 = \sum_{b=1}^{N_b}\left(\frac{\partial p_j}{\partial \mathrm{k}_b}\frac{\partial \mathrm{k}_b}{\partial S_{hi}}\right). \tag{4.60}$$

Substituting the expression for $\partial \mathrm{k}_b/\partial S_{hi}$ given by Eq. 4.15 into Eq. 4.60 gives

$$\begin{aligned}\left(\frac{\partial p_j}{\partial S_{hi}}\right)_1 &= \sum_{b=1}^{N_b}\left(\frac{\partial p_j}{\partial \mathrm{k}_b}\frac{\partial \mathrm{k}_b}{\partial S_{hi}}\right) \\ &= \sum_{b=1}^{N_b}\left(\frac{\partial p_j}{\partial \mathrm{k}_b}\left(\sum_{\ell=1}^{N_x}\frac{\partial \mathrm{k}_b}{\partial T_{m\ell}}\frac{\partial T_{m\ell}}{\partial S_{hi}} + \frac{\partial \mathrm{k}_b}{\partial B_{m\ell}}\frac{\partial B_{m\ell}}{\partial S_{hi}} + \frac{\partial \mathrm{k}_b}{\partial L_{m\ell}}\frac{\partial L_{m\ell}}{\partial S_{hi}} + \frac{\partial \mathrm{k}_b}{\partial R_{m\ell}}\frac{\partial R_{m\ell}}{\partial S_{hi}}\right)\right).\end{aligned} \tag{4.61}$$

According to Eqs. 4.22, 4.27, 4.32 and 4.37,

$$\frac{\partial T_{m\ell}}{\partial S_{hi}} = \frac{\partial B_{m\ell}}{\partial S_{hi}} = 0 . \tag{4.62}$$

So Eq. 4.61 becomes

$$\left(\frac{\partial p_j}{\partial S_{hi}}\right)_1 = \sum_{b=1}^{N_b} \frac{\partial p_j}{\partial \mathrm{k}_b} \left(\sum_{\ell=1}^{N_x} \frac{\partial \mathrm{k}_b}{\partial L_{m\ell}} \frac{\partial L_{m\ell}}{\partial S_{hi}} + \frac{\partial \mathrm{k}_b}{\partial R_{m\ell}} \frac{\partial R_{m\ell}}{\partial S_{hi}} \right). \tag{4.63}$$

Based on Eqs. 4.32 and 4.37, $\frac{\partial L_{m\ell}}{\partial S_{hi}} = \frac{\partial R_{m\ell}}{\partial S_{hi}} = 0$, if $i \neq \ell$. So Eq. 4.63 can be rewritten as

$$\left(\frac{\partial P_j}{\partial S_{hi}}\right)_1 = \sum_{b=1}^{N_b} \frac{\partial P_j}{\partial K_b} \left(\frac{\partial \mathrm{k}_b}{\partial L_{mi}} + \frac{\partial \mathrm{k}_b}{\partial R_{mi}} \right). \tag{4.64}$$

Actually, only a few terms in Eq. 4.64 are nonzero. These terms correspond to $b\text{¢} = (k\text{-}1)N_xN_y + (j_1\text{-}1)N_x + i$ and $b = (k\text{-}1)N_xN_y + (j_2\text{-}1)N_x + i$ (see Fig. 4.4). Note that $b\text{¢}$ and b here represent, respectively, the gridblocks for k from k_1 to k_2 (i, j_1 and j_2 are fixed). According to Eqs. 4.47 and 4.48, we can write all the possible non-zero terms as follows,

$$\begin{aligned} \left(\frac{\partial p_j}{\partial S_{hi}}\right)_1 = & \sum_{k_1}^{k_2} \frac{\partial p_j}{\partial \mathrm{k}_{b'}} \left(\frac{\mathrm{k_{nc}} - \mathrm{k_c}}{\Delta y} + \frac{P_{bi}(\mathrm{k_{nc}} - \mathrm{k_c})}{\Delta z \Delta y} + \frac{P_{ti}(\mathrm{k_{nc}} - \mathrm{k_c})}{\Delta z \Delta y} \right) \\ & + \sum_{k_1}^{k_2} \frac{\partial p_j}{\partial \mathrm{k}_{b''}} \left(\frac{\mathrm{k_c} - \mathrm{k_{nc}}}{\Delta y} + \frac{P_{bi}(\mathrm{k_c} - \mathrm{k_{nc}})}{\Delta z \Delta y} + \frac{P_{ti}(\mathrm{k_c} - \mathrm{k_{nc}})}{\Delta z \Delta y} \right). \end{aligned} \tag{4.67}$$

Rearranging Eq. 4.67 gives

$$\left(\frac{\partial p_j}{\partial S_{hi}}\right)_1 = \sum_{k_1}^{k_2} \left(\frac{\partial p_j}{\partial \mathrm{k}_{b''}} - \frac{\partial p_j}{\partial \mathrm{k}_{b'}} \right) \left(\frac{\mathrm{k_c} - \mathrm{k_{nc}}}{\Delta y} + \frac{P_{bi}(\mathrm{k_c} - \mathrm{k_{nc}})}{\Delta z \Delta y} + \frac{P_{ti}(\mathrm{k_c} - \mathrm{k_{nc}})}{\Delta z \Delta y} \right). \tag{4.68}$$

Since $\mathrm{k_c} > \mathrm{k_{nc}}$, i.e., the permeability inside the channel is greater than that out of the channel, $\left(\frac{\partial p_j}{\partial S_{hi}}\right)_1$ will be non-negative if $\frac{\partial p_j}{\partial \mathrm{k}_{b''}} \geq \frac{\partial p_j}{\partial \mathrm{k}_{b'}}$ for each k, $k_1 \leq k \leq k_2$ (see Fig. 4.3

or Fig. 4.4), otherwise $\left(\frac{\partial p_j}{\partial S_{hi}}\right)_1$ will be negative. Recall $\frac{\partial p_j}{\partial k_{b''}}$ and $\frac{\partial p_j}{\partial k_{b'}}$ are the sensitivities of j^{th} observed pressure to the permeability in gridblock $b¢$ intersected by boundary $L_m(x)$ and in gridblock b intersected by boundary $R_m(x)$, respectively. From Fig. 4.7, we saw that the sensitivity is sometimes greater on the left, and sometimes greater on the right, hence the variability in sign in Fig. 4.22.

Fig. 4.24 illustrates the sensitivity of pressure at different times to the widths of the channel. It is understandable that $\frac{\partial p_i}{\partial W_j} > 0$ because increasing channel widths will result in increasing channel volume or the overall permeability of the system correspondingly, which will further lead to lower pressure drop or higher flowing pressure. This indicates that $(\partial p_i / \partial W_j)>0$. Moreover, at early times, the pressure is only sensitive to channel widths at x_i locations close to the well (at well location, x_i =20).

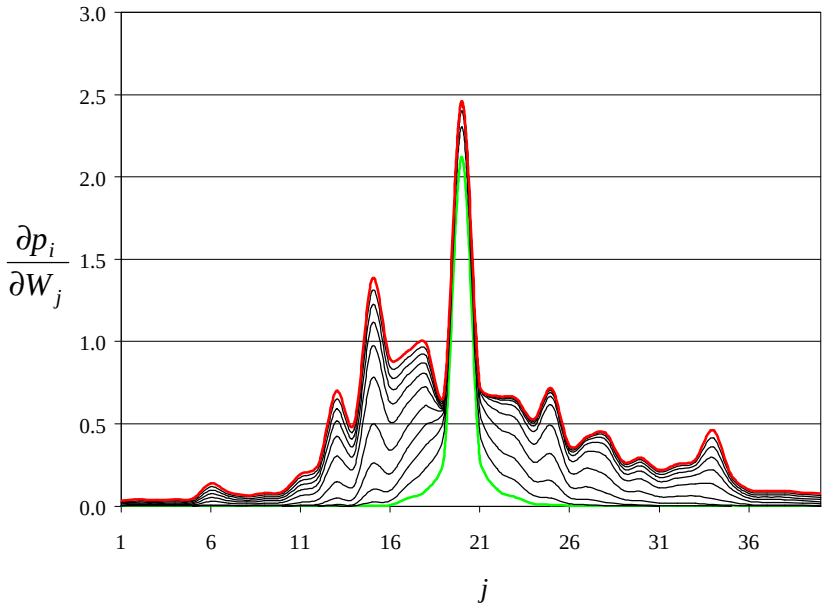

Fig. 4.24- Sensitivity of pressure to the widths of the channel at different times.

Fig. 4.25 shows the sensitivity of pressure to the aspect ratio, i.e., $\frac{\partial p}{\partial AR}$. Different curves correspond to different pressures, i.e., pressures at different times. The results of Fig. 4.25 demonstrate that $\frac{\partial p}{\partial AR}$ is negative, and that increasing $AR(x)$ will reduce the well flowing pressure.

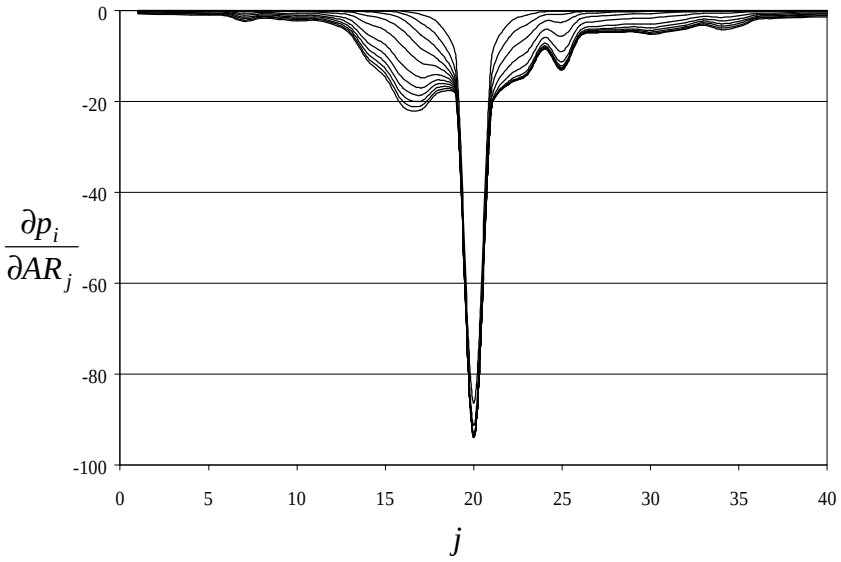

Fig. 4.25 – Sensitivity of pressure to aspect ratios of the channel.

To understand this, recall that $AR(x)$ is the ratio of the width to the thickness of the channel, i.e., $AR(x) = W(x)/H(x)$, where $H(x)$ denotes the channel thickness. Consider that the pressure is only a function of $W(x)$ and $AR(x)$, i.e., $p = p[W(x),AR(x)]$. Since AR is a function of W and H, we can further write

$$p = p[W, AR(W, H)]. \tag{3.69}$$

Applying chain rule for the derivative of p with respect to channel thickness H, gives

$$\frac{\partial p}{\partial H} = \frac{\partial p}{\partial AR}\frac{\partial AR}{\partial H} = \left[-\frac{W}{H^2}\right]\frac{\partial p}{\partial AR}. \tag{3.70}$$

Clearly, $\frac{\partial p}{\partial AR}$ should be negative since $\frac{\partial p}{\partial H}>0$.

CHAPTER V

SYNTHETIC CASE STUDIES

A few synthetic case studies are given in this chapter. The purpose is to demonstrate the effectiveness and efficiency of the channel inversion process described in the previous chapters.

Although real case studies would be done with similar procedures, all the examples in this chapter are synthetic. In fact, the observed pressure data are generated from a known "true model" which is a realization of the prior model. The observed thickness will be obtained from the well in which the "observed pressure data" were simulated and taken as pressure measurements after some random noise was added.

A detailed procedure used for generating pressure "measurements" for all the cases considered here is described below.

(1) Data input

The input data for generating a true channel and pressure response include specification of the statistical parameters (mean, variance, covariance for the stochastic model parameters), dimension of the simulation grid and other parameters for flow simulation such as initial pressure, fluid viscosity, flowrate and duration, well location and well radius. One also needs to specify the variance for data measurement errors of the conditioning data.

(2) Generation of a 3D single channel on the simulation grid

This is done by sampling the Gaussian distributions and Gaussian fields for the specified model parameters. Univariate Gaussian distributions, (e.g., those for the four random variables of the principal direction line and for the rock properties if specified as unknowns) can be sampled using standard pseudo random number generators with the proper variance. The moving average method is used for sampling the 1D Gaussian random fields (horizontal and vertical sinuosity, width and aspect ratio) as described in Chapter II.

(3) Distribution of permeability and porosity

Two cases will be considered in this study. One uses uniform, fixed permeability and porosity inside the channel and out of the channel. The other uses uniform but uncertain porosity and permeability both inside and outside the channel. In both cases, the volume average method is used for calculating the permeability and porosity of the boundary gridblocks as discussed before. In the first case, permeability and porosity are not model parameters, whereas in the second case, channel permeability (k_c), non-channel permeability (k_{nc}), channel porosity (j_c) and non-channel porosity (j_{nc}) will be model parameters.

(4) Simulation for pressure response as “observed pressure data”

This is done by the numerical flow simulator. The time intervals for simulation is calculated automatically, see [11] for details. Random noise based on a specified data measurement error variance is added to the simulated pressure to obtain the synthetic data.

(5) Channel thickness and top boundary of the channel at a well location

This is obtained by the width and aspect ratio at the well locations of the "true reservoir". For example, if the well is located at the 20th gridblock in the *x*-direction and the well is in the channel and fully penetrates the channel, then the true thickness is *W*(20)/*AR*(20). The top boundary is calculated from Eq. 4.17 at the well location. The observed data are generated by adding random noise to these data.

5.1 Case 1: Constant Permeability and Porosity Inside and Outside the Channel

The model parameters are listed in Table 5.1a and parameters for flow simulation are listed in Table 5.1b.

Table 5.1a – Geometric parameters of the channel model for case 1

Principal direction line: $\bar{y}_0 = 100.0\text{ft},\ \bar{z}_0 = 50.0\text{ft},\ \bar{s}_{xy} = 0.05,\ \bar{s}_{xz} = 0.00$,

$$s^2_{y_0} = 1.0,\ s^2_{z_0} = 1.0,\ s^2_{s_{xy}} = 0.001,\ s^2_{s_{xz}} = 0.001.$$

Horizontal and vertical sinuosity of the centerline: $s^2_{S_h} = 676.0,\ s^2_{S_v} = 9.0$,

$$a_{S_h} = a_{S_v} = 80.0\text{ft}.$$

Width and aspect ratio: $m_W = 80.0\text{ft},\ s^2_W = 9.0,\ a_W = 80.0\text{ft},$

$$m_{AR} = 2.0,\ s^2_{AR} = 0.025,\ a_W = 80.0\text{ft}.$$

Table 5.1b – Parameters for flow simulation

Fluid viscosity	3.0 cp
Total compressibility	10^{-5} 1/psi
Initial pressure of the reservoir	3230.0 psi
Initial time step size	0.01 day
Maximum allowable time step	0.30 day
Production rate	500.0 bbl/day
Production duration	3.0 days
Well radius	0.3 feet

A seed value of –3244 is used to generate a realization to use as the "true model". The dimension of the simulation grid is 40×25×10 and the well is located at (20,11). The total channel volume from this true model is 1.315×10^6 ft^3 and the channel thickness and the top depth at the well location are 41.6ft and 72.7ft, respectively. The observed pressure data are obtained by adding random noise (pressure data error variance is 1) to the simulated pressure data. Similarly, the observed channel thickness and top depth are obtained by adding random noise to the corresponding true values. The measurement error variance specified for channel thickness and top depth is 0.5.

In this case, uniform permeability and porosity both inside and outside the channel are specified and fixed as k_c=100md, k_{nc}=1md, ϕ_c=0.3 and ϕ_{nc}=0.1. Therefore, the model parameter vector contains only geometric parameters that describe the channel.

To obtain a realization, we apply the randomized maximum likelihood method. This requires that we generate an unconditional realization of the model from the prior and an unconditional realization of the data and minimize the objective function given by Eq. 3.17. The unconditional realization of the data is obtained again by adding random noise to the observed data based on the related variances.

A different seed (-32442) for the random number generator was used for generating unconditional realizations of the prior and the conditioning data. When minimizing the objective function by the Levenberg-Marquardt algorithm, we simply take the unconditional realization of the prior as an initial guess of the model parameter vector.

Table 5.2 presents the pressure data, including the simulated pressure data from the flow simulator, the observed pressure data (simulated plus random noise) and the unconditional realization of the pressure data used as d_{uc} (observed plus random noise).

The observed channel thickness and top depth are obtained in a similar way and are 41.4ft and 72.8ft, respectively. Their unconditional realizations are 41.1ft and 73.2ft, respectively.

Table 5.2 – Pressure data for case 1

Time (days)	Simulated (psi)	Observed (psi)	Unconditional (psi)
.01	2999.46	2999.28	3000.37
.03	2948.13	2947.97	2946.83
.07	2898.26	2898.18	2898.32
.15	2838.34	2837.28	2837.75
.31	2760.83	2760.95	2761.17
.61	2657.47	2657.90	2658.19
.91	2570.51	2571.37	2570.93
1.21	2491.44	2490.77	2489.69
1.51	2416.75	2418.08	2417.18
1.81	2344.70	2345.04	2344.61
2.11	2274.33	2274.38	2274.00

Fig. 5.1 shows the objective function versus the number of iterations of the Levenberg-Marquardt algorithm. As we can see, the objective function decreases rapidly from a very large value (10360) at the first iteration to the very small value of 9 in 4 iterations. This demonstrates the efficiency of the Levenberg-Marquadt algorithm for this case.

The pressure data matching as well as the observed thickness and top depth matching also verify this point. Fig. 5.2 shows the pressure data match, in which the triangles represent the observed pressure data and the solid line is drawn from the calculated pressure based on the conditional realization of the channel. The calculated channel thickness and top depth at the well location are 41.5ft (observed 41.1ft) and 72.8ft (observed 72.8ft), respectively.

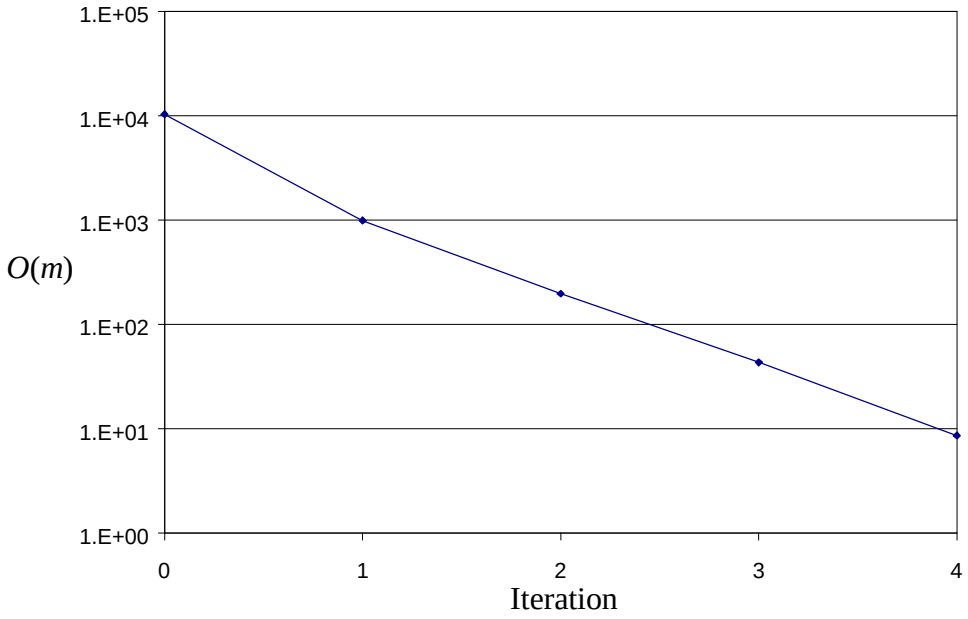

Fig. 5.1 - Objective function $O(m)$ versus iteration.

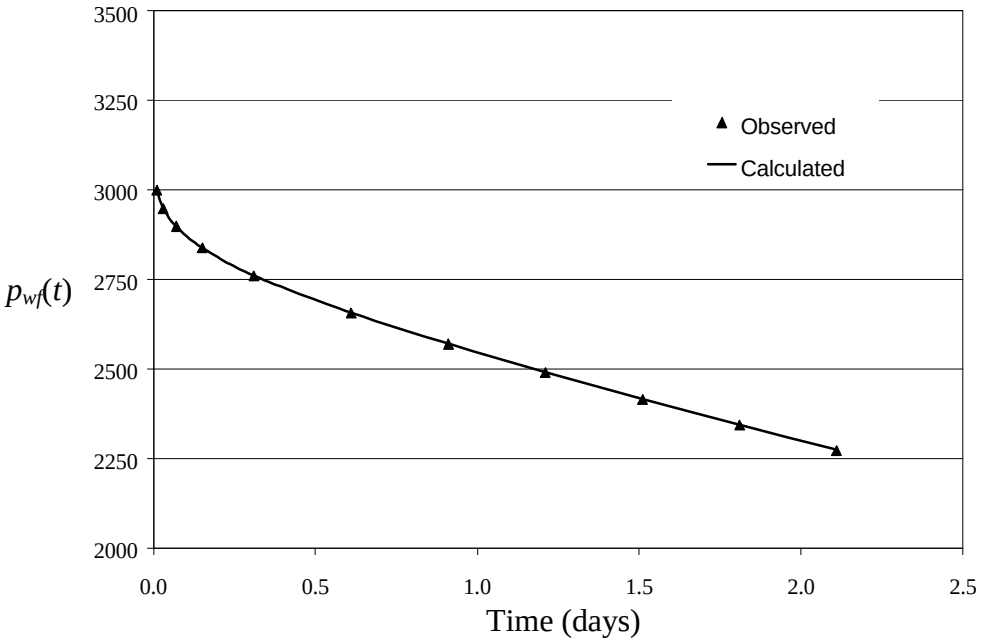

Fig. 5.2 – Pressure data matching for case 1.

Although, the data mismatch is satisfactory, we also need to ensure that the resulting channel is “plausible”. Fig. 5.3 shows the true channel, the initial guess (unconditional realization from the prior) and the final result obtained by matching the observed pressure data and the observed channel thickness and top depth at the well. Only the channel is shown in each figure since it is easy to visualize. As discussed before, each channel in Fig. 5.3 is actually represented by the permeability distribution within the channel and on the channel boundaries. Different colors on the channel boundaries represent different permeability values calculated by the volumetric average.

That the final channel from inversion in Fig.5.3 (c) is quite different from the true model in Fig. 5.3 (a) indicates that the well test pressure data are not very sensitive to the overall shape of the channel, and that the true channel can not be determined uniquely by the pressure response at a single well. This is more clearly demonstrated by the conditional realizations of the four Gaussian random fields that control the shape of the channel, i.e., the horizontal and vertical sinuosity ($S_h(x)$, $S_v(x)$), the width of the channel ($W(x)$) and the aspect ratio ($AR(x)$) of the channel, as shown in Figs. 5.4 through 5.7.

In each figure of Figs. 5.4 through 5.7, there are three lines. The ones with triangles represent the true random fields, the ones with squares are the initial guesses (unconditional realizations) of the random fields and the lines with diamonds are the corresponding fields from inversion or conditional realizations of the Gaussian random fields. The labels on the x-axis of each figure are x-direction indices and the conditional realization of each Gaussian random field is titled as final field.

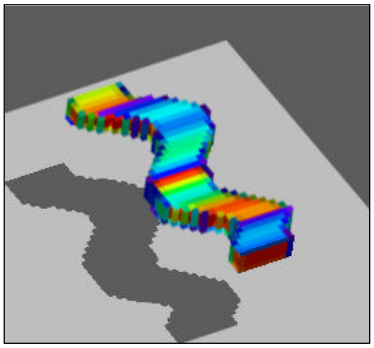

(a) True channel.

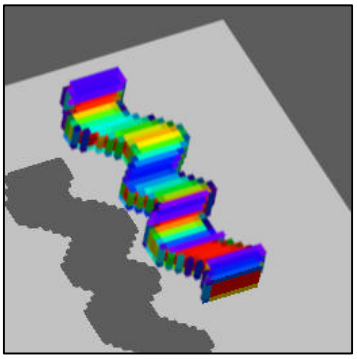

(b) Initial guess of the model.

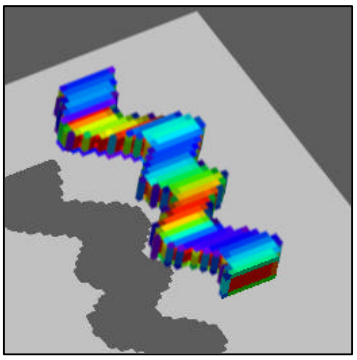

(c) Conditional realization of the channel.

Fig. 5.3 – Comparison of the channel images, (a) true channel image; (b) initial guess of the channel; (c) conditional realization of the channel.

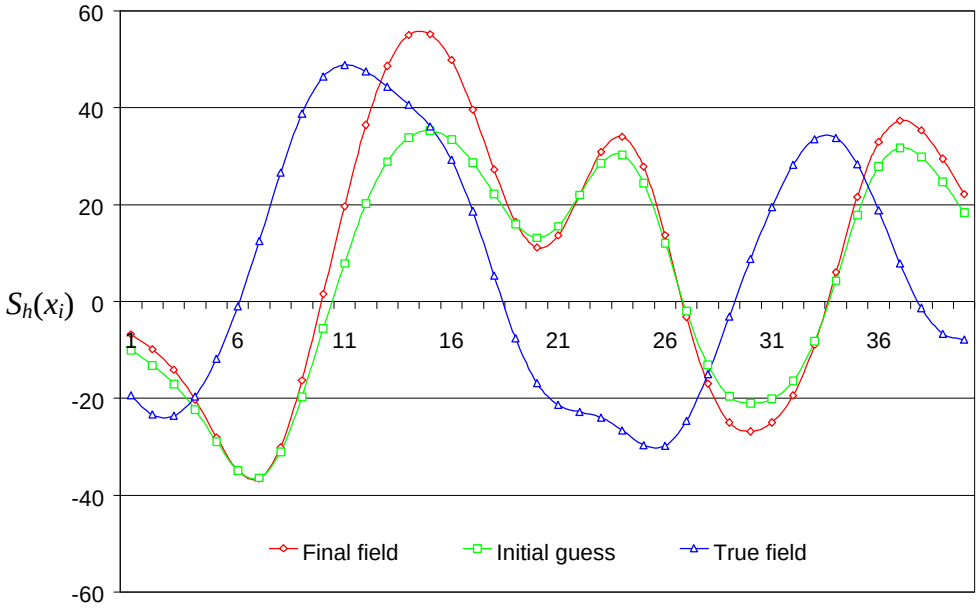

Fig. 5.4 – Horizontal sinuosity of the channel.

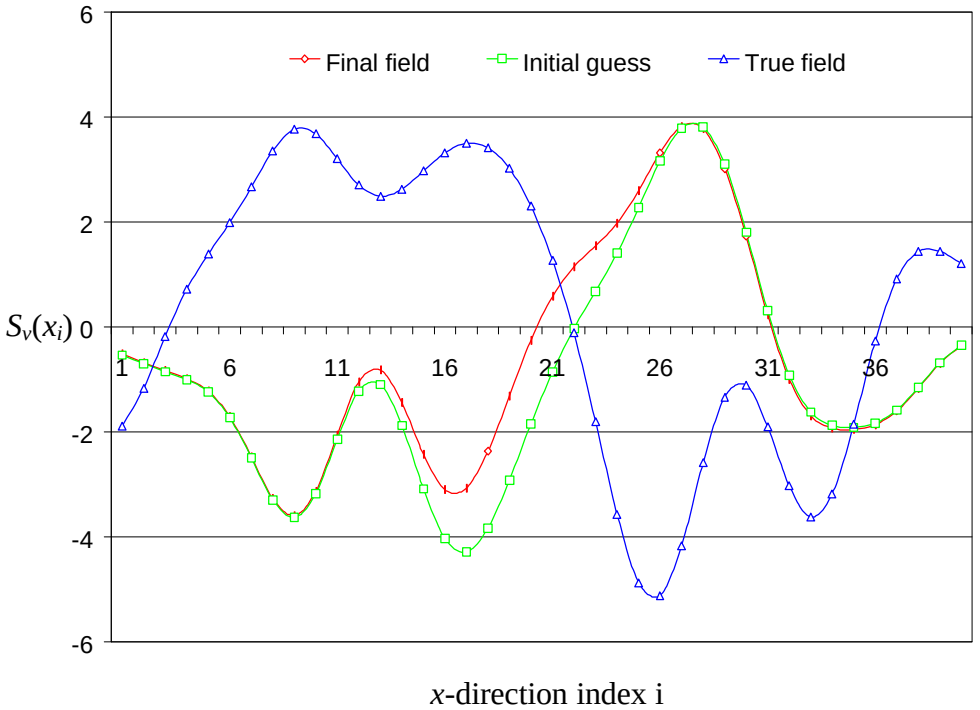

Fig. 5.5 – Vertical sinuosity of the channel.

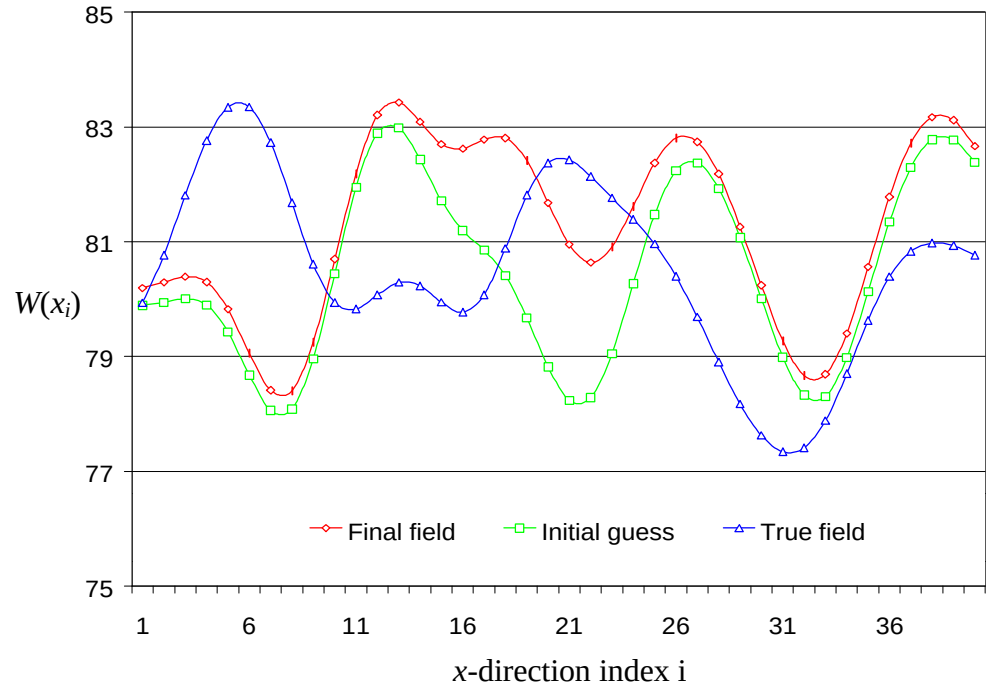

Fig. 5.6 – Width $W(x)$ of the channel.

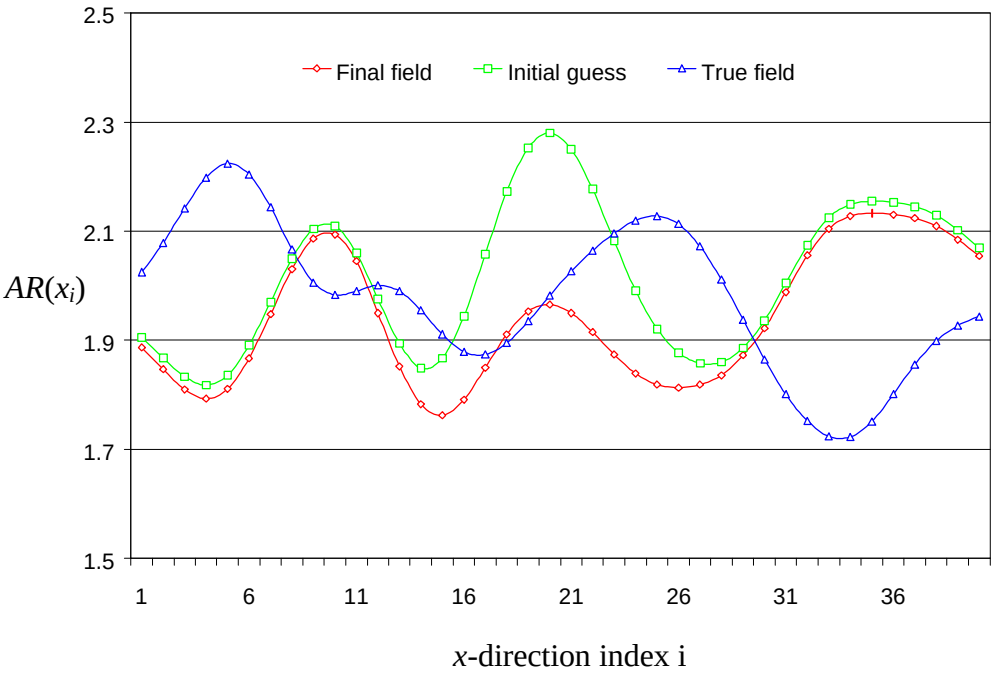

Fig. 5.7 – Aspect ratio $AR(x)$ of the channel.

As we can see, the final fields from inversion are very different from the true fields except around the well location (i=20). For example, the true horizontal sinuosity at i=24 is $S_h(24)$=-29.6 ft. The initial guess for this is 24.4 ft and the final inversion value is 27.8ft. In the above example, we used a value of 676 as the model variance for $S_h(x)$; hence, the squared mismatch $(24.4\text{-}27.8)^2$ =11.56 in $S_h(24)$ can only contribute 11.56/676 = 0.02 in the objective function, which is a comparatively negligible number. The vertical sinuosity field exhibits the same phenomena but is better matched around the well location (i = 20) since it is associated with the top depth of the channel and the top depth was taken as conditioning data. Comparatively, the width and aspect ratio of the channel are somewhat "closer" to the true case, especially around the well location. These two fields control the size or volume of the channel. So this suggests that matching long time (pseudo-steady state flow) pressure may reduce the uncertainty in channel volume.

The reason that the width and aspect ratio are closer to the true fields around the well, see Figs. 5.6 and 5.7, is that the observed channel thickness, i.e., the ratio of width to aspect ratio at the well, was conditioning data. For example, in the conditional realization, $W(20)$=81.67ft and $AR(20)$=1.96, so $W(20)/AR(20)$=41.5ft which is almost identical to the observed channel thickness (41.4ft).

5.2 Case 2: Well Out Of the Channel in the Initial Guess

In this case, we consider the case where the unconditional realization of the channel from the prior is such that the well is out of the channel. Recall that this unconditional realization is used as an initial guess in the Levenberg-Marquardt algorithm.

As in Case 1, an unconditional realization represents the true case and the well at which we obtain synthetic pressure data is located within the channel and the well is fully

penetrating the channel in the vertical direction. Based on this true model and the single-phase flow simulator, we simulate the pressure response at the well location to obtain well test pressure data. Then, we add noise to get our synthetic pressure data. We still assume constant porosity and permeability inside and outside the channel. The dimension of the grid is 40×25×10.

Table 5.3 lists all the parameters used for this case. For this example, pressure data during pseudo-steady state flow are available. Theoretically, the most important reservoir property that can be estimated from single-phase pseudo steady-state flow data is the total pore volume of the reservoir, which for our example, would be controlled by the total channel volume since channel and non-channel porosities are fixed. Therefore, if we use pseudo-steady state pressure data as conditioning data, then we should be able to estimate the total channel volume or pore volume of the channel.

Fig. 5.8 shows the simulated pressure, pressure drop as well as the derivative of the pressure up to 8 days, based on the true model. We can see from this figure, the pressure derivative approaches a constant (418.303 psi/day) for t>1.0 days, which indicates pseudo steady-state flow. The total pore volume in the true model is 13.43×10^5 ft^3; therefore the theoretical value of pressure derivative for the system is

$$\frac{\partial \Delta p}{\partial t} = \frac{5.615q}{c_t PV} = 418.268\,(\text{psi/day}), \tag{5.0}$$

which is essentially the same as the pressure derivative obtained from the simulated pressure data, see Fig. 5.8. The first eleven pressure data points will be used for matching; the last five of these correspond to pseudo steady-state flow.

Table 5.3 - Parameters for case 2

Principal direction line: $\bar{y}_0 = 100.0\text{ft}$, $\bar{z}_0 = 50.0\text{ft}$, $\bar{s}_{xy} = 0.05$, $\bar{s}_{xz} = 0.0$,

$s^2_{y0} = 1.0$, $s^2_{z0} = 1.0$, $s^2_{s_{xy}} = 0.001$, $s^2_{s_{xz}} = 0.001$.

Sinuosity of the center line: $s^2_{S_h} = 900.0$, $s^2_{S_v} = 4.0$, $a_{S_h} = a_{S_v} = 80\text{ft}$.

Width and aspect ratio: m_W=80.0ft, $s^2_W = 4.0$, a_W=80ft.

m_{AR}=1.5, $s^2_{AR} = 0.0250$, a_{AR}=80ft.

Gridblock Size: $\Delta x = \Delta y = \Delta z$=10ft.

Porosity inside and outside of the channel: 0.3, 0.1

Permeability inside and outside of the channel: 100md, 5md

Parameters for flow simulation or drawdown test

Fluid viscosity:	0.5 cp
Total compressibility:	10^{-5} 1/psi
Initial reservoir pressure:	3500 psi
Production rate:	1000 rb/d
Testing period:	3 days
Well radius:	0.3ft
Well location:	*iwell*=24, *jwell*=13

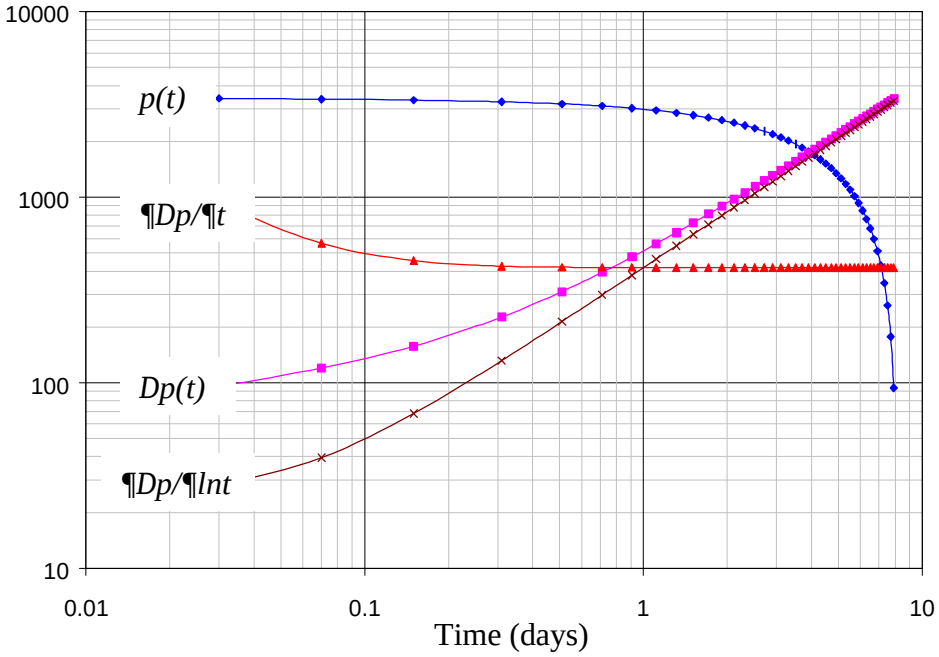

Fig. 5.8 – Pressure response and pressure derivative for case 2.

Fig. 5.9 shows layer 5 cut from the true model, the unconditional realization and the initial guess respectively, intended to have a clear view of the well location. Figs. 5.9(b) and (c) are identical because we use the unconditional realization as the initial guess in the Levenberg-Marquardt algorithm. Notice that the well gridblock colored black is out of the channel in the unconditional realization and the initial guess.

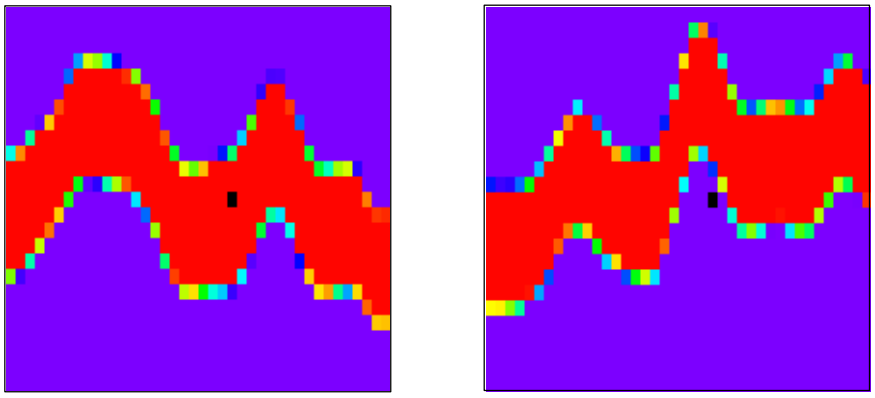

(a) from true model. (b) from the unconditional realization

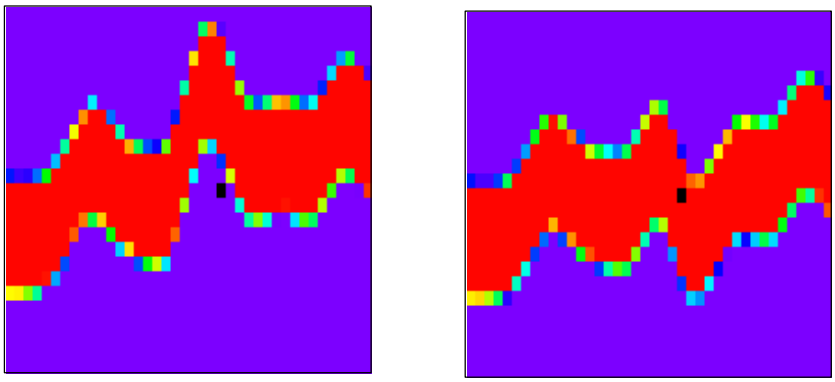

(c) from initial guess. (d) from the 1st iteration.

Fig. 5.9 – Layer 5 cut from the models, the black cells show the well location in each case, (a) from the true model, (b) from the unconditional realization, (c) from the initial guess (identical to (b) since the unconditional realization is taken as initial guess), (d) from the 1st iteration of the Levenberg-Marquardt algorithm.

Since the well is outside the channel, the permeability and porosity around the well are much lower than in the true case. Pressure mismatch is large at the first iteration step and dominates the gradient of the objective function. Therefore, if we used a Gauss-Newton procedure without a severe restriction on step size, we would take a large step. When this happens, the Gauss-Newton procedure often converges to a local minimum which gives an unreasonably high pressure mismatch. The damping factor a in the Levenberg-Marquardt algorithm usually eliminates this problem if the value of a is large enough. In our results, we used $a=1000$ in the first iteration of Levenberg-Marquardt algorithm. The objective function evaluated at the initial guess is 1.76×10^{6}, which is virtually all due to the pressure mismatch. At the first proposed update of the model, the objective function is larger than at the initial guess. According to Levenberg-Marquardt algorithm, we increase a by 10, then recompute a new proposed update and recalculate the objective function. Fig. 5.10 shows the change of the objective function as the value

of a increases from 1000. Note a must be increased to 10^6 before we update a model which reduces the objective function below its value at the initial guess. This corresponds to a relocation of the channel by the Levenberg-Marquardt algorithm so that the well is within the channel (see Fig. 5.9 (d)). This example illustrates the effectiveness of the Levenberg-Marquardt algorithm. As seen later, however, it is more effective to do a simple step which automatically moves the channel so that the well is located properly according to whether the channel is observed at the well.

Fig. 5.11 shows the change in the objective function and channel volume as the iteration of the Levenberg-Marquardt algorithm proceeds. The true channel volume is $1.712\times10^6 ft^3$. At convergence, the channel volume of the realization is $1.711\times10^6 ft^3$ as shown in the figure, which is very close to the true channel volume.

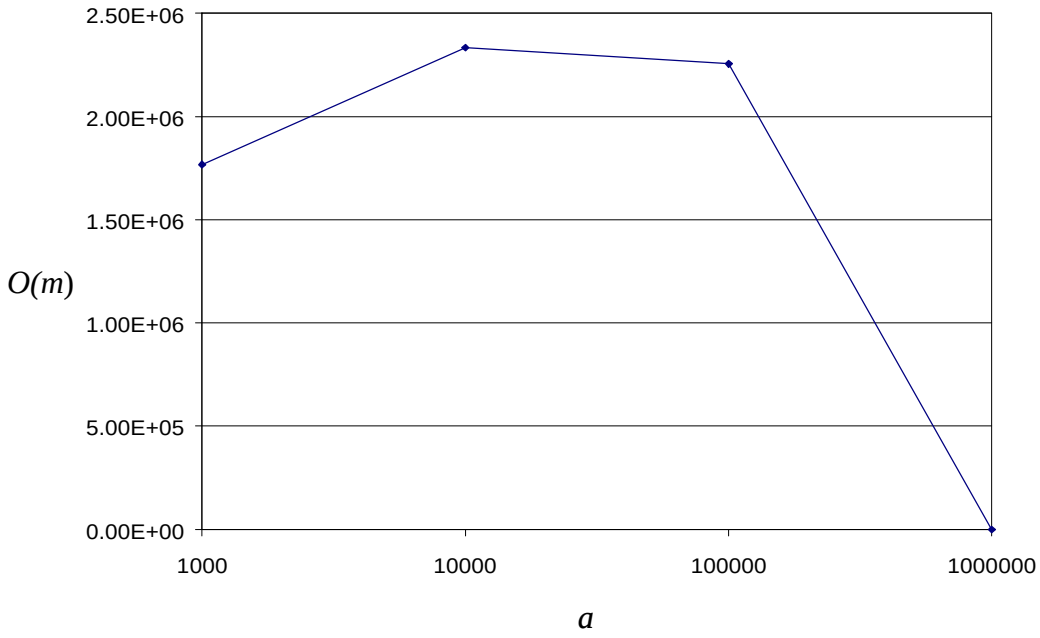

Fig. 5.10 – Objective function $O(m)$ versus damping factor a in the 1st iteration.

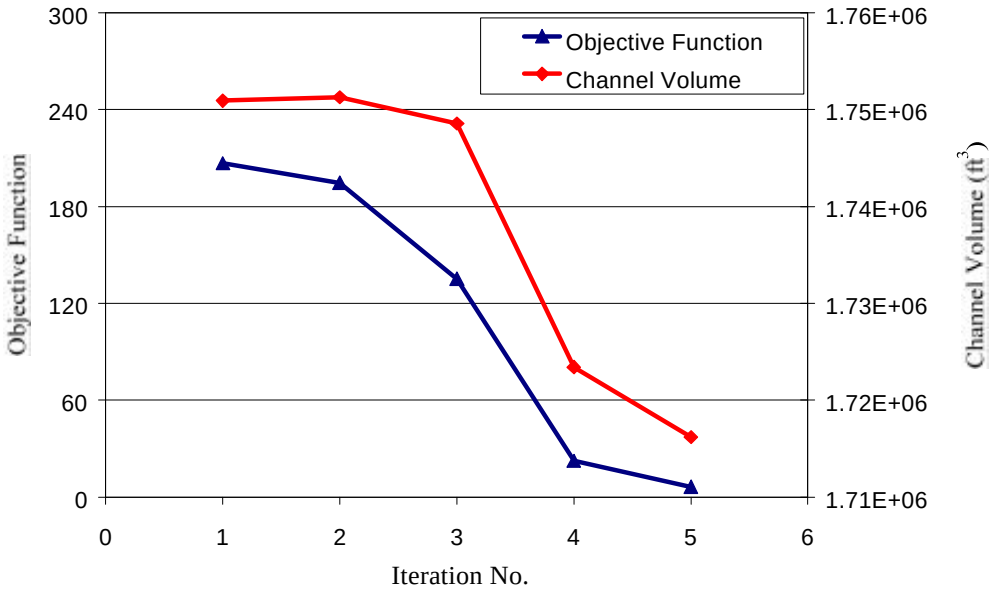

Fig. 5.11 – Objective function and channel volume change for case 2.

Although not shown, the observed channel thickness and top depth are also well matched in this case since they are observed data. The observed channel thickness and top depth at the well location are 53.6ft and 86.3ft and the calculated values at the well location of the realization are 53.4ft and 86.2ft, respectively. The pressure match is shown in Fig. 5.12. The average sum of squared pressure mismatch is 0.62 in this case, which represents an acceptable match of pressure data.

Figs. 5.13 through 5.18 compare the model parameters which include the four random variables for the principal direction line, the four random fields and channel thickness field. There are three curves in each figure. They represent the true random field, an unconditional realization from the prior, and the final field obtained from the inversion process. Pressure data are of course not adequate to resolve these parameters. We can see this clearly from the results in these figures. For example, the true value for $S_h(23)$ is 12.6 (see Fig. 5. 13), from the unconditional realization of the prior $S_h(23)$=79.9,

and from the inversion result $S_h(23)=44.4$, which is much closer to the true value than the unconditional realization because the location is just next to the well location in the x-direction and $S_h(x)$ is related to the well location in the channel and in the y-direction.

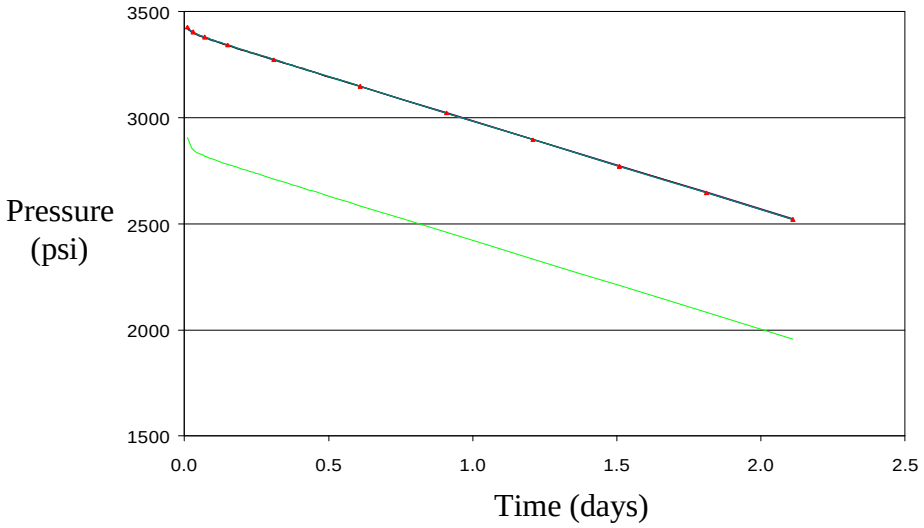

Fig. 5.12 – Pressure match for Case 2, the gray line represents the pressure response calculated from the initial guess, triangles are the observed pressure and the black line represents the calculated pressure at initial guess.

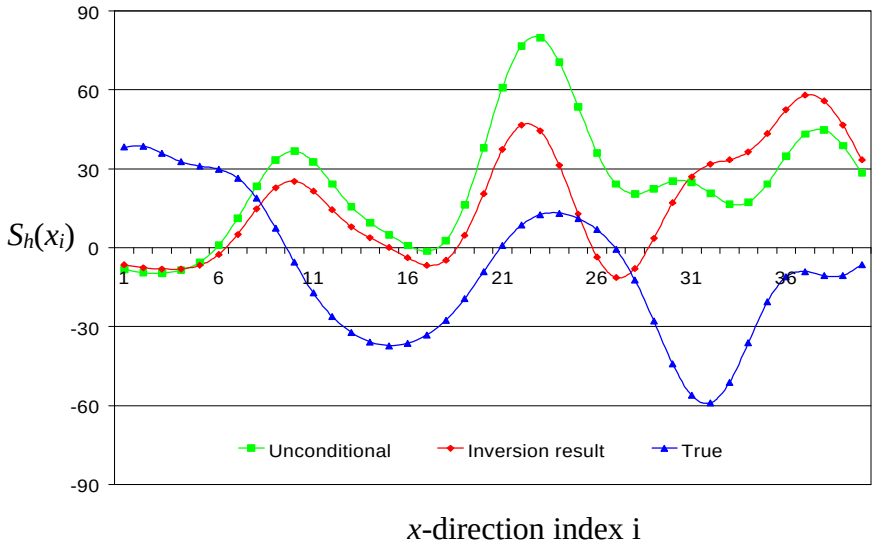

Fig. 5.13 – Horizontal sinuosity fields from the true, the unconditional realization of the prior and from the inversion result. The well is at i=24. The x-coordinate is actually the gridblock number in the x-direction.

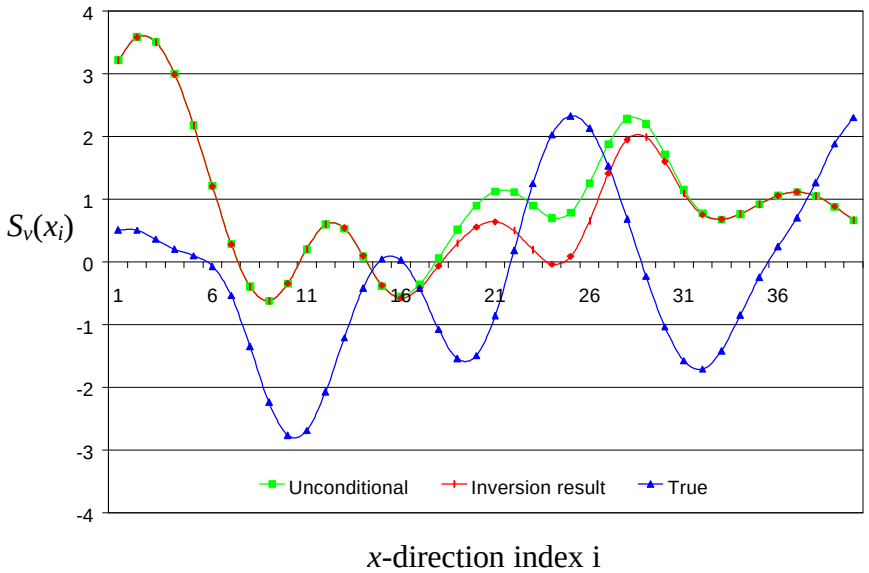

Fig. 5.14 – Vertical sinuosity of the channel from the true model, the unconditional realization and from the inversion result.

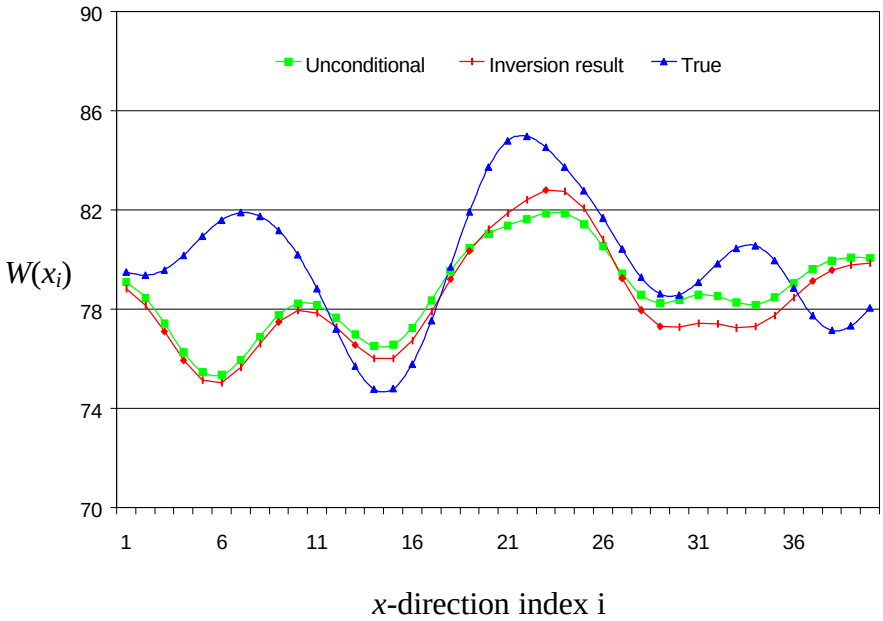

Fig. 5.15 – Channel widths from the true model, the unconditional realization of the prior and from inversion result.

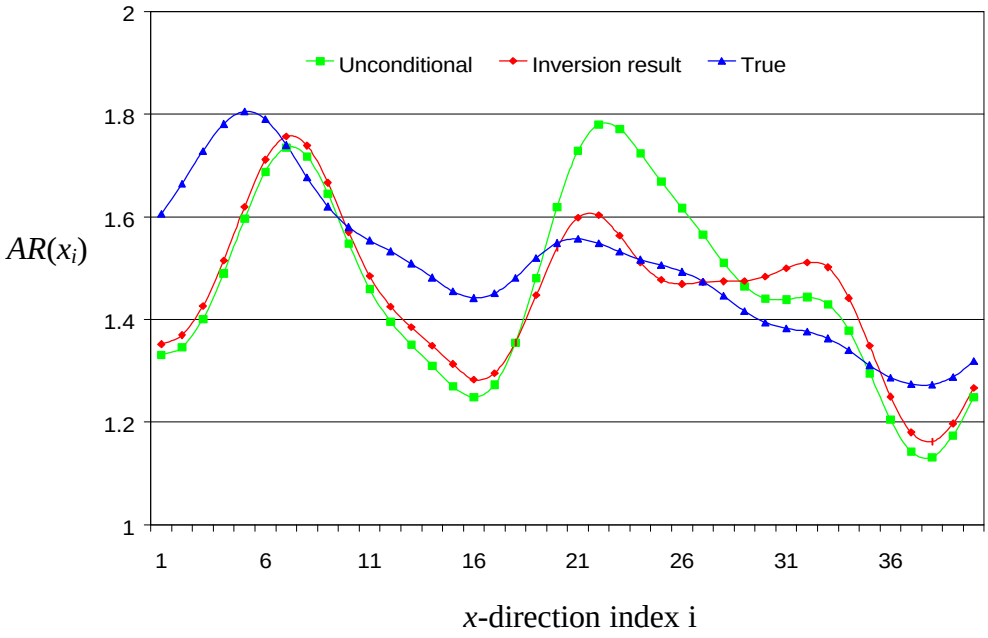

Fig. 5.16 – Aspect ratio of the channel from the true model, the unconditional realization and from the inversion result.

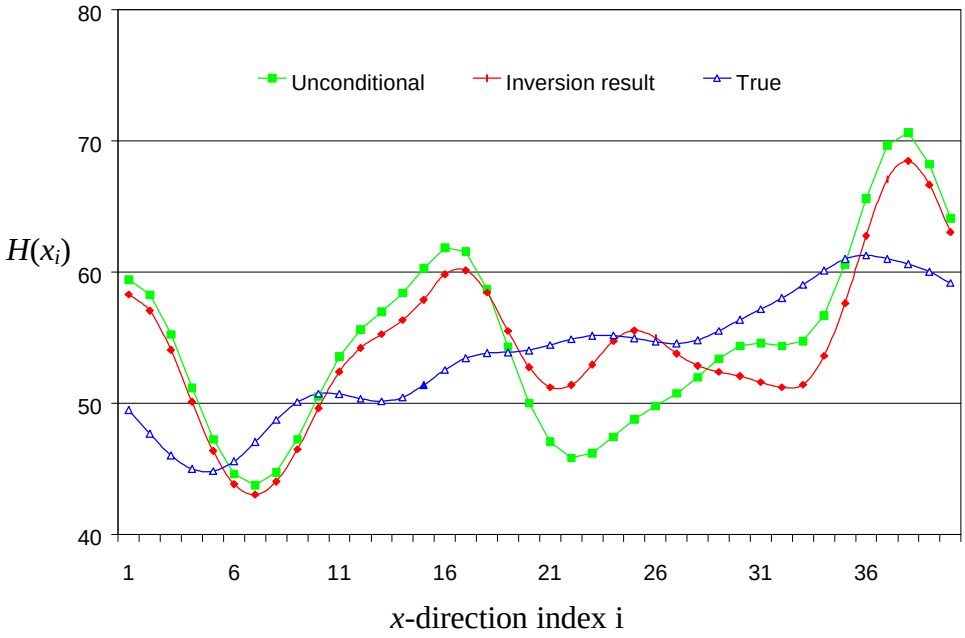

Fig. 5.17 - Channel thickness from the unconditional realization, inversion result and from the true model.

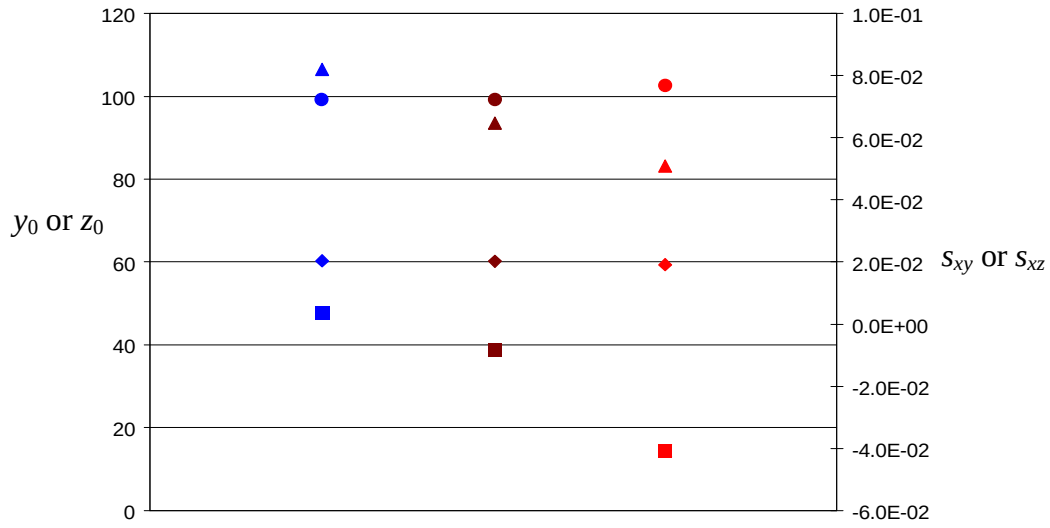

Fig. 5.18- Parameters for principal direction line, ✷'s represent y_0, ◆'s stand for z_0, ▲'s are s_{xy} and ■'s are s_{xz}. Symbols on the left represent the unconditional values, middle ones are true values and ones on the right are the inversion results. Inversion results are much closer to the true values after conditioning to the data.

Although the Levenberg-Marquardt algorithm may still converge for many initial guesses where the well is located out of the channel, in some cases, we found that the algorithm took a large number of iterations to converge or converged to models which gave a unreasonably large pressure mismatch. For example, for the above case, we started with a different unconditional realization of model parameters, and obtained the results shown in Fig. 5.19. In this case, the Levenberg-Marquardt algorithm did not converge within 11 iterations, meaning that the criteria on pressure mismatch and objective function were not satisfied. Fig. 5.19 shows the variation of objective function $O(m)$ with the number of iterations. The value of the objective function at the tenth iteration was 26 and the value at the eleventh iteration was 23.

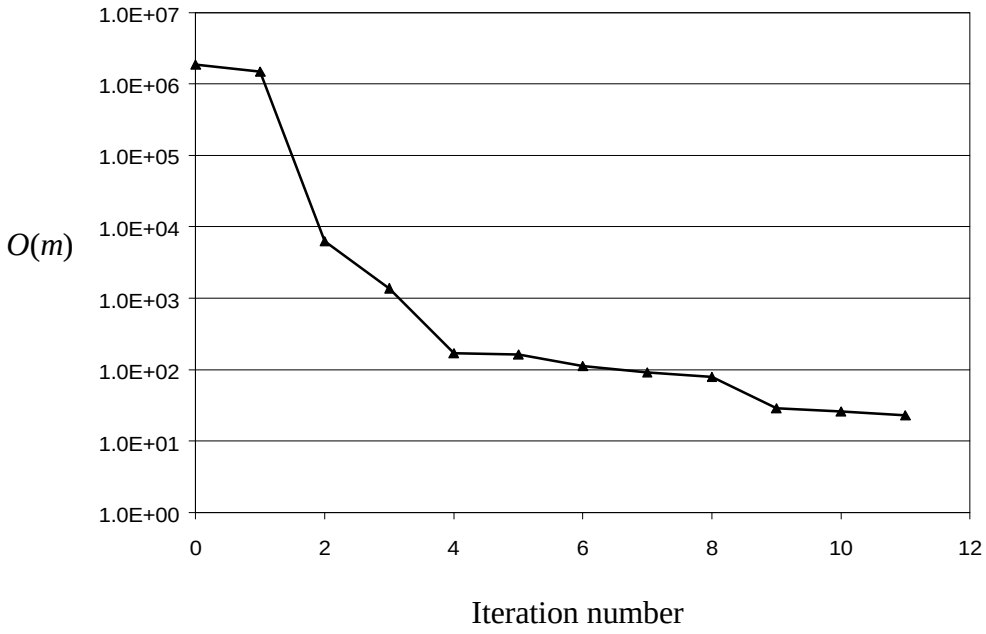

Fig. 5.19 - Change of objective function $O(m)$ with the number of iterations.

Obviously, the objective function evaluated at the initial guess is extremely large because the well is out of the channel represented by the initial guess. As described before, the pressure mismatch at the first iteration dominates the gradient of the objective function as well as the modification of the initial guess, i.e., dm^1. Therefore, we need to make a "smoother" change in the model parameters by using a large value of the damping factor a (initially a=1000) in the Levenberg-Marquardt algorithm. By examining the objective function based on the updated model parameters, it was found that there is a reduction in the objective function by using the initial value of a even though it is small. So the Levenberg-Marquardt algorithm goes on for another iteration. In fact, dm^1 is actually quite large and the channel obtained at the first iteration is quite strange; i.e., the model is quite rough in that channel parameters vary widely over a "small" distance, see Fig. 5.20b. Specifically, a=1000 is not large enough to control this

roughness. However, the objective function did decrease. There is no way to correct this rough change unless an appropriate value of a is known a priori.

We can explore this phenomenon more clearly in the change of the channel from iteration to iteration. Here we still use a layer cut from the reservoir because it is easy to analyze. Fig. 5.20 presents the 5^{th} layer of the reservoir at different iterations, which shows the shape and position of the channel as well as the well location (black) in the *x*-*y* plane.

In the initial guess, Fig. 5.20a, the well is out of the channel. Hence, the pressure response must be very different from the true pressure data mainly because the porosity (0.1) and permeability (5 md) outside of the channel are much lower than those within the channel (0.3 and 100 md respectively). This large difference will lead to a very high objective function (see the first point in Fig. 5.19). By using the Levenberg-Marquardt formula, i.e., Eq. 3.36 and setting the damping factor a=1000, we updated the initial guess as in Fig. 5.20 (b) and checked the objective function. In Fig. 5.20(b), we see that some of the model parameters around the well such as the horizontal sinuosity values, are over-modified. But the objective function is decreasing from the previous one even though the absolute value is still too high (see the second point in Fig. 5.19) and the well is not located to the inside of the channel.

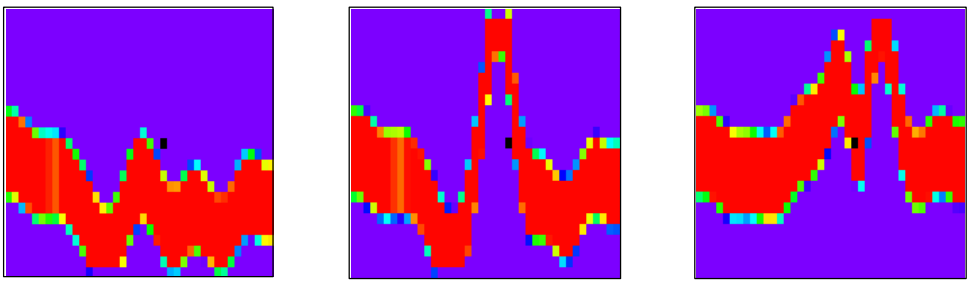

(a) Initial guess. (b) 1^{st} iteration. (c) 2^{nd} iteration.

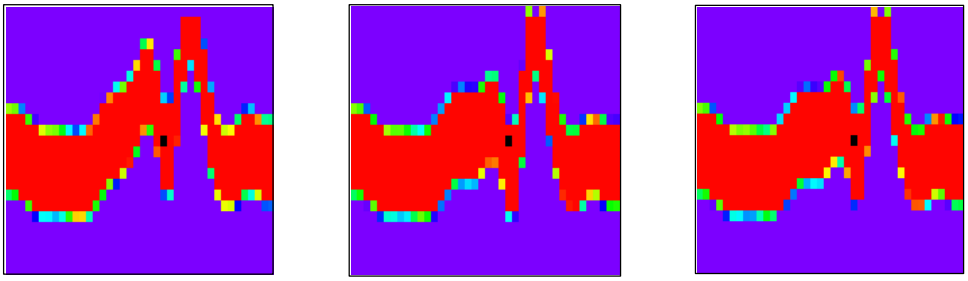

(c) 3rd iteration. (d) 4th iteration. (e) 5th iteration.

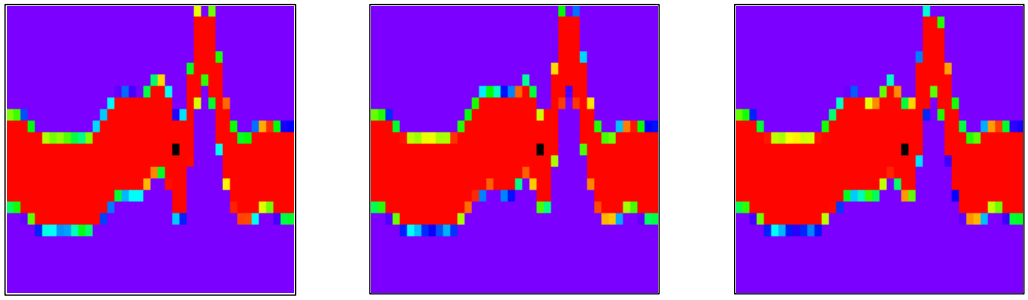

(f) 6th iteration. (g) 7th iteration. (h) 8th iteration.

Fig. 5.20 – Change of the channel with iterations

There is an abrupt reduction in the objective function from iteration 1 to iteration 2 since the updated channel is moved such that the well is within the channel and the observed pressure response is better matched. But this did not lead to rapid convergence because the channel boundaries are very rough. From Figs. 5.20 (d) through (h), the objective function was decreasing very slowly around a local minimum but did not actually converge after 11 iterations. Part of the reason is that a boundary effect appears in this case since we simply constrain our channel within the simulation grid. For example, if the index of the top boundary of the channel, $T_m(x)$, exceeds the maximum gridblock number (N_z), we simply set $T_m(x)/\Delta z=N_z$. A similar procedure is applied at other boundaries. This treatment induces some computational error in $\partial K/\partial m$. As we can see from Fig. 5.20 (b), the widths of the channel, e.g., $W(22)$ and $W(23)$, are much

smaller than the width at other locations since these two values are truncated in order to keep the channel within the grid. It may be possible for the algorithm to converge if more iterations are allowed. But this is too expensive. For example, it took 23.4 minutes of CPU time to do the 11 Levenberg-Marquardt iterations on a Pentium 400.

We found that it is better to position the well within the channel at the first iteration if the channel is observed in the well. This method saves computational time, and also tends to ensure that the modification to the model parameters in the Levenberg-Marquardt iterations is reasonably smooth.

Here, we propose to condition the prior channel model to the well locations directly, which is similar to performing kriging to honor the hard data for reservoir properties. In other words, we take the well location information as "hard data" when we generate realizations from the prior channel model. This procedure is discussed below in more detail.

Suppose there are N_w wells in the reservoir in which we have observed the channel. Denote the x and y coordinates of the center-line of the channel as x_c and y_c and the corresponding gridblock indices as ic and jc respectively. Here, x_c, y_c, ic and jc are all vectors with N_w elements. We wish to position the wells in the channel with some uncertainty in location when we generate realizations of the channel from the prior model. We consider only the model parameter vector m_G for channel geometry in m since the rock properties in m_r have nothing to do with the well locations. As before, we order the parameters in m_G as in Eq. 3.1

$$m_G = [\, y_0,\, z_0,\, s_{xy},\, s_{xz},\, \{S_{hi},\, i=1,2,\ldots,N_x\},\, \{S_{vi},\, i=1,2,\ldots,N_x\},\, \{W_i,\, i=1,2,\ldots,N_x\},\, \{AR_i,\, i=1,2,\ldots,N_x\}\,]^T. \tag{5.1}$$

Then the expression for each element of y_c, say $y_{ck}(m_G)$, in terms of the model parameters defined earlier is

$$\begin{aligned} y_{ck}(m_G) &= y_0 + x_{ck} s_{xy} + S_h[ic(k)] \\ &= m_{G,1} + x_{ck} m_{G,3} + m_{G,4+ic(k)}, \end{aligned} \tag{5.2}$$

for k=1,2,…,N_w. This is a linear function of model parameters. So we can rewrite the general expression of y_c as

$$\mathrm{y}_c(m_G)=Am_G, \tag{5.3}$$

where A is a $N_w \times M$ (M=4N_x+4 is the number of parameters in m_G) coefficient matrix with each row having a structure like

$$[1, 0, x_{ck}, 0, \boldsymbol{e}_k, \{0,\ldots\ldots,0\}, \{0,\ldots\ldots,0\}, \{0,\ldots\ldots,0\}], \tag{5.4}$$

for k=1,2,…,N_w, where $\boldsymbol{e}_k$ is a unit vector with the $ic(k)^{\text{th}}$ element equal to 1 and all other elements equal to zero. We can see that the matrix A is actually the gradient of $y_c(m_G)$ with respect to m_G or the "sensitivity" of the calculated well locations to the model parameters. To condition $m_{G,uc}$, a unconditional realization, to $y_c(m_G)$, we minimize the objective function

$$\begin{aligned} F(m_G) = &\frac{1}{2}(m_G - m_{G,uc})^T C_G^{-1}(m_G - m_{G,uc}) + \\ &+ \frac{1}{2}(Am_G - y_{cobs})^T C_w^{-1}(Am_G - y_{cobs}), \end{aligned} \tag{5.5}$$

where y_{cobs} represents the y-coordinates of the observed center–line at the wells and C_w is a diagonal covariance matrix that measures the uncertainty of y_{cobs}. This ensures that the starting values for the channel geometry variables can be made to contain the wells. The minimum of the objective function, $F(m_G)$, gives a conditional realization of m_G conditioned to "hard data", i.e., the channel center-line, and the prior information

contained in $m_{G,prior}$. The minimum of $F(m_G)$ can be obtained analytically. In fact, the gradient of $F(m_G)$ is

$$\nabla F(m_G) = C_G^{-1}(m_G - m_{G,uc}) + A^T C_w^{-1}(Am_G - y_{cobs}). \tag{5.6}$$

Setting $\nabla F(m_G)$ to be equal to zero, we have,

$$\begin{aligned} C_G^{-1}(m_G - m_{G,uc}) &= -A^T C_w^{-1}(Am_G - y_{cobs}) \\ &= -(A^T C_w^{-1} A)m_G + A^T C_w^{-1} y_{cobs}. \end{aligned} \tag{5.7}$$

In order to solve for m_G, we simply add $(A^T C_w^{-1} A)(m_G - m_{G,uc})$ to both sides of the above equation to obtain

$$(C_G^{-1} + A^T C_w^{-1} A)(m_G - m_{G,uc}) = -A^T C_w^{-1}(Am_{G,uc} - y_{cobs}). \tag{5.8}$$

Therefore, the conditional realization of m_G, denoted by m^0, (we use this notation to indicate that m^0 will be used as an initial guess of m_G for the Levenberg-Marquardt algorithm) will be

$$m^0 = m_{G,uc} - \left[C_G^{-1} + A^T C_w^{-1} A\right]^{-1} A^T C_w^{-1}(Am_{G,uc} - y_{cobs}), \tag{5.9}$$

or

$$m^0 = m_{G,uc} - C_G A^T \left[C_w + AC_G A^T\right]^{-1}(Am_{G,uc} - y_{cobs}), \tag{5.10}$$

where the last result was obtained from the following matrix inverse lemma (see [24]),

$$\left[C_G^{-1} + A^T C_w^{-1} A\right]^{-1} A^T C_w^{-1} = C_G A^T \left[C_w + AC_G A^T\right]^{-1}. \tag{5.11}$$

If we have only one well, then, $C_w = s^2_{y_{c1}}$ and $AC_G^{-1}A^T$ is just a number, so it is trivial to calculate m^0.

Based on this scheme, we repeated the last example. Instead of using an unconditional realization of the prior as an initial guess of the model parameters, we use

m^0 from Eq. 5.10 as the initial guess of the Levenberg-Marquardt algorithm. We have just one well in the reservoir and we know that x_{cobs}=240ft, y_{cobs}=130ft, $ic(1)$=24 and $jc(1)$=13. Assume $C_w = s^2_{y_{c1}} = 1.0$, then it is easy to calculate m^0 from Eq. 5.10. Fig. 5.21 shows layer 5 cut from the reservoirs based on $m_{G,uc}$ and m^0, respectively. The well is almost positioned in the middle of the channel in the y-direction (actually, next to the center block).

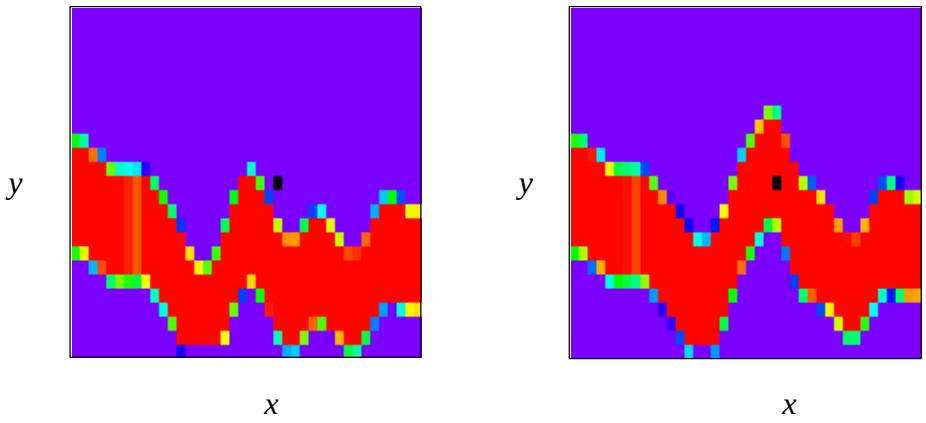

Fig. 5.21 – A layer cut from the unconditional realization of the prior and the initial guess after conditioning to the channel centerline observed at the well, the well location is marked black.

Starting with this initial guess, the Levenberg-Marquardt algorithm converged in 3 iterations and took only 4.8 minutes of CPU time. The objective function goes initially from 1014.4 to 5.5 at iteration 3 and the average of the squared pressure mismatch is only about 0.06, which means a very good pressure match. The channel volume from the initial guess is 1.68×10^6 ft^3 and the channel volume after convergence is 1.72×10^6 ft^3, which is much closer to the true channel volume 1.71×10^6 ft^3. The observed channel thickness and top depth are also approximately honored. The calculated values are 53.4 ft and 87.1ft and the unconditional values are 54.9 ft and 86.6ft, respectively. Fig. 5.22 shows layers 1 to 7 cut from the 3D images of the reservoir based on a unconditional

realization of the prior, the initial guess m^0, the conditional realization from the inversion process and the true model, respectively.

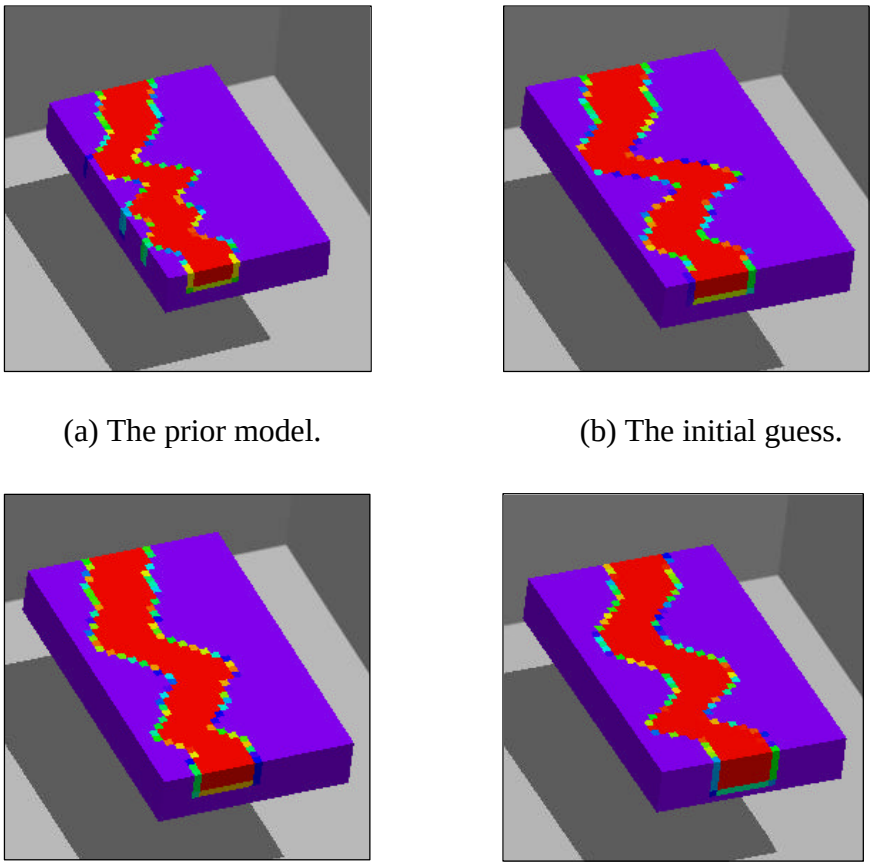

(a) The prior model. (b) The initial guess.

(c) Inversion result. (d) True Model.

Fig. 5.22 – Layer 1-7 cut from the entire reservoir, (a) a realization from the prior model; (b) an initial guess based on an unconditional realization conditioned to the observed center-line at the well; (c) final channel conditioned to pressure and observed thickness and top depth; (d) the true channel.

5.3 Case 3: Unknown Porosity and Permeability

In the last two cases, the porosity and permeability both inside and outside the channel were assumed to be known and the inverse process was applied only to generate realizations of the geometric parameters for the channel. As we can see from the results,

the inversion process is very successful. Here, we consider an example where we also wish to generate realizations of channel permeability and porosity and the permeability and porosity of the non-channel facies.

Channel permeability and porosity, respectively, are denoted by k_c and ϕ_c, whereas the permeability and porosity out of the channel are denoted by k_{nc} and ϕ_{nc}. Assume that k_c, ϕ_c, k_{nc} and ϕ_{nc} are independent Gaussian random variables with means and variances that represent our uncertainty in the values estimated from other sources of information, i.e., $\phi_c \sim N(\bar{\phi}_c, s^2_{\phi_c})$, $\phi_{nc} \sim N(\bar{\phi}_{nc}, s^2_{\phi_{nc}})$, $k_c \sim N(\bar{k}_c, s^2_{k_c})$ and $k_{nc} \sim N(\bar{k}_{nc}, s^2_{k_{nc}})$. By sampling these variables, we can generate realizations, but we wish to condition realizations to well-test pressure data. Thus, k_c, ϕ_c, k_{nc} and ϕ_{nc} are considered as additional model parameters. In this case, the vector of model parameters is given by

$$m = [\, y_0,\, z_0,\, s_{xy},\, s_{xz},\, \{S_{hi},\, i = 1,2,\ldots,N_x\},\, \{S_{vi},\, i = 1,2,\ldots,N_x\},$$
$$\{W_i,\, i = 1,2,\ldots,N_x\},\, \{AR_i,\, i = 1,2,\ldots,N_x\},\, k_c,\, k_{nc},\, \phi_c,\, \phi_{nc}]^T. \qquad (5.12)$$

We need to incorporate $s^2_{k_c}, s^2_{k_{nc}}, s^2_{\phi_c}$ and $s^2_{\phi_{nc}}$ in the C_M matrix as four diagonal entries. We can simply apply the chain rule to calculate the sensitivities of pressure to k_c, ϕ_c, k_{nc} and ϕ_{nc}, i.e., for j=1,2,……, N_p,

$$\frac{\partial p_j}{\partial k_c} = \sum_{b=1}^{N_b} \frac{\partial p_j}{\partial k_b} \frac{\partial k_b}{\partial k_c}, \qquad (5.13)$$

$$\frac{\partial p_j}{\partial k_{nc}} = \sum_{b=1}^{N_b} \frac{\partial p_j}{\partial k_b} \frac{\partial k_b}{\partial k_{nc}}, \qquad (5.14)$$

$$\frac{\partial p_j}{\partial \phi_c} = \sum_{b=1}^{N_b} \frac{\partial p_j}{\partial \phi_b} \frac{\partial \phi_b}{\partial \phi_c}, \qquad (5.15)$$

$$\frac{\partial p_j}{\partial j_{nc}} = \sum_{b=1}^{N_b} \frac{\partial p_j}{\partial j_b} \frac{\partial j_b}{\partial j_{nc}}, \tag{5.16}$$

where $\partial p_j / \partial \mathrm{k}_\mathrm{b}$ and $\partial p_j / \partial j_\mathrm{b}$ are sensitivities of j^{th} observed pressure to gridblock permeability k_b and porosity j_b and have been obtained previously. Here, we only need to calculate $\partial \mathrm{k}_b / \partial \mathrm{k}_\mathrm{c}$, $\partial \mathrm{k}_b / \partial \mathrm{k}_\mathrm{nc}$, $\partial j_b / \partial j_\mathrm{c}$ and $\partial j_b / \partial j_\mathrm{nc}$, i.e., the derivative of gridblock permeability and porosity with respect to k_c, k_nc, j_c and j_nc.

The gridblock permeability k_b is determined as follows,

$$\mathrm{k}_b = \begin{cases} \mathrm{k}_c & \text{if gridblock } b \text{ is inside the channel} \\ \mathrm{k}_{nc} & \text{if gridblock } b \text{ is outside the channel} \\ \mathrm{r}_b \mathrm{k}_\mathrm{c} + (1 - \mathrm{r}_b)\mathrm{k}_\mathrm{nc} & \text{if gridblock } b \text{ is intersected by a channel boundary} \end{cases} \tag{5.17}$$

where r_b is the fraction of the channel volume in boundary block b. Its value depends on which boundary gridblock b is considered. For example, if b is on the top boundary with indices (i_b, j_b, k_b), i.e., $b = (k_b\text{-}1)N_xN_y + (j_b\text{-}1)N_x + i_b$, then $r_b = P_t(i_b)/\Delta z$ if uniform grid is assumed (see Fig. 4.1). Similarly,

$$j_b = \begin{cases} j_c & \text{if gridblock } b \text{ is inside the channel} \\ j_{nc} & \text{if gridblock } b \text{ is outside the channel} \\ \mathrm{r}_b j_\mathrm{c} + (1 - \mathrm{r}_b) j_\mathrm{nc} & \text{if gridblock } b \text{ is intersected by a channel boundary} \end{cases} \tag{5.18}$$

It is straightforward to get $\partial \mathrm{k}_b / \partial \mathrm{k}_\mathrm{c}$, $\partial \mathrm{k}_b / \partial \mathrm{k}_\mathrm{nc}$, $\partial j_b / \partial j_\mathrm{c}$ and $\partial j_b / \partial j_\mathrm{nc}$ from Eqs. 5.17 and 5.18.

$$\frac{\partial \mathrm{k}_b}{\partial \mathrm{k}_\mathrm{c}} = \begin{cases} 1 & \text{if gridblock } b \text{ is within the channel} \\ 0 & \text{if gridblock } b \text{ is out of the channel} \\ r_b & \text{if gridblock } b \text{ is intersected by a channel boundary} \end{cases} \tag{5.19}$$

$$\frac{\partial \mathrm{k}_b}{\partial \mathrm{k}_\mathrm{nc}} = \begin{cases} 0 & \text{if gridblock b is within the channel} \\ 1 & \text{if gridblock b is out of the channel} \\ 1 - r_b & \text{if gridblock b is intersected by a channel boundary} \end{cases} \tag{5.20}$$

$$\frac{\partial j_b}{\partial j_c} = \begin{cases} 1 & \text{if gridblock } b \text{ is within the channel} \\ 0 & \text{if gridblock } b \text{ is out of the channel} \\ r_b & \text{if gridblock } b \text{ is intersected by a channel boundary.} \end{cases} \tag{5.21}$$

$$\frac{\partial j_b}{\partial j_{nc}} = \begin{cases} 0 & \text{if gridblock } b \text{ is within the channel} \\ 1 & \text{if gridblock } b \text{ is out of the channel} \\ 1 - r_b & \text{if gridblock } b \text{ is intersected by a channel boundary} \end{cases} \tag{5.22}$$

Next, we consider an example. All the channel parameters and fluid properties are exactly the same as in Case 2, see Table 5.3. But the well is located at (20,13) and the following statistical parameters for k_c, k_{nc}, j_c and j_{nc} are specified:

$$\bar{k}_c = 100\,\text{md},\ \bar{k}_{nc} = 5\,\text{md},\ \bar{j}_c = 0.3,\ \bar{j}_{nc} = 0.1;$$

$$s^2_{k_{ci}} = 25,\ s^2_{k_{nc}} = 0.0025,\ s^2_{j_c} = 0.0025,\ s^2_{j_{nc}} = 0.0001.$$

Tables 5.4 and 5.5 list all the parameter values sampled from the corresponding Gaussian variables and fields for the model parameters in order to obtain the "true" reservoir. The true channel volume is 1.78×10^6 ft^3 and the channel thickness and top depth at the well are 56.93 ft and 80.1 ft, respectively.

Table 5.4 - True model parameters for case 3

True Model parameters			
y_0	99.02 ft	k_c	96.02 md
z_0	50.19 ft	k_{nc}	5.00 md
s_{xy}	0.07	j_c	0.24
s_{xz}	0.01	j_{nc}	0.09

Table 5.5 – True model parameters for case 3 (continued)

i	$S_h(x_i)$	$S_v(x_i)$	$W(x_i)$	$AR(x_i)$
1	-32.94	-0.87	83.11	1.49
2	-38.25	-0.89	83.93	1.46
3	-35.53	-0.87	84.35	1.39
4	-24.21	-0.86	84.23	1.31
5	-7.85	-0.80	83.63	1.24
6	7.97	-0.58	82.74	1.21
7	19.11	-0.15	81.85	1.22
8	24.84	0.37	81.20	1.26
9	27.32	0.77	81.00	1.31
10	29.56	0.92	81.38	1.35
11	33.42	0.94	82.28	1.39
12	38.72	1.01	83.45	1.45
13	43.77	1.21	84.42	1.54
14	46.97	1.43	84.79	1.64
15	47.57	1.52	84.35	1.73
16	45.28	1.36	83.25	1.76
17	39.88	0.98	81.99	1.73
18	31.81	0.46	81.19	1.64
19	22.80	-0.03	81.32	1.53
20	14.70	-0.39	82.40	1.45
21	7.83	-0.68	83.95	1.41
22	0.67	-1.12	85.21	1.43
23	-8.18	-1.90	85.50	1.48
24	-17.83	-2.95	84.57	1.54
25	-25.05	-3.95	82.68	1.60
26	-26.43	-4.53	80.35	1.62
27	-21.48	-4.57	78.08	1.59
28	-13.61	-4.22	76.29	1.53
29	-8.04	-3.71	75.27	1.46
30	-8.47	-3.14	75.19	1.42
31	-14.39	-2.49	75.92	1.41
32	-21.48	-1.78	76.98	1.44
33	-24.43	-1.11	77.72	1.49
34	-20.71	-0.61	77.69	1.54
35	-12.01	-0.26	76.85	1.57
36	-2.93	0.13	75.58	1.56
37	2.25	0.73	74.44	1.53
38	2.12	1.52	73.90	1.48
39	-1.52	2.24	74.16	1.44
40	-5.36	2.58	75.13	1.43

By producing the well at 1000 rb/d, we get the pressure response for a 3-day test. By adding noise to the simulated pressure data, we obtain the observed pressure data as shown in Fig. 5.23 (triangles).

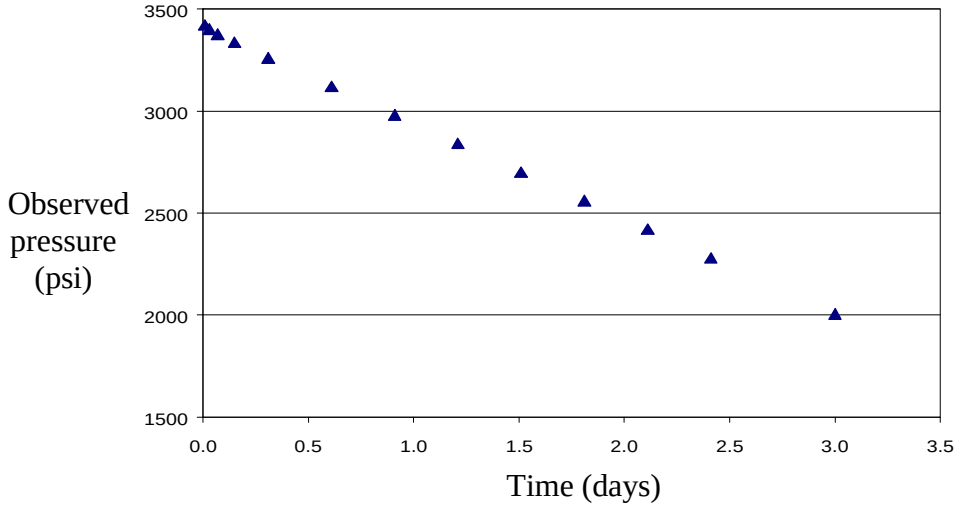

Fig. 5.23 – Observed pressure data for case 3.

Figs. 5.24(a) through 5.24(d) illustrate the sensitivities of gridblock permeability and porosity to k_c, k_{nc}, j_c and j_{nc}, i.e., $\frac{\partial k_b}{\partial k_c}$, $\frac{\partial k_b}{\partial k_{nc}}$, $\frac{\partial j_b}{\partial j_c}$ and $\frac{\partial j_b}{\partial j_{nc}}$. As we can see, $\partial k_b / \partial k_c$ is similar to $\partial j_b / \partial j_c$ and $\partial k_b / \partial k_{nc}$ is identical to $\partial j_b / \partial j_{nc}$ according to Eqs. 5.19 through 5.22. In Fig. 5.24 (b), $\partial k_b/\partial k_{nc} = 1$ out of the channel and 0 inside the channel. On the channel boundaries, $\partial k_b/\partial k_{nc}$ has different values.

The sensitivities of pressure with respect to k_c, k_{nc}, j_c and j_{nc}, i.e., $\frac{\partial p_j}{\partial k_c}$, $\frac{\partial p_j}{\partial k_{nc}}$, $\frac{\partial p_j}{\partial j_c}$ and $\frac{\partial p_j}{\partial j_{nc}}$ for $j=1,2,\ldots,N_p$, are calculated from Eqs. 5.13 through 5.16 and are shown in Fig. 5.25 where the horizontal coordinate j is equivalent to time and relative sensitivity to permeability k_c and k_{nc} is plotted.

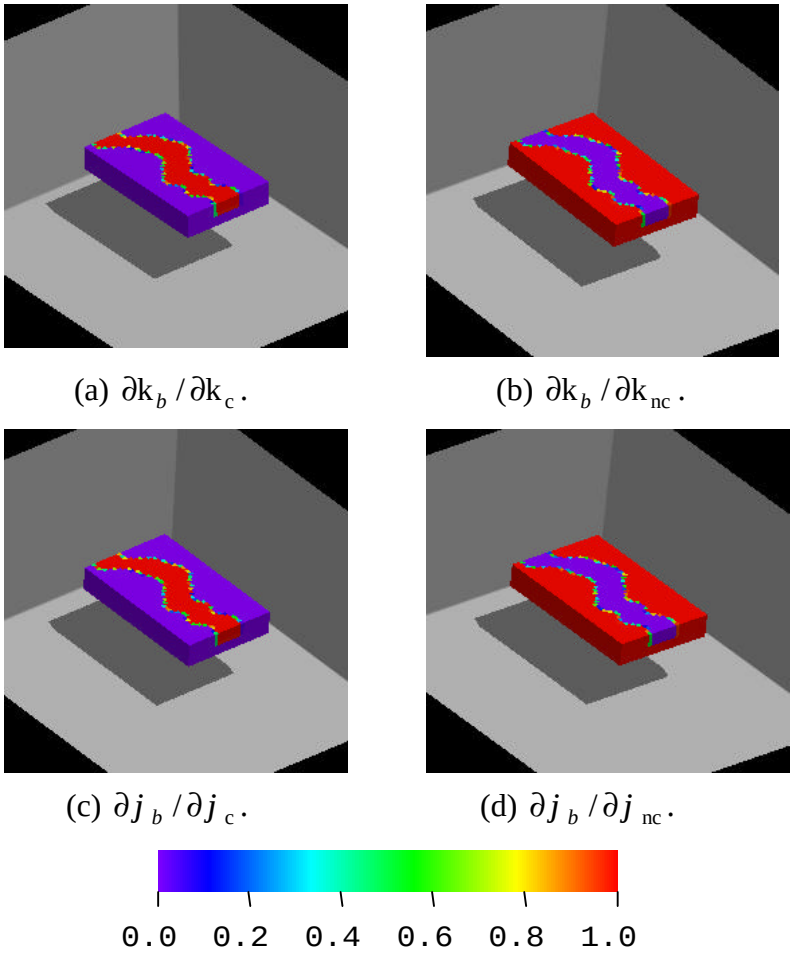

Fig. 5.24 – Sensitivities of gridblock permeability and porosity to k_c, k_{nc}, j_c and j_{nc}.

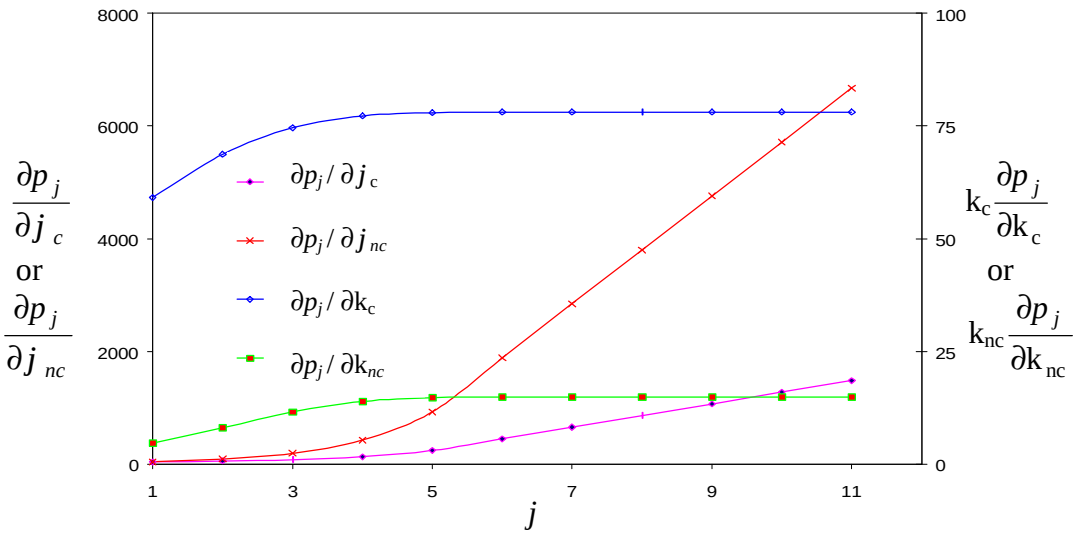

Fig. 5.25 – Sensitivities of pressure with respect to k_c, k_{nc}, j_c and j_{nc}.

Note that for $j > 6$, $\frac{\partial p_j}{\partial k_c}$ and $\frac{\partial p_j}{\partial k_{nc}}$ are constant, $\frac{\partial p_j}{\partial j_c}$ and $\frac{\partial p_j}{\partial j_{nc}}$ are straight lines.

This occurs because the fluid flow is in pseudo-steady state (*pss*) where the derivative of pressure with respect to time is inversely proportional to the average porosity of the system. In order to check this, we did a 5-day test. Fig. 5.26 shows the test pressure, pressure drop and the calculated pressure drop derivative. As we can see, after about t > 0.91 days, the pressure drop derivative becomes constant (467.03 psi/day). Since the total pore volume of the reservoir is 12.025×10^5 ft^3, the theoretical value of the pressure drop derivative is $\frac{5.615q}{c_t PV} = \frac{5.615\times1000}{12.025} = 466.94$ (psi/day), which is basically equal to the constant value shown in Fig. 5.26 and verifies pseudo-steady state flow.

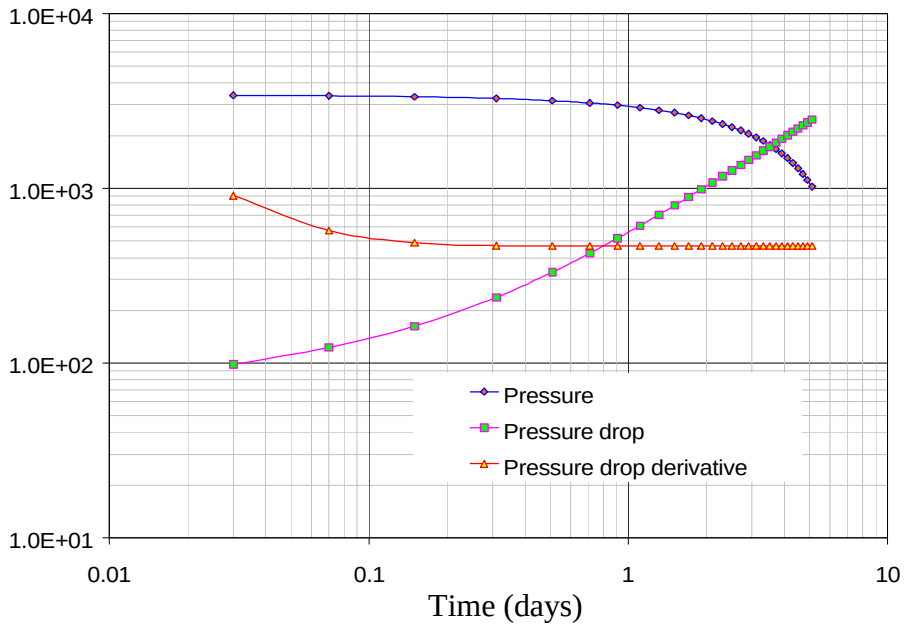

Fig. 5.26 – Pressure, pressure drop and its derivative for case 3.

As before, we generate realizations by randomized maximum likelihood method. After generating an unconditional realization $m_{G,uc}$ of the geometric parameters from the prior, we first condition to the channel centerline observed at the well location, see Eq. 5.10. The initial values (unconditional realizations) for k_c, k_{nc}, j_c and j_{nc} are, respectively, 101.83 md, 5.08 md, 0.36 and 0.12. After 3 iterations, the Levenberg-Marquardt algorithm converged in the sense that the average sum of the squared pressure error (SSE= 0.392) is less than the variance of the pressure data measurement error (1.0 psi^2). The value of the objective function decreases from an initial value of 1.1×10^5 to a minimum of 11.2. The total pore volume of the "true" reservoir is 1.202×10^6 ft^3, and the total pore volume based on the inversion results is 1.205×10^6 ft^3, which is approximately equal to the true pore volume. The observed channel thickness and top depth are also well honored in this case. Table 5.6 lists the values of k_c, k_{nc}, j_c and j_{nc} from the true case, the unconditional realization and the final results or conditional realization from the randomized maximum likelihood method. As we can see, the conditional results are very close to the true values.

Table 5.6 - Comparison of the values of k_c, k_{nc}, j_c and j_{nc}

	True value	Unconditional	Conditional
k_c	96.02	101.83	97.22
k_{nc}	5.00	5.08	5.08
j_c	0.24	0.36	0.23
j_{nc}	0.09	0.12	0.099

In this case, the total pore volume of the reservoir or the average porosity of the system appears to be well resolved by data. The permeability and porosity both inside and outside the channel are also well resolved.

5.4 Case 4: Multiple Realizations and Uncertainty Evaluation

In this example, we wish to generate multiple realizations of model parameters for channel geometry and rock property by the randomized maximum likelihood method so that we can characterize the uncertainty in model parameters. Again, we first generate a "true" model. Then, we put a synthetic well in the reservoir, which fully penetrates the reservoir in the vertical direction. Having the true model and the well location, the synthetic observed pressure data are obtained by running a flow simulator and then adding random noise to the simulated pressure data. For the example considered, we have both radial flow and linear flow data. The main purpose is to see whether the important properties, e.g., kh product, flow cross-section area (channel width times thickness), channel volume, etc., can be resolved.

The initial guess of the geometric model parameter vector for the Levenberg-Marquardt algorithm is obtained by conditioning an unconditional realization of the prior model only to the observed channel center at the well as in case 2 of this chapter.

Table 5.7 lists all the parameters used for this case. The dimension of the simulation grid is 60×40×15. So the total number of gridblocks is 36,000.

As noted previously, we obtained a true reservoir model by sampling the prior. Table 5.8 lists some of the model parameters and the true channel thickness and top depth at the well obtained from "the true reservoir". The true channel thickness and cross-sectional area (product of width and thickness) along the channel are shown in Fig. 5.27. We will use these two random fields for comparison and uncertainty evaluation.

Table 5.7 - Parameters for case 4

Principal direction line: $\bar{y}_0 = 180.0\text{ft},\ \bar{z}_0 = 80.0\text{ft},\ \bar{s}_{xy} = 0.05,\ \bar{s}_{xz} = 0.0,$

$s^2_{y0} = 1.0,\ s^2_{z0} = 1.0,\ s^2_{s_{xy}} = 0.0001,\ s^2_{s_{xz}} = 0.0001.$

Sinuosity of the center line: $s^2_{S_h} = 900.0,\ s^2_{S_v} = 100.0,\ a_{S_h} = a_{S_v} = 80\text{ft}.$

Width and aspect ratio: m_W=160.0ft, $s^2_W = 100.0$, a_W=80ft.

m_{AR}=2.5, $s^2_{AR} = 0.0625$, a_{AR}=80ft.

Gridblock Size: $\Delta x = \Delta y = \Delta z = 10\text{ft}$.

Porosity inside and outside the channel: $\bar{f}_c = 0.3,\ s^2_{f_c} = 0.0025$

$\bar{f}_{nc} = 0.1,\ s^2_{f_{nc}} = 0.0004$

Permeability inside and outside the channel: $\bar{k}_c = 100\text{md},\ s^2_{k_c} = 625$

$\bar{k}_{nc} = 0.1\text{md},\ s^2_{k_{nc}} = 0.0025$

Parameters for flow simulation or drawdown test

Fluid viscosity:	2.5 cp
Total compressibility:	10^{-5} 1/psi
Initial reservoir pressure:	3500 psi
Production rate:	1000 rb/d
Testing period:	0.5 days
Initial and maximum time step:	0.0001 day, 0.05 day
Time step multiplier:	1.2
Well radius:	0.3 ft
Well location:	*iwell*=37, *jwell*=23

Table 5.8 – True model parameters for case 4

Principal direction line: y_0=180.5 ft, z_0=81.4 ft, s_{xy}=0.064, s_{xz}=0.013
Permeability inside and outside the channel: k_c=134.1 md, k_{nc}=0.067 md
Porosity inside and outside the channel: j_c=0.26, j_{nc}=0.10
Channel thickness at the well: 81.6 ft
Top depth of the channel at well: 126.3 ft (from bottom of the reservoir)

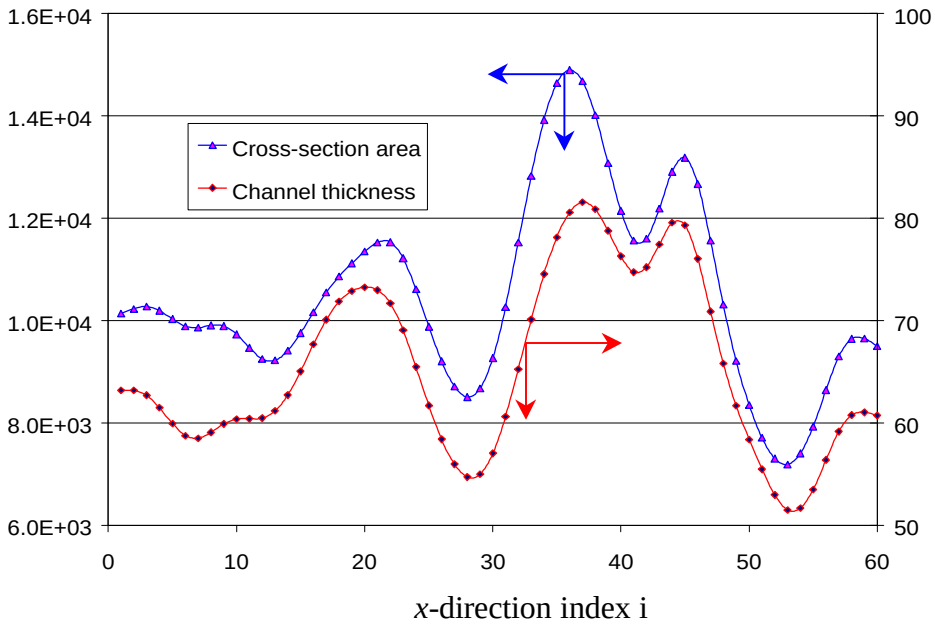

Fig. 5.27 – Channel thickness and cross-section area based on the true model.

Fig. 5.28 shows the true channel image and one slice cut from the entire reservoir which illustrates the well location (black cell) clearly.

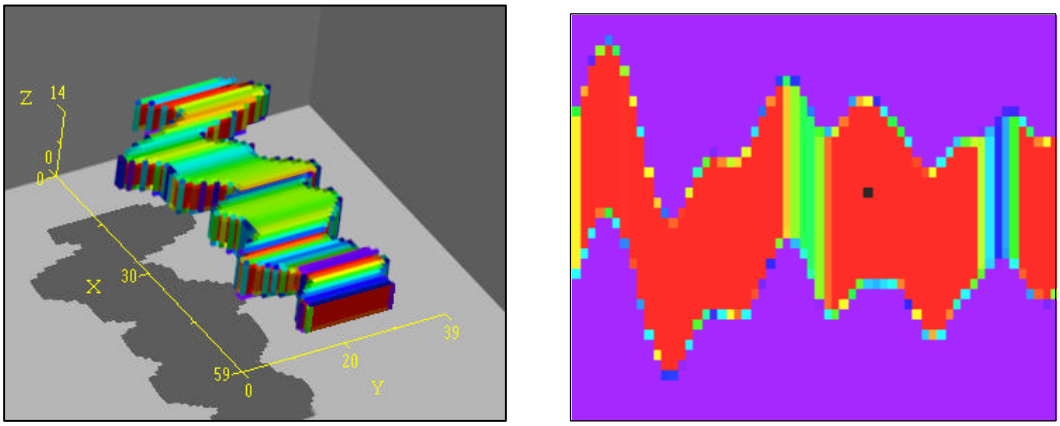

(a) True channel image. (b) Layer 7 cut from the reservoir.

Fig. 5.28 – True channel image and a layer cut from the reservoir.

Fig. 5.29 shows the simulated pressure drop and its derivative with respect to natural logarithm of time in a log-log plot for a half-day test. As we can see, from t = 0.001 day to about t = 0.01 day, the pressure derivatives is approximately constant, which indicates a radial flow regime. For t > 0.01 day, the pressure derivative exhibits a half slope straight line indicative of linear flow.

During radial flow in a layered reservoir of thickness h, the derivative of the pressure drop with respect to the natural logarithm of time is inversely proportional to the average kh product of the system, i.e., in field units,

$$\frac{\partial \Delta p_{wf}}{\partial \ln t} = \frac{70.6qm}{\bar{\mathrm{kh}}}, \tag{5.23}$$

where

$$\bar{\mathrm{kh}} = \sum_{i=1}^{N_z} \mathrm{k}_i \mathrm{h}_i , \tag{5.24}$$

where k_i and h_i represent the permeability and thickness of the gridblock layer *i* which is penetrated by the well in vertical direction. For the specific example under consideration, the well is fully-penetrating. The corresponding permeabilities (in millidarcies) of the gridblocks penetrated by the well are 0.067, 0.067, 0.067, 71.1, 134.1, 134.1, 134.1, 134.1, 134.1, 134.1, 134.1, 84.1, 0.067, 0.067, 0.067 and the gridblock size in the vertical direction is uniform and equal to 10 ft. therefore, $\bar{k}h \approx 10935$ and $\frac{\partial \Delta p_{wf}}{\partial \ln t} \approx 16.14$. If we neglect the permeability of the non-channel facies (it is very small compared to the channel permeability), then $\frac{\partial \Delta p_{wf}}{\partial \ln t} \approx 16.12$. But from Fig. 5.29, $\frac{\partial \Delta p_{wf}}{\partial \ln t} \approx 19$ based on the simulated pressure drop. It is unclear whether this difference is related to the use of the Peaceman's equation relating gridblock pressure to well-bore pressure or due to the variation in channel thickness, width and permeability values along the edges of the channel.

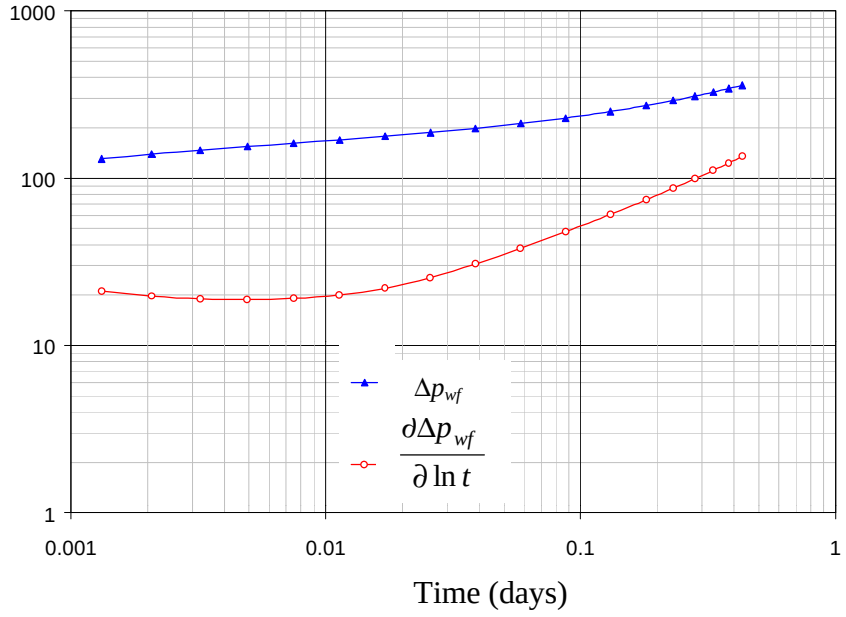

Fig. 5.29 – Simulated pressure drop and its derivative for case 4.

Table 5.9 lists the simulated pressure data selected from the complete set of pressure data generated from the simulator. The observed pressure data to be used as conditioning data were obtained by adding random noise assuming that measurement errors can be represented as independent identically distributed random variable with mean zero and variance 1 psi^2. Similarly, we add random noise to the true channel thickness and top depth as our observed data. The data variances used were 0.5 ft^2.

Table 5.9 – Conditioning pressure data for case 4

Time (days)	Pressure (psi)
0.00099	3374.079
0.00208	3360.021
0.00396	3348.575
0.0072	3337.941
0.01281	3327.266
0.03262	3306.037
0.05674	3288.244
0.09841	3264.197
0.17041	3231.259
0.29483	3184.84
0.44483	3136.148

As before, we generate realizations from the a posteriori pdf by using the randomized maximum likelihood method. The realizations generated are conditioned to the observed pressure data, channel thickness and top depth at the well location. Recall that in the randomized maximum likelihood method, each realization is generated by minimizing an appropriate objective function using the Levenberg-Marquardt algorithm.

Before we discuss the set of multiple realizations, we present some results from one realization.

Fig. 5.30 shows a plot of the objective function versus the number of Levenberg-Marquardt iterations used to generate a realization. In this case, the algorithm converged in four iterations. The objective function evaluated at the initial guess was greater than 100,000 and was reduced to 10 at the 4th iteration. The pressure data are very well matched as shown in Fig. 5.31. The observed channel thickness and top depth (not shown) were honored.

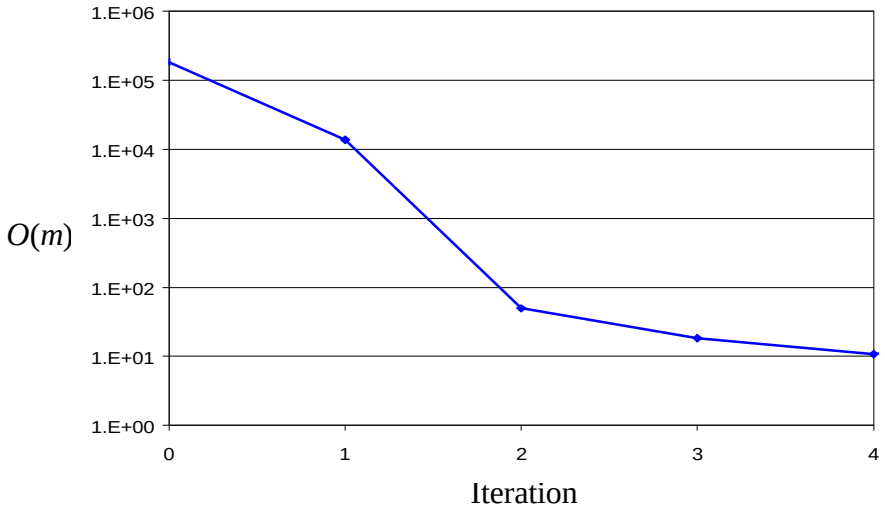

Fig. 5.30 – Objective function $O(m)$ versus the number of iterations.

Fig. 5.32 shows the channel thickness, i.e., $W(x)/AR(x)$, from the true model, the unconditional realization and from the conditional realization (inversion result). The x-axis of Fig. 5.32 is actually the value of the x-direction index. Clearly, the channel thickness at the well is honored since it is data. Around the well location, the conditional realization is much closer to the true case and away from the well location, the conditional realization is almost similar to the unconditional realization, i.e., the Levenberg-Marquardt optimization process resulted in only small change in the channel

thickness away from the well. This is simply a reflection of the fact that because of the short test time, the observed data are essentially insensitive to thickness at large distances from the well.

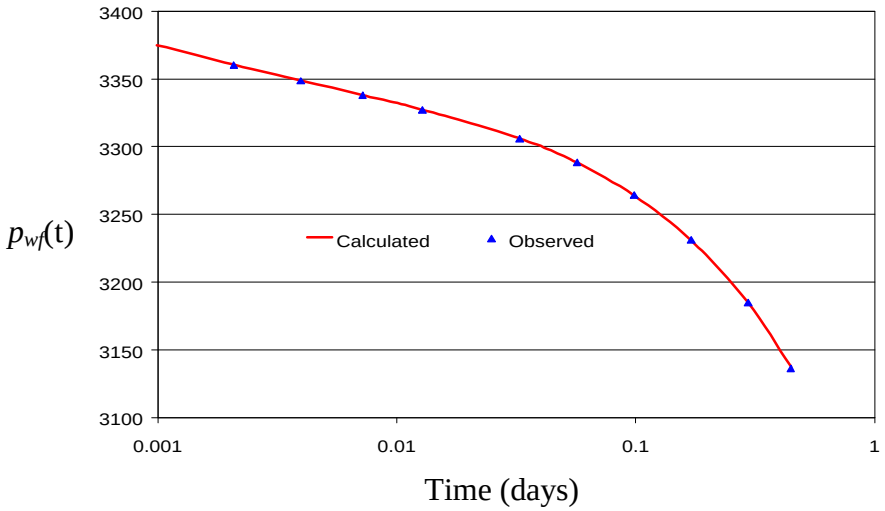

Fig. 5.31 – Pressure data matching.

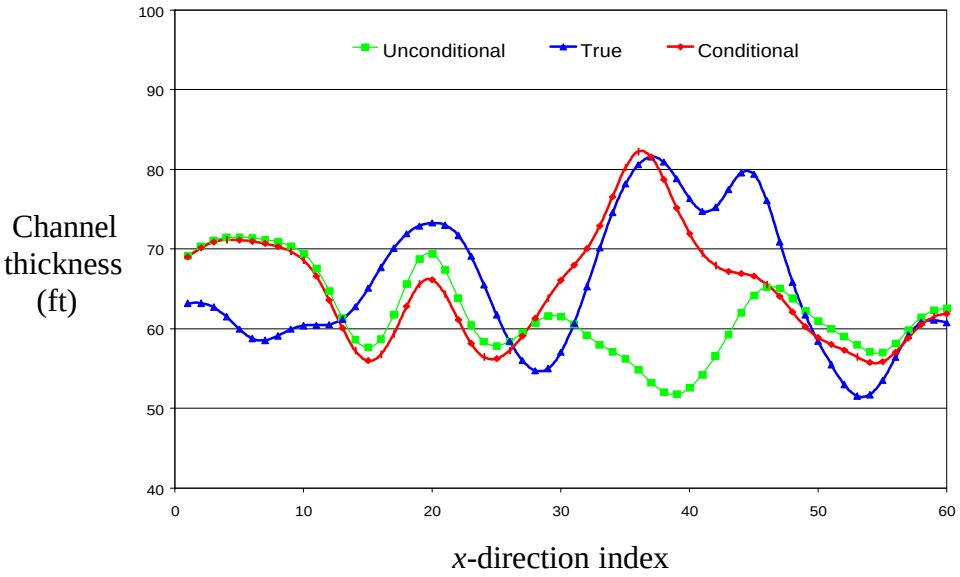

Fig. 5.32 – Channel thickness from the true model, an unconditional realization and the inversion results.

In this example, a realization for channel and non-channel permeability and porosity was also generated. Fig. 5.33 shows the change of k_c and k_{nc} with the number of

iterations in the Levenberg-Marquardt algorithm. The straight lines represent the true values of k_c and k_{nc}, whereas the curves with diamonds and triangles are the values of k_c (blue) and k_{nc} (red) at various iterations. As can be seen from this figure, the channel permeability k_c is very well resolved. The true value of k_c is 134.1 md and the value at convergence is 133.94 md. Since the non-channel facies permeability k_{nc} is very small and less important compared to k_c, it is not well recovered. Similar results were obtained for the porosity of channel and non-channel facies as shown in Fig. 5.34.

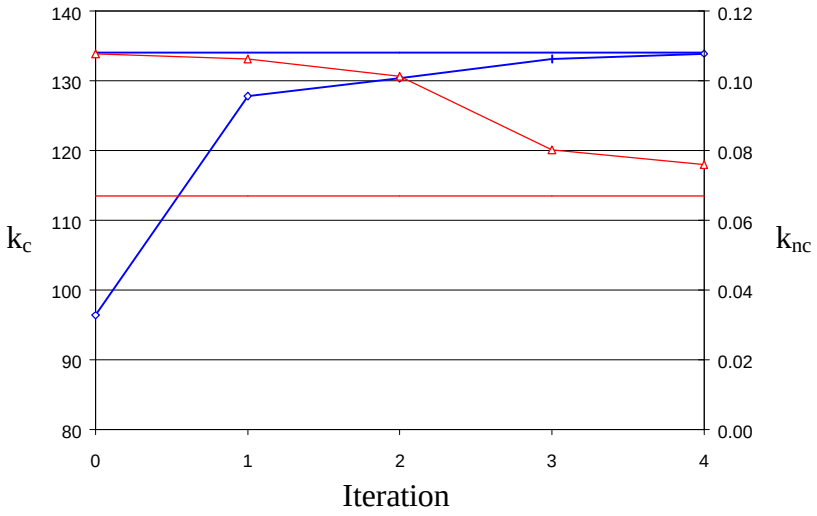

Fig. 5.33 – Channel permeability (k_c) and non-channel permeability (k_{nc}) versus the number of iterations.

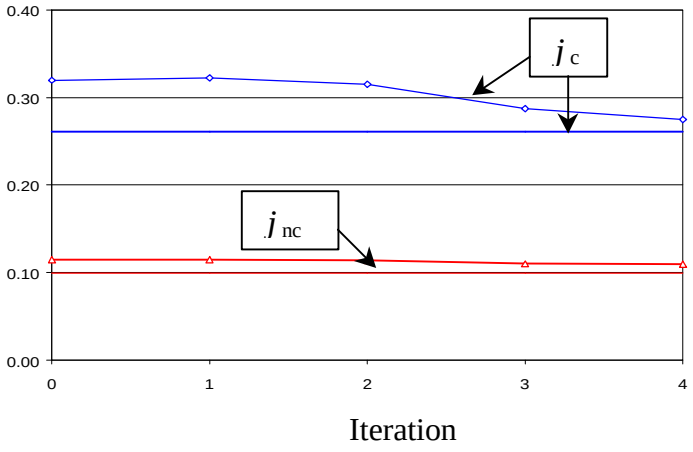

Fig. 5.34 – Channel and non-channel porosities versus iteration.

Following exactly the same procedure as for the realization just discussed, we generated 49 more realizations by the Levenberg-Marquardt algorithm for the evaluation of the uncertainty of all parameters. These results are presented next.

Fig. 5.35 shows 50 unconditional realizations (black curves) of the channel thickness, where the thicker curve represents the channel thickness from the true model. As indicated in this figure, the variation in thickness is the same at all points along the channel because no conditioning data are used. Recall that channel thickness is the ratio of width to the aspect ratio which is the explicit parameter.

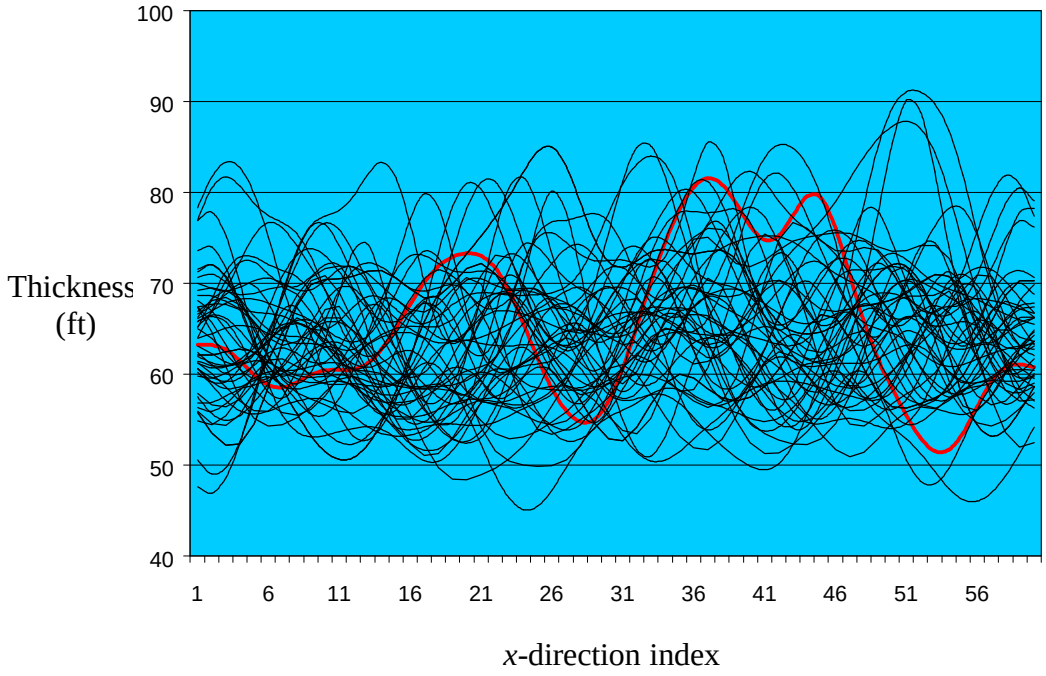

Fig. 5.35 – True channel thickness and unconditional realizations from the prior.

As described before, if we generate conditional realizations by conditioning to the observed radial flow pressure data and the channel thickness at the well, channel thickness at the well location should be well honored in all the realizations, and the $\overline{kh}$ product near the well should also be well resolved since the radial flow pressure response

is mainly controlled by the kh product of the channel. In other words, relatively small variation in channel thickness around the well is expected in multiple realizations. Fig. 5.36 illustrates this phenomenon. Again, the thicker curve in Fig. 5.36 is the true channel thickness and all the black curves represent 50 conditional realizations from the inversion process. As we can see, the variation of the channel thickness around the well (*x*-direction index = 37) is much narrower than other locations away from the well.

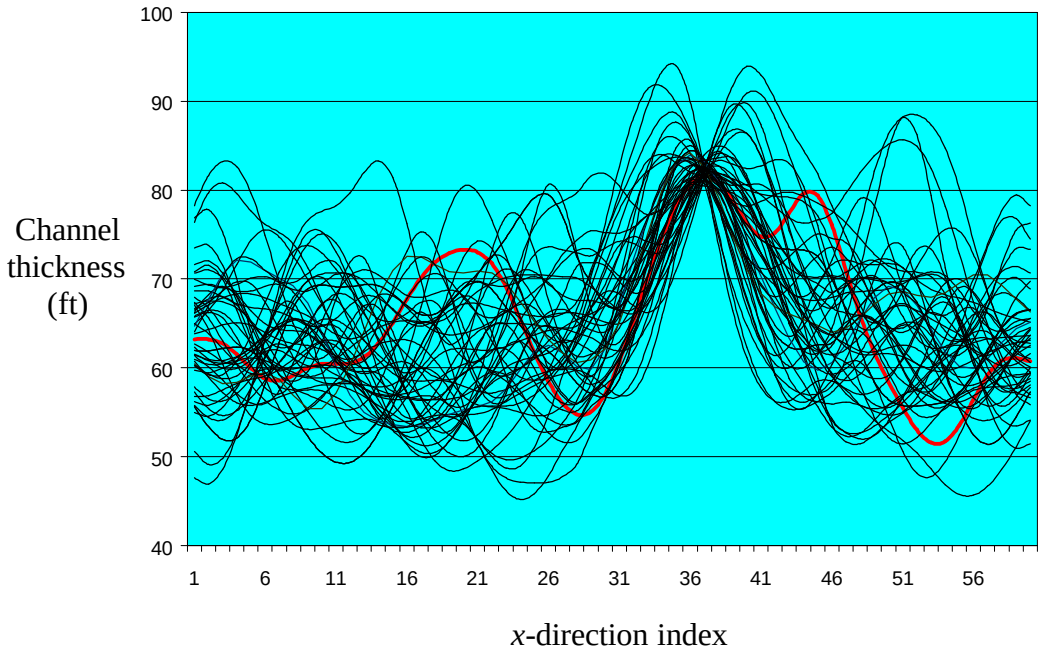

Fig. 5.36 – Conditional realizations of the channel thickness.

If the kh product of the channel is well resolved, then we expect that linear flow data should resolve reasonably the product of channel width and thickness. Fig. 5.37 verifies this conjecture, where 50 unconditional and conditional realizations of the channel cross-sectional area are shown in Figs. 5.37(a) and 5.37(b), respectively, with each realization being calculated by the product of the corresponding unconditional and conditional realizations of channel width and thickness.

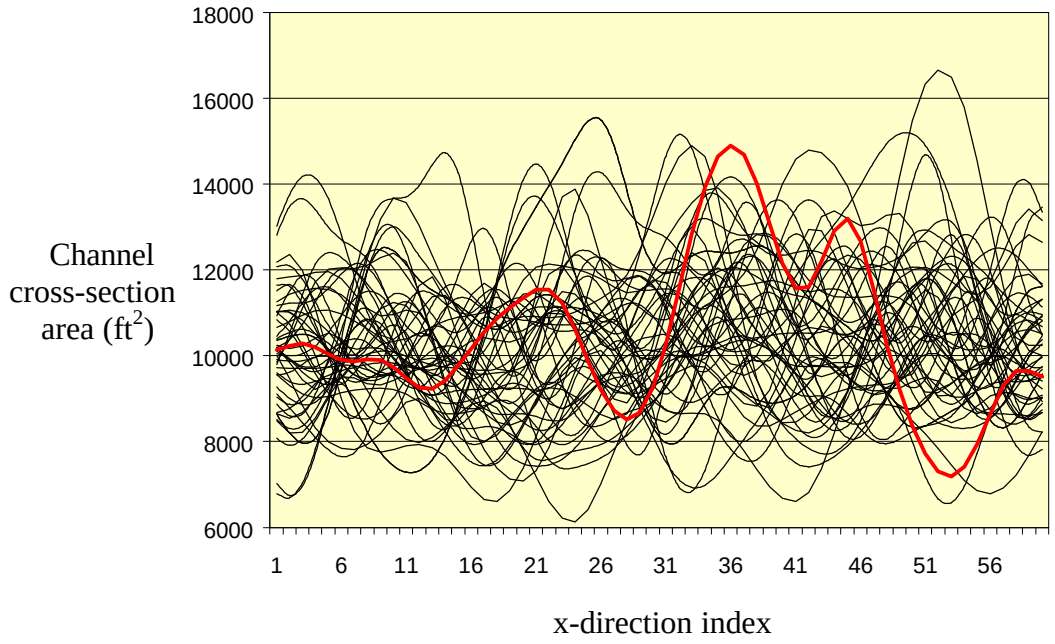

Fig. 5.37 (a) – Unconditional realizations of channel cross-sectional area.

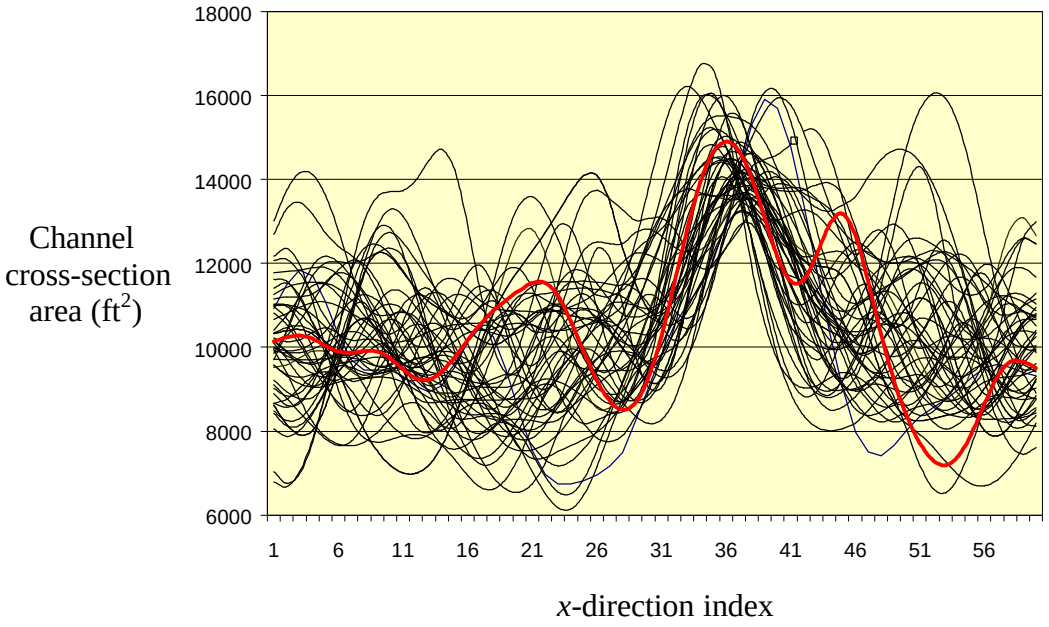

Fig. 5.37 (b) – Conditional realizations of channel cross-section area.

Another way to evaluate uncertainty is to plot histograms from the realizations of the parameter. As a check of how well the conditioning data are honored, Fig. 5.38 shows two histograms of the top depth of the channel at the well location. Fig. 5.38 (a) is based on 50 unconditional realizations of the top depth, whereas Fig. 5.38 (b) is based on 50 conditional realizations of the channel top depth. Since channel top depth at the well is conditioning data, it is honored by all of the conditional realizations. Therefore, the mean of the conditional samples is essentially equal to the observed top depth (126.5 ft) and the variance is very small (standard deviation is 0.95). However, the sample mean and variance of the unconditional realizations depend on the means and variances of the geometric model parameters related to the top depth of the channel, see Eq. 4.17. In addition to the mean value and standard deviation, other statistical parameters of the samples, e.g., maximum, minimum, lower and upper quartiles and median are also listed on the upper-right corner of each histogram.

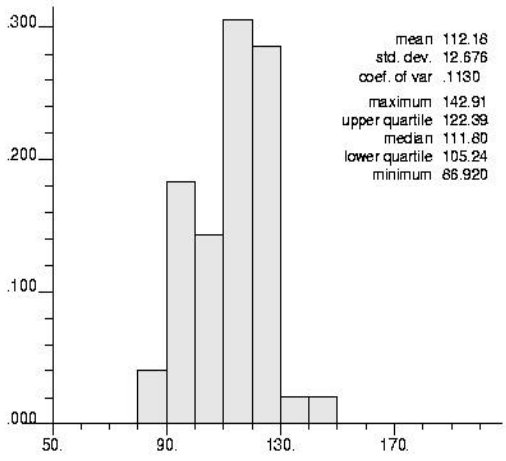

(a) Top depth at the well, based on unconditional realizations.

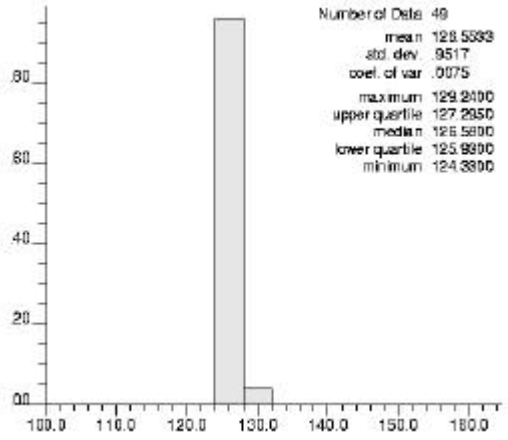

(b) Top depth at the well, based on conditional realizations.

Fig. 5.38 – Histograms of channel top depth based on (a) unconditional realizations and (b) conditional realizations. The vertical axis is the relative frequency of the samples.

Figs. 5.39 (a) and (b) presents the histograms of channel permeability based on 50 unconditional and conditional realizations, respectively. Since channel thickness at the well is observed data, and $\bar{k}h \cong k_c h_c$ is well resolved by radial flow data, we expect that channel permeability should be well resolved. If so, realizations obtained from the inversion process should exhibit only a very small variation in channel permeability. As shown in Fig. 5.39 (b), the mean of the conditional samples is 133.8 md, which is very close to the true channel permeability (134.1 md), whereas the standard deviation of the conditional samples is only 2.6. Note that the mean calculated from the set of unconditional realizations is 106.5 md, which is bigger than the prior mean of channel permeability (100 md) and the calculated standard deviation of 24.5 md is slightly smaller than the prior standard deviation (25 md). This simply reflects that the number of realizations (50) is not large enough to capture the exact statistical characteristics of the distribution. Similar results occur in all the histograms generated from the 50 unconditional realizations.

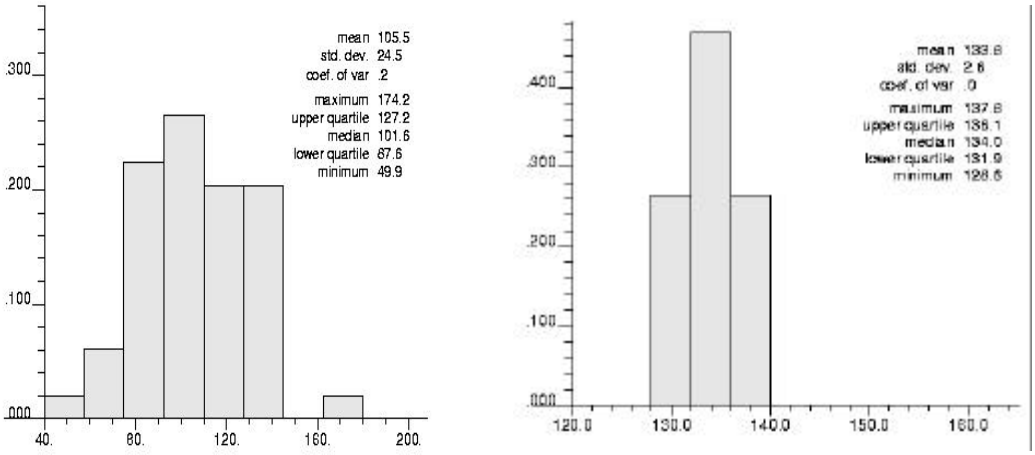

(a) Channel permeability based on unconditional realizations.

(b) Channel permeability based on conditional realizations.

Fig. 5.39 – Histograms of channel permeability based on (a) unconditional realizations and (b) conditional realizations.

The histograms for channel porosity, non-channel permeability and porosity are shown in Figs. 5.40 through 5.42. Again, there are two histograms in each figure, one is based on the set of unconditional realizations of the prior model and the other is based on conditional realizations obtained by the randomized maximum likelihood method. Note for these parameters, there is not a great difference between the statistics of the unconditional and conditional realizations, meaning that there is no significant reduction in the uncertainty of these parameters obtained by conditioning to the data. For example, the mean and standard deviation of the non-channel porosity based on unconditional realizations are 0.094 and 0.0234, the mean and variance of the corresponding conditional samples are 0.0895 and 0.0218, respectively, as shown in Figs. 5.42(a) and (b). The true non-channel porosity is 0.1.

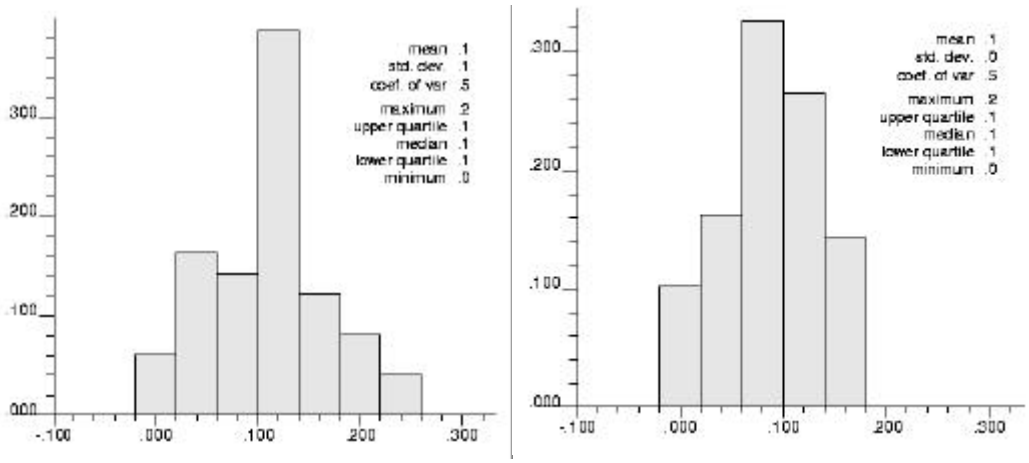

(a) Non-channel permeability based on unconditional realizations.

(b) Non-channel permeability based on conditional realizations.

Fig. 5.40 – Histograms of non-channel permeability based on (a) unconditional realizations and (b) conditional realizations.

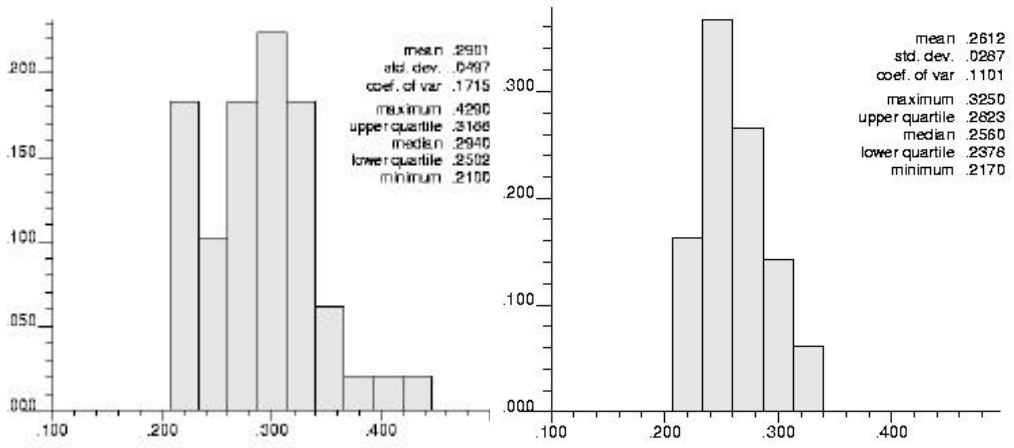

(a) Channel porosity based on unconditional realizations.

(b) Channel porosity based on conditional realizations.

Fig. 5.41 – Histograms of channel porosity based on (a) unconditional realizations and (b) conditional realizations.

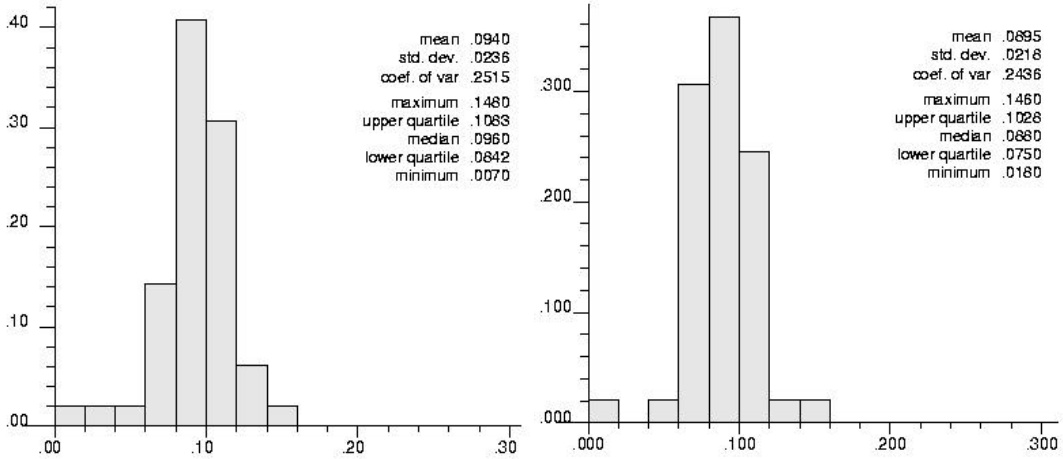

(a) Non-channel porosity based on unconditional realizations.

(b) Non-channel porosity based on conditional realizations.

Fig. 5.42 – Histograms of non-channel porosity based on (a) unconditional realizations and (b) conditional realizations.

For other geometric model parameters such as width of the channel, it is convenient to select a particular location for plotting histograms. As a comparison, we chose two locations; one is the well location and another is away from the well with the *x*-direction

index equal to 10. We plotted the histograms of channel width at these two locations, based on 50 unconditional and 50 conditional realizations. As we can see from Figs. 5.43 (a) and (b), the variation of channel width based on the conditional realizations is only slightly reduced, which indicates that the channel width at the well location was not very well resolved (the mean of the conditional samples is 171.2 ft and the true value is 180 ft). Far from the well, the uncertainty in channel width is not reduced (see Figs. 5.44 (a) and (b)).

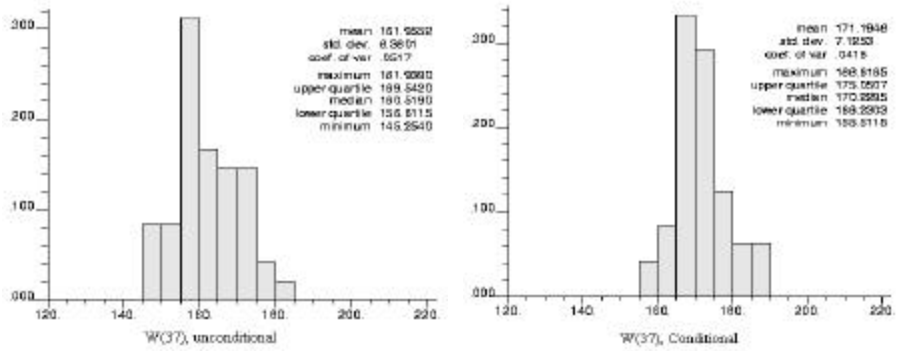

(a) (b)

Fig. 5.43 – Histograms of channel width at the well location based on (a) unconditional realizations and (b) conditional realizations.

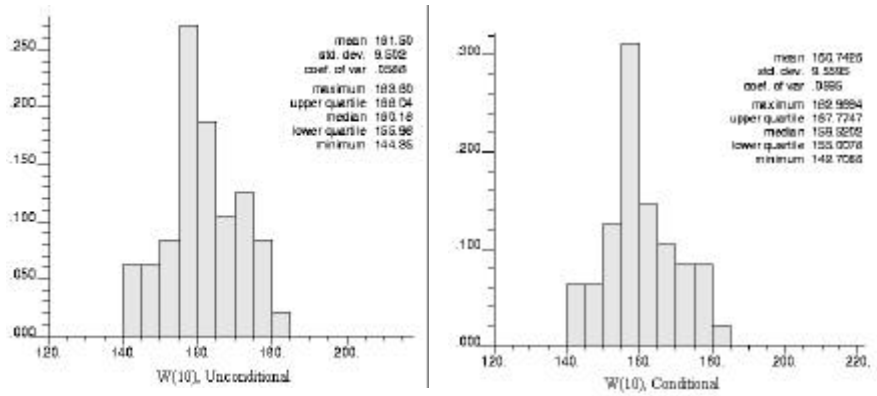

(a) (b)

Fig. 5.44 – Histograms of channel width at *x*-direction index i =10 based on (a) unconditional realizations and (b) conditional realizations.

5.5 Case 5: Unknown Channel Thickness

In the proceeding examples, both pressure data and observed channel thickness at the well were used as conditioning data. In this case, channel thickness was well resolved by the data. However, we expect that if channel thickness is unknown, radial flow pressure data will resolve only the kh product. In this example, we wish to see what reservoir properties can be resolved from only the observed pressure data and top depth of the channel; i.e., we deal with the cases where the observed channel thickness is not available. We will divide the observed pressure data into two sets; one contains only radial flow pressure data and the other contains only linear flow pressure data. We have already discussed the analytical expression of pressure derivative from radial flow. Here, we only wish to see what we can resolve from radial flow pressure data. Similarly, we wish to see what properties can be resolved from only linear flow pressure data. Theoretically, during linear flow in a homogeneous channel with straight boundaries and uniform width *W* and thickness *H*, the derivative of pressure with respect to the natural logarithm of time is inversely proportional to the product of the cross-sectional area of the channel (*HW*) and the square root of channel porosity (j_c) times channel permeability (k_c), i.e.,

$$\frac{\partial \Delta P}{\partial \ln t} \propto \frac{\sqrt{t}}{HW\sqrt{k_c j_c}}. \tag{5.25}$$

Therefore, it is reasonable to expect that linear flow pressure data should well resolve $HW\sqrt{k_c j_c}$ of the actual channel. However, if data from only a single well are available and *HW* varies with positions, then it is clear that a value of channel *HW* *x* feet to the

"right" of the well will have the same effect on pressure data as the same value *x* feet to the "left" of the well.

To illustrate these concepts, we consider only two cases. For each we will generate only one realization by the randomized maximum likelihood method using the Levenberg-Marquardt algorithm to minimize the appropriate objective function. All model parameters as well as the true model for these two cases are exactly the same as those in Case 4, see Tables 5.7 and 5.8 and Fig. 5.28.

Tables 5.10(a) and 5.10(b) list the simulated pressure data from radial flow and linear flow, respectively. Random noise will be added twice on these data sets, once to obtain the observed pressure data and a second time to obtain the unconditional realization of the data. These are also listed in Tables 5.10 (a) and (b).

Table 5.10 (a) – The radial flow pressure data.

Time (days)	Simulated pressure (psi)	Observed pressure (psi)	Unconditional realization (psi)
0.0001	3421.548	3421.364	3421.89
0.00022	3407.491	3407.327	3408.008
0.00036	3396.296	3396.216	3396.977
0.00054	3387.360	3386.296	3387.089
0.00074	3380.114	3380.225	3380.893
0.00099	3374.079	3374.502	3374.240
0.00129	3368.884	3369.748	3371.098
0.00165	3364.259	3363.580	3361.439
0.00208	3360.021	3361.346	3360.868
0.00260	3356.044	3356.388	3356.799
0.00322	3352.248	3352.295	3351.524
0.00396	3348.575	3348.960	3347.683
0.00485	3344.986	3344.693	3343.092
0.00592	3341.451	3341.651	3342.590

Table 5.10(b) – The linear flow pressure data.

Time (days)	Simulated pressure (psi)	Observed pressure (psi)	Unconditional realization (psi)
0.01	3340.859	3340.675	3341.842
0.0220	3319.218	3319.054	3318.287
0.0364	3304.791	3304.711	3306.287
0.0536	3291.655	3290.591	3290.510
0.0744	3278.472	3278.583	3278.456
0.0993	3264.718	3265.141	3264.172
0.1291	3250.07	3250.934	3251.772
0.1649	3234.237	3233.558	3232.049
0.2079	3216.902	3218.227	3217.879
0.2579	3198.266	3198.61	3198.157
0.3079	3180.717	3180.764	3180.378
0.3579	3163.982	3164.366	3163.138
0.4079	3147.883	3147.59	3148.425
0.4579	3132.299	3132.5	3133.205

Fig. 5.45 shows the objective function (the line with diamonds) and the kh product (with squares) at the well location for 5 iterations of the Levenberg-Marquardt algorithm. The horizontal line (purple) represents the true kh product at the well location. As we can see, the Levenberg-Marquardt algorithm converged in 5 iterations, with the objective function decreasing from 105 initially to about 17 at the 5^{th} iteration. The kh product at convergence is 10,851 md·ft, which is reasonably close to the true value of 10,936 md·ft. Based on the unconditional realization of the channel and its permeability, k_c= 96.38 md and the channel thickness at the well is 53.25ft, so the kh product at the well location is 5132 md·ft, which is far far away from the true value. Results from the conditional realization indicate that the channel thickness at the well location and channel permeability, respectively, are 74 ft and 146.2 md, compared to the true value of 80 ft and

134 md. This represents the expected results; i.e., radial flow pressure data do not accurately resolve k and h, individually. Fig. 5.46 shows the calculated and the observed pressure data, which are in good agreement where the calculated data were obtained from the conditional realization.

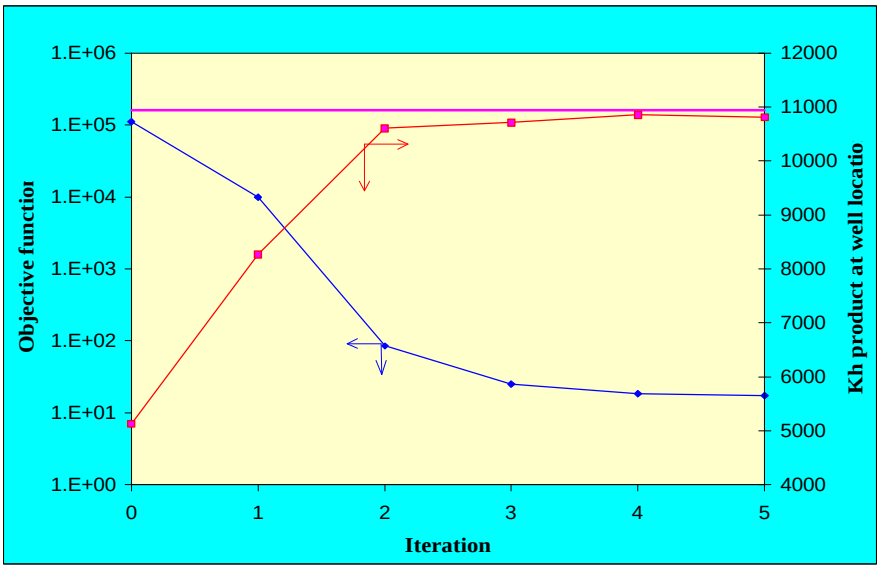

Fig. 5.45 – The objective function and kh product versus iteration.

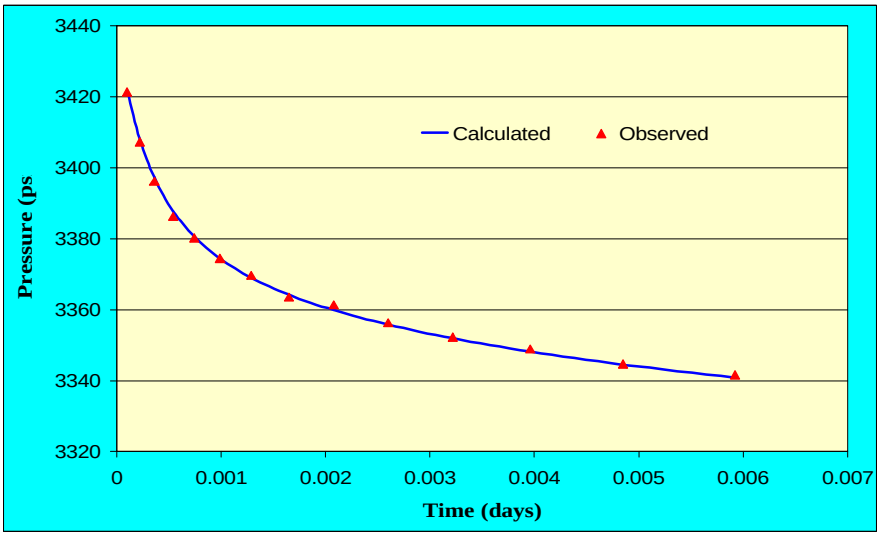

Fig. 5.46 – The radial flow pressure data matching.

Recall that the channel thickness and width vary with x. Figs. 5.47 and 5.48 show how the channel thickness and the kh product vary along the channel. In Figs. 5.47 and 5.48, the black lines with triangles represent the true fields, whereas the dark gray ones with diamonds are from the conditional realizations and the gray ones with squares are from the unconditional realizations. The well is located at the 37^{th} gridblock in the x-direction, i.e., $x_i = x_{37}$. As in the previous examples, the channel thickness from the conditional realization are much closer to the true values around the well location, but similar to the values from the unconditional realization away from the well location. However, the kh product values around the well location are very well resolved compared to the channel thickness itself, see Fig. 5.48. Away from the well, there is approximately a constant difference between the conditional realization and the unconditional realization, which depends on the corresponding permeability difference.

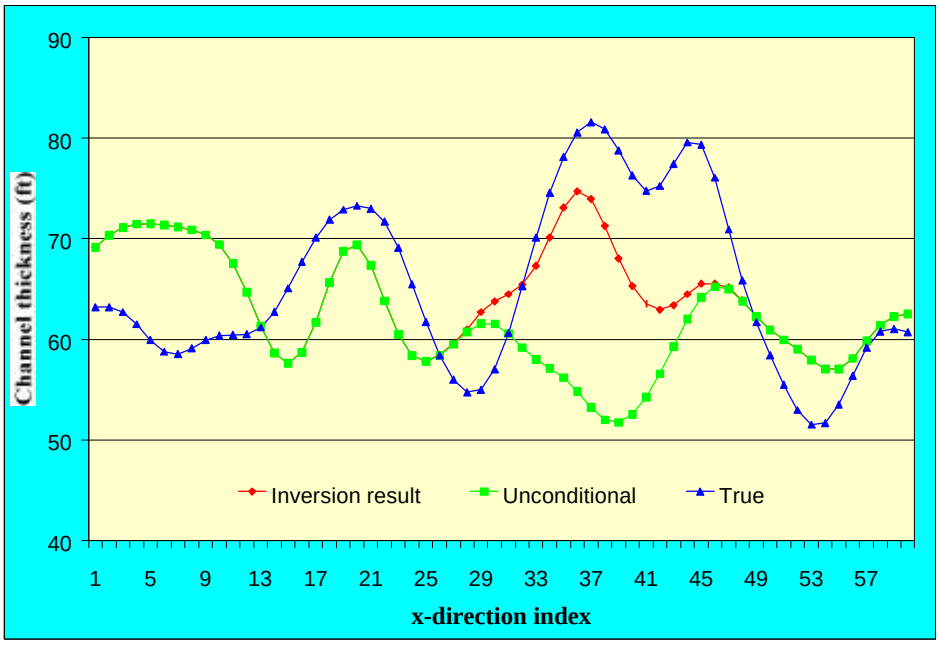

Fig. 5.47 – Channel thickness versus x-direction index.

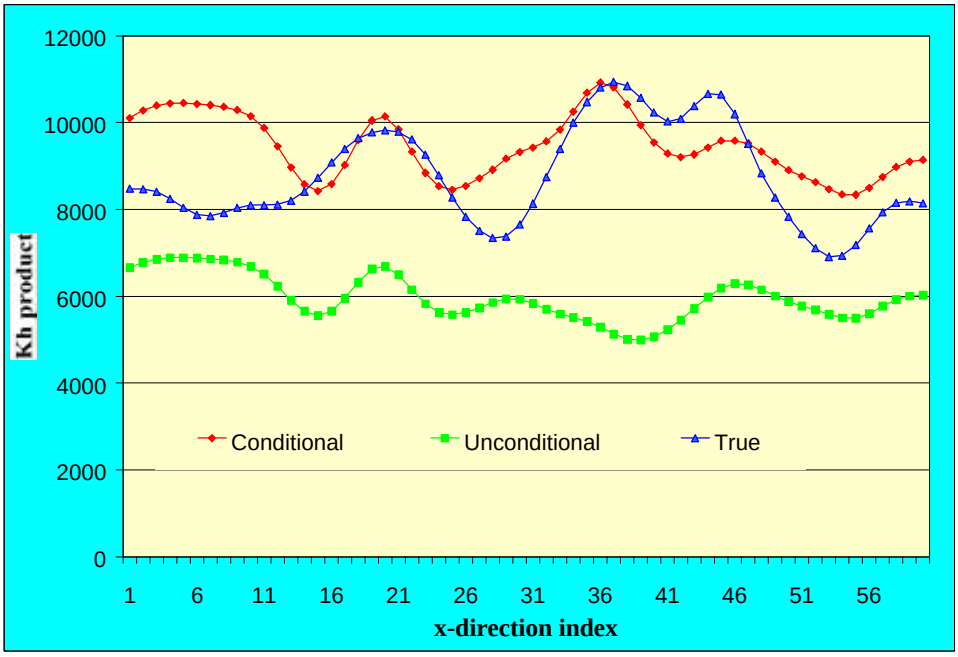

Fig. 5.48 – The kh product versus *x*-direction index.

We also generated a conditional realization of the channel and rock properties by conditioning only to the linear flow pressure data (Table 5.10(b)) and the observed top depth of the channel at the well location. In this case, the Levenberg-Marquardt algorithm also converged in 5 iterations. The objective function at convergence was 23. Fig. 5.49 shows the agreement between observed and calculated pressure data, where the solid line represents the calculated pressure data at the last iteration of the Levenberg-Marquardt algorithm and the red triangles are the synthetic observed pressure data. The average sum of the squared pressure mismatch was 1.6 in this case, see Eq. 3.37. The observed top depth of the channel was honored. The observed top depth is 127.1 ft and at the last iteration of the Levenberg-Marquardt algorithm, the calculated top depth at the well location is 126.1 ft, which is very close to the true value (126.3 ft).

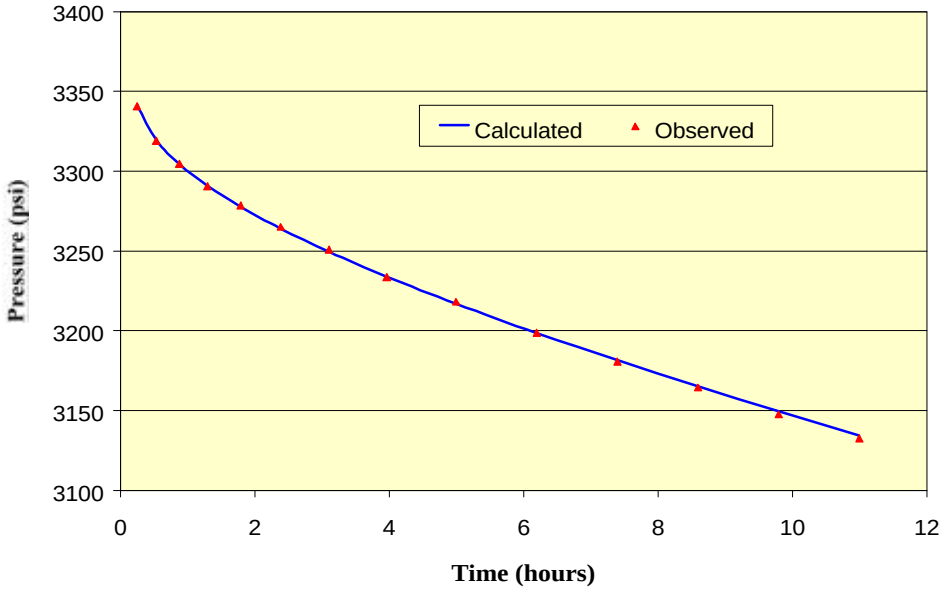

Fig. 5.49 – Pressure data matching for linear flow.

Physically, linear flow occurs after the radial flow, i.e., after the pressure data has been influenced by the channel boundaries in the *y*-direction. In the true model, the well is located 8 gridblocks away from both boundaries in the *y*-direction. Therefore, the region that affects the linear flow pressure data is roughly 8 or 9 gridblocks away from the well in the *x*-direction. Figs. 5.50 through 5.53 show the channel width (*W*), thickness (*H*), cross-sectional area (*WH*) and $WH\sqrt{k_c j_c}$ from the conditional realization, the unconditional realization and from the true model, respectively. Again the black lines with triangles represent the true fields, the dark gray ones with diamonds are based on the conditional realization from the randomized maximum likelihood method and the gray ones are based on the unconditional realizations. A common feature in these figures is that the above properties based on the conditional realization are closer to those from the true model in a broader area in the *x*-direction and none of them was very well resolved near the well which is located at the 37th gridblock. For example, the channel

widths at the *x*-direction index equal to 27 (10 blocks away to the left of the well location) are 155.7 ft (true), 164.6 ft (conditional) and 169.7 ft (unconditional), respectively, see Fig. 5.50. The channel cross-sectional areas at the same location in Fig. 5.51 are 8718.2 ft^2 (true), 12059.5ft^2 (conditional) and 13751.4 ft^2 (unconditional), and the values of the quantity, $WH\sqrt{k_c j_c}$, are 51572.9 (true), 68281.1 (conditional) and 73231.6 (unconditional), see Fig. 5.52.

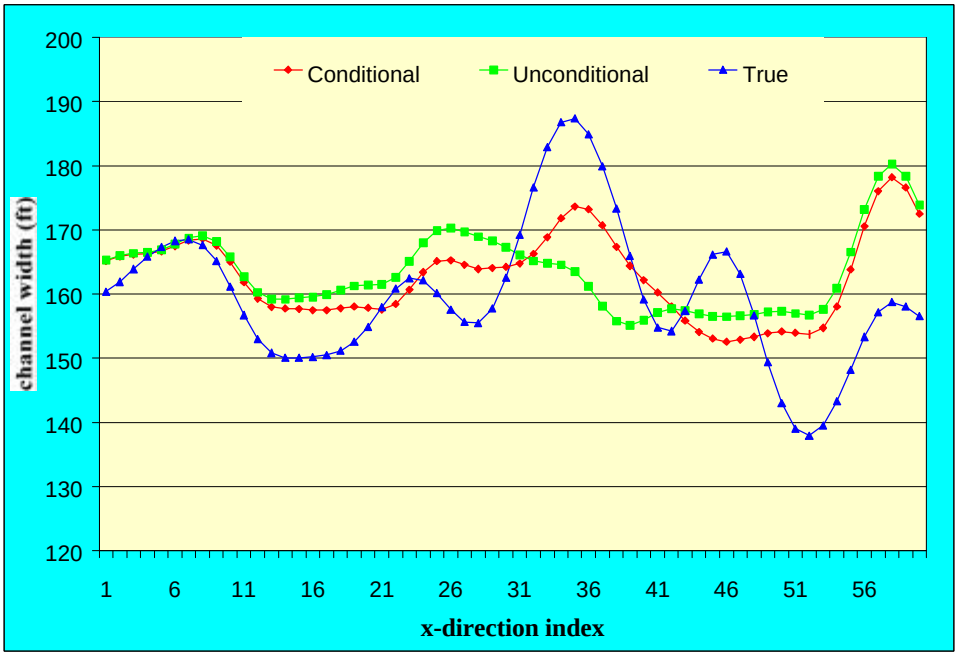

Fig. 5.50 – Channel width versus the *x*-direction index for linear flow case.

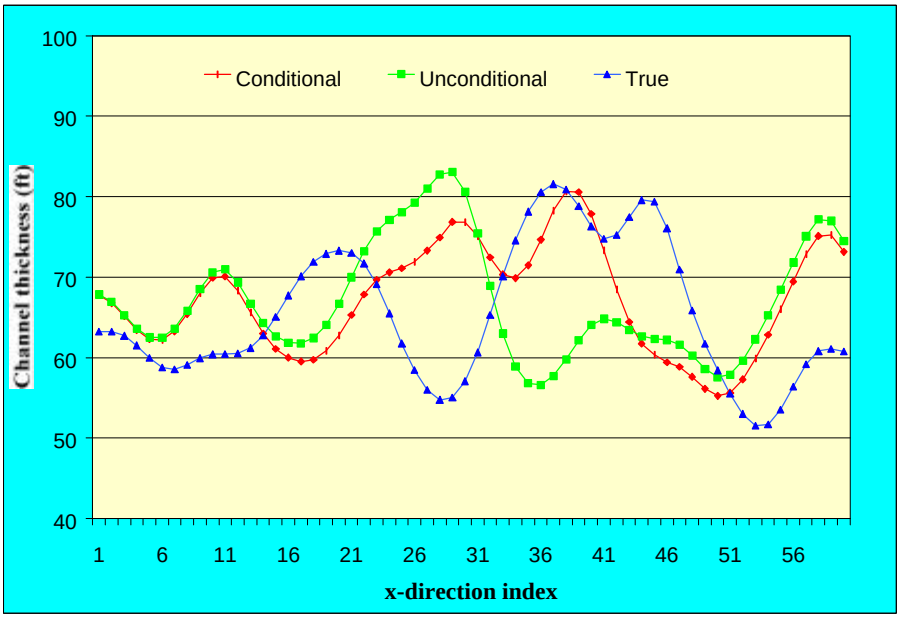

Fig. 5.51 – Channel thickness versus the *x*-direction index.

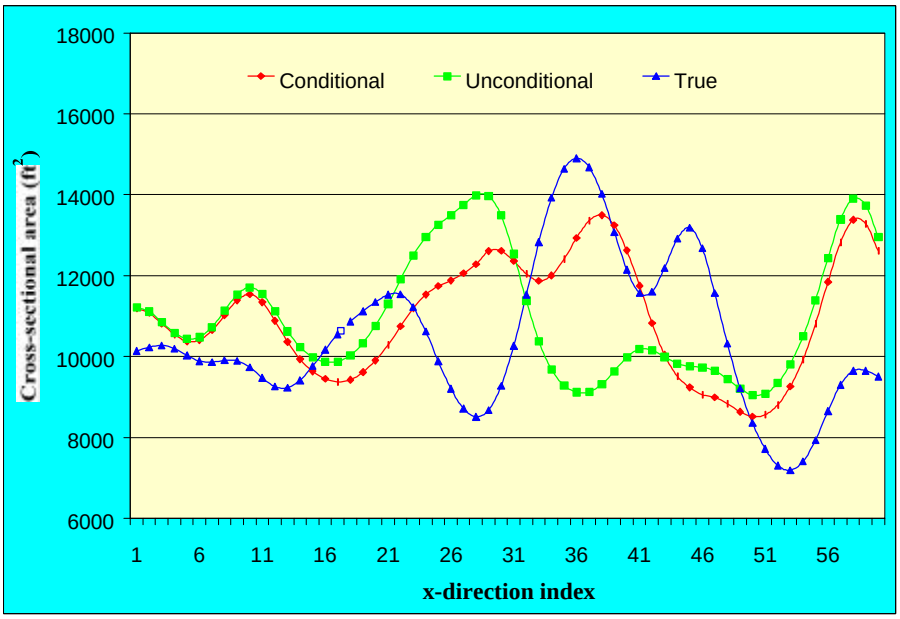

Fig. 5.52 – Channel cross-sectional area versus the *x*-direction index.

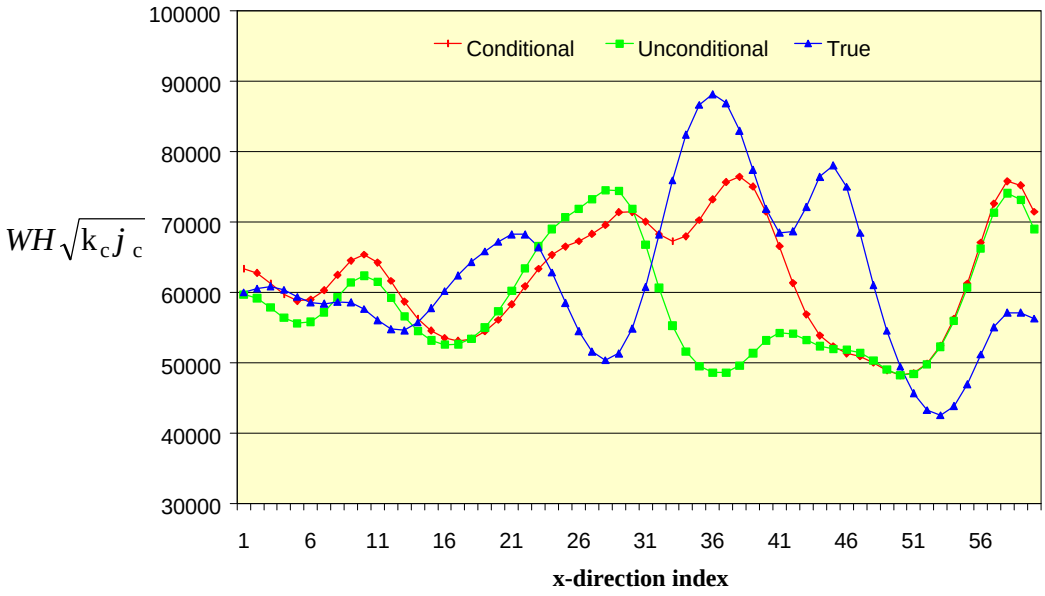

Fig. 5.53 – The value of $WH\sqrt{k_c j_c}$ versus the x-direction index.

Since the influence of the WH value at x_i has on pressure data depends primarily on the distance between x_i and x_w (the x-coordinate of the well location), a more representative quantity for investigating whether $WH\sqrt{k_c j_c}$ is resolved by linear flow data is

$$f(d) = \frac{1}{2}\left[H(x_w + d)W(x_w + d) + H(x_w - d)W(x_w - d)\right]\sqrt{k_c j_c}\,. \qquad (4.26)$$

Here x_w is the x-coordinate of the well, $d = x_i - x_w$ represents the distance between x_i and the x-coordinate of the well location, so d=0 represents the well location itself. $H(x)$ is the channel thickness at x such that x represents the x-coordinate of the gridblock center and $W(x)$ represents the channel width at x. k_c and j_c are the channel permeability and porosity, respectively, and permeability and porosity in the channel are homogeneous. Note, f(d) represents the average of the quantity $WH\sqrt{k_c j_c}$ at two locations symmetric

to the well location. If $WH\sqrt{k_c j_c}$ is well resolved from linear flow pressure data, then a plot of f(d) for conditional and unconditional realizations should show that the conditional realizations are closer to the values of f(d) from the true model. If we generate multiple unconditional and conditional realizations, then we would expect that the variation in f(d) based on the conditional realization should be much smaller than the variation of f(d) based on the unconditional realizations. Fig. 5.54 and Fig. 5.55 show 10 unconditional and conditional realizations of f(d), respectively. In Figs. 5.54 and 5.55, the thick line represents the f(d) calculated from the true model and all other curves are obtained from 10 conditional and unconditional realizations, respectively. As seen from Fig. 5.55, from the 7th gridblock to 18th gridblock from the well, the values of f(d) are much closer to the true case and the variation of f(d) is much narrower than that shown in Fig. 5.54. This supports our conjecture that the average value of $WH\sqrt{k_c j_c}$ as a function of distance from the well is well resolved from the linear flow pressure data.

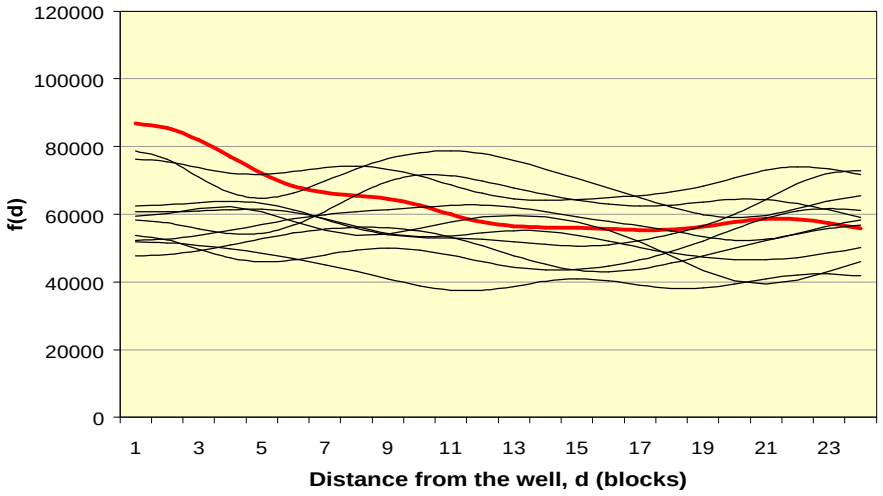

Fig. 5.54 – Function f(d) based on 10 unconditional realizations.

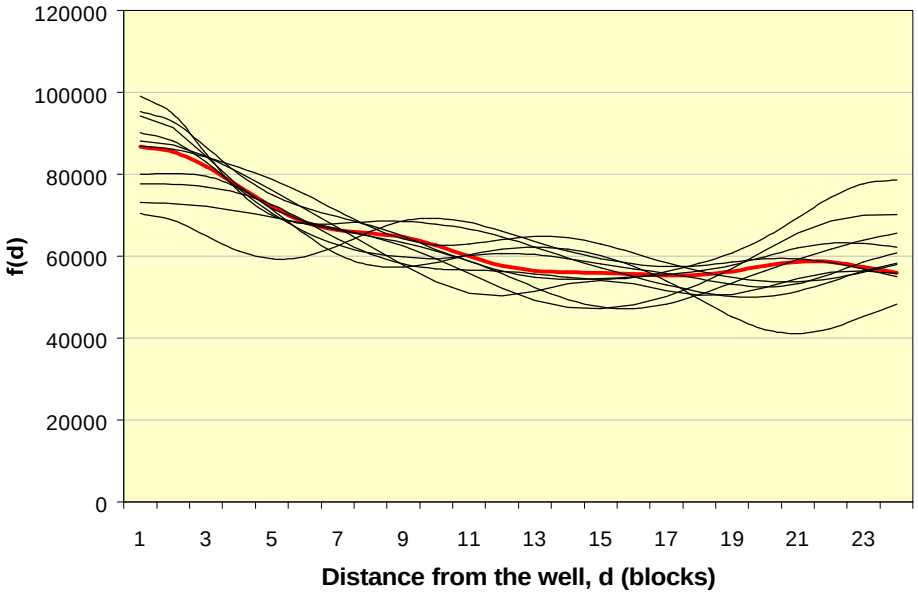

Fig. 5.55 – Function f(d) based on 10 conditional realizations.

CHAPTER VI

CONCLUSIONS

We have implemented the randomized maximum likelihood method to condition a stochastic model for a single 3D channel to well test pressure data, channel thickness and depth of the channel top observed at the well location. The generation of each realization by this method requires the minimization of an appropriate objective function. We have implemented a form of the Levenberg-Marquardt algorithm to perform this minimization. We have shown that the overall methodology relies mainly on the following factors: a well-defined stochastic model (the prior) of channel geometry; the construction of the a posteriori probability density function (pdf) and assumed objective function; an accurate and efficient approach for the computation of sensitivity coefficients of the conditioning data to the model parameters and finally an efficient way to sample the a posteriori pdf and generate realizations that honor the data and the prior knowledge. We have seen from the synthetic case studies that the methodology implemented was successful.

The prior stochastic channel model used was defined with four Gaussian random variables and four 1D Gaussian random fields for a single channel in three-dimensional domain. The four random variables define the principal direction line which controls the orientation or main directional tendency of the channel body. The horizontal sinuosity and vertical sinuosity, modeled as 1D Gaussian fields, determine the shape of the channel, whereas the width and aspect ratio specify the dimensions or sizes of the

channel in space. This model is flexible and representative of reality. More importantly, with this prior, it is simple to evaluate the sensitivity coefficients of model parameters to conditioning data provided the entire channel body could be completely contained within the reservoir grid.

The a posteriori pdf was formulated from the Bayes's theorem. In addition to multiple Gaussian priors, we assumed that data measurement errors can be modeled as independently, identically distributed multiple Gaussian with mean zero and known variances. Conditioning data included well-test pressure data, the observed channel thickness, and the measured depth of channel top at the well location.

We developed a very efficient analytical method to evaluate the sensitivities of gridblock permeability and porosity to the geometric model parameters of the channel. These results are needed to compute the sensitivities of the conditioning pressure data to the model parameters by an application of the chain rule. These sensitivities are used when sampling the a posteriori pdf by the randomized maximum likelihood method. Although uniform grid size, constant permeability and porosity inside and outside the channel were used in the derivations and illustrations, there appears to be no difficulties in applying the methodology for a non-uniform grid and completely heterogeneous permeability and porosity fields. The basic idea should also be extendable to multi-channel, multi-well and multiphase flow circumstances, although this will require additional theoretical development.

For sampling the a posteriori pdf, we implemented the randomized maximum likelihood method to generate realizations from the pdf. We know that this sampling procedure gives correct realizations if the observed data are linearly related to the model.

However, it represents only an approximate sampling in our case, where the relationship between the well test pressure data and the channel model parameters is non-linear.

In sampling with the randomized maximum likelihood method, we have applied a form of the Levenberg-Marquardt algorithm to minimize the objective function. The case studies presented have verified the effectiveness and efficiency of this algorithm. It only requires 4 to 6 iterations for convergence in the cases we considered, which takes about 20 to 45 minutes on a Pentium 400 computer. At each iteration, sensitivity coefficients are computed only once, but an iteration might require several flow simulation runs, depending on the behavior of the objective function. The algorithm uses a damping factor to avoid an explicit line search. The difficulty is in selecting a starting value of the factor. In all the cases of this study, we have used a value of 1000 to initialize the algorithm. We found that this starting value is appropriate in most cases.

Based on the results of synthetic case studies, we found that good estimates of reservoir properties, such as the kh product of the reservoir around the well, the total channel volume or total pore volume, and the flow cross-section area of the reservoir around the well could be obtained using pressure data from a single well, provided pressure data during appropriate flow periods are available. For example, the total pore volume of the reservoir could be well resolved if pseudo-steady state pressure data are available. Moreover, conditioning to pressure data, the observed channel thickness and top depth does reduce the uncertainty in the geometric parameters near the well location.

NOMENCLATURE

Symbol

a	correlation length of the Gaussian covariance function, ft.
AR	aspect ratio.
b	gridblock index.
c	normalizing constant of a probability density function.
c_t	total system compressibility, psi^{-1}.
C_{AR}	prior covariance matrix for aspect ratio.
C_D	data covariance matrix.
$C_{D,p}$	pressure data covariance matrix.
$C_{D,t}$	data covariance matrix for channel thickness.
$C_{D,z}$	covariance matrix for channel top depth.
C_G	prior covariance matrix for geometric parameters.
C_ℓ	prior covariance matrix for the principal direction line.
C_M	prior covariance matrix.
C_R	prior covariance matrix for rock properties.
C_{S_h}	prior covariance matrix for horizontal sinuosity.
C_{S_h}	prior covariance matrix for vertical sinuosity.

C_W	prior covariance matrix for channel width.
d	vector of predicted data.
d_{obs}	vector of observed data.
d_{obs}^{p}	vector of observed pressure data, psi.
d^{H}	vector of predicted channel thickness, ft.
d^{p}	vector of predicted pressure data, psi.
d^{z}	vector of predicted channel top depth, ft.
E	expectation of a random variable or random field.
$f(x)$	square root of a covariance function.
$f_{\mathrm{M}}(m)$	prior probability density function of the model.
$g(m)$	relationship between predicted data and model parameters.
G	sensitivity coefficient matrix.
h	distance of a gridblock center from the well location, ft.
$H(m)$	Hessian matrix.
$H(x)$	Channel thickness at x, ft.
H_{obs}	observed channel thickness, ft.
k	permeability, md.
$\bar{\mathrm{k}}$	average permeability, md.
K	permeability field, md.
ℓ_p	principal direction line.
ℓ_c	channel center.

m	vector of model parameters.
m_{G}	vector of channel geometric parameters.
$m_{G,prior}$	vector of prior means of geometric model parameters.
m_{prior}	vector of prior means of model parameters.
m_r	vector of rock properties.
$m_{r,prior}$	vector of prior means of rock properties.
N_b	number of simulation gridblocks.
N_d	number of conditioning data.
N_p	number of observed channel thickness.
N_T	number of observed pressure data.
N_x	number of gridblocks in the *x*-direction.
N_y	number of gridblocks in the *y*-direction.
N_z	number of gridblocks in the *z*-direction.
N_w	number of wells.
$O(m)$	objective function.
p	pressure, psi.
p_i	i^{th} observed pressure, psi.
$\mathrm{P_b}(x)$	proportion of channel interior in a bottom boundary gridblock.
$\mathrm{P_l}(x)$	proportion of channel interior in a left boundary gridblock.
$\mathrm{P_r}(x)$	proportion of channel interior in a right boundary gridblock.
$\mathrm{P_t}(x)$	proportion of channel interior in a top boundary gridblock.

q	flow rate, RB/D.
r_b	volume fraction of channel interior in a gridblock, fraction.
r_w	wellbore radius, ft.
S_h	horizontal sinuosity, ft.
S_v	vertical sinuosity, ft
s_{xy}	slope of the projection of the principal direction line in the *x*-*y* plane.
s_{xz}	slope of the projection of the principal direction line in the *x*-*z* plane.
t	time, days.
V	gridblock volume, ft^3.
V_i	volume of channel interior in a gridblock, ft^3.
V_o	volume of non-channel facies in a gridblock, ft^3.
W	channel width, ft.
y_0	*y*-coordinate of the principal direction line at starting point, ft.
z_0	*z*-coordinate of the principal direction line at starting point, ft.
a	constant in the Levenberg-Marquardt algorithm.
m	viscosity, cp.
m_{AR}	mean of aspect ratio.
m_W	mean of channel thickness, ft.
j	porosity, fraction.
Φ	porosity field.
s^2	variance of a random variable.

Subscripts

b	related to a gridblock.
c	related to channel facies or channel center.
G	related to channel geometric parameters.
nc	related to non-channel facies.
r	related to rock property field.
w	related to well.
W	related to channel width.

Superscripts

T	transpose.
-1	matrix inverse.

REFERENCES

1. Anterion, F., Karcher, B. and Eymard R. (1989): " Use of Parameter Gradients for Reservoir History Matching," SPE 18433, Proceedings of the 10th SPE Reservoir Simulation Symposium, p 339-354.
2. Carter, R. D., Kemp, L. F., Pierce, A. C. and Williams, D. L. (1974): "Performance Matching With Constraints," SPE Journal, April 1974, p 187-196.
3. Carter, R. D., Kemp, L. F., Pierce, A. C. (1974): "Discussion of Comparison of Sensitivity Coefficient Calculation Methods in Automatic History Matching," SPEJ, 22, p 205-208.
4. Carvalho, R. S., Redner, A. R., Thompson, L. G. and Reynolds, A. C. (1992): "Robust Procedures for Parameter Estimation by Automated Type-Curve Matching," SPE 24732, presented at the 1992 SPE Annual Conference and Exhibition, Washington D. C., Oct. 4-7.
5. Chavent, G. M., Dupuy, M. and Lemonnier, P. (1975): "History Matching by Use of Optimal Control Theory," SPEJ, 15(1), p 74-86.
6. Chen, W. H., Gavalas, G. R. and Seinfeld, J. H. (1974): "A New Algorithm for Automatic History matching," SPEJ, p 953-608, December.
7. Chu, L., Reynolds, A. C. and Oliver, D. S. (1995): "Reservoir Description From Static and Well-Test Pressure Data Using Efficient Gradient Methods," SPE 29999,

presented at the 1995 SPE International Meeting on Petroleum Engineering, Beijing, China, Nov. 14-17.

8. Cunha, L. B., Oliver, D. S., Redner, R. A. and Reynolds, A. C. (1996): "A Hybrid Markov Chain Monte Carlo method for Generating Permeability Fields Conditioned to Multiwell Pressure Data and Prior Information," SPE 36566, presented at the 1996 SPE Annual Technical Conference and Exhibition, Denver, Oct. 1-9.
9. Georgsen, F. and Omre, H. (1992): "Combining Fiber Processes and Gaussian Random Functions for Modeling Fluvial Reservoirs," In Geostatistics troia'92, p 425-439.
10. Georgsen, F., Egeland, T., Knarud, R. and Omre, H. (1994): "Conditional Simulation of Facies Architecture in Fluvial Reservoirs," In Geostatistical Simulations, p 235-250, Kluwer academic, Dordrecht, 1994.
11. He, Nanqun (1997): "Three Dimensional Reservoir Description by Inverse Problem Theory Using Well-Test Pressure and Geostatistical Data," PhD Dissertation, University of Tulsa, 1997.
12. He, N., Reynolds, A. C. and Oliver, D. S. (1996): "Three-dimensional Reservoir Description from Multi-well Pressure Data and Prior Information," SPE 36509, presented at the 1996 SPE Annual Technical Conference and Exhibition, Denver, Colorado, Oct. 6-9.
13. Journel, A. G. (1974): "Geostatistics for Conditional Simulation of Ore Bodies," Economic Geology, Vol. 69, p 673-687.
14. Journel, A. G. and Huijbregts, C. J. (1978): "Mining Geostatistics," Academic Press, New York, 600p.

15. Kitanidis, P. K. (1986): “Parameter Uncertainty in Estimation of Spatial Function: Bayesian Analysis,” Water Resources Research, 22(4), p 499-507.
16. Landa, J. L. (1997): “Reservoir Parameter Estimation Constrained to Pressure Transients, Performance History and Distributed Saturation Data,” PhD Dissertation, Stanford University.
17. Landa, J. L. and Horne, R. N. (1997): “A Procedure to Integrate Well Test Data, Reservoir Performance History and 4D Seismic Information into a Reservoir Description,” SPE 38653, in 1997 SPE Annual Technical Conference and Exhibition.
18. Oliver, D. S. (1994): “Incorporation of Transient Pressure Data into Reservoir Characterization,” In Situ, Vol. 18, No. 3, p 243-275.
19. Oliver, D. S. (1995): “Moving Averages for Gaussian Simulation in Two and Three Dimensions,” Mathematical Geology, 27(8), p 939-960.
20. Oliver, D. S. (1998): “Conditioning Multiple 2D Channels to Well Test Data,” TUPREP Report, 1998.
21. Oliver, D. S., He, N., Reynolds, A. C. (1996): “Conditioning Permeability Fields to Pressure Data,” ECMOR, Leoben, Austria, 3-6, Sept.
22. Rahon, D., Edoa, P. F. and Masmoudi, M. (1997): “Inversion of Geological Shapes in Reservoir Engineering Using Well-tests and History matching of Production Data,” SPE 38656, Presented in SPE Annual Technical Conference and Exhibition.
23. Reynolds, A. C., He, N., and Oliver, D. S. (1997): “Reducing Uncertainty in Geostatistical Description with Well Testing Pressure Data,” Fourth International Reservoir Characterization Technical Conference, Houston, Texas, 2-4, March.

24. Tarantola, A. (1987): “Inverse Problem Theory, Models for Data Fitting and Model Parameter Estimation,” Elsevier Science Publishers, Amsterdam

25. Wu, Z. (1999): “Conditioning Geostatistical Models to Two-phase Production Data,” PhD Dissertation, The University of Tulsa.

26. Wu, Z., Reynolds, A. C. and Oliver, D. S. (1998): “Conditioning Geostatistical Models to Two-phase Production Data,” SPE 49003.

27. Yeh, W. (1986): “Review of Parameter Identification Procedures in Groundwater Hydrology,” Water Resources Research, 22, p 95-108.